UNIVERSITY OF SOUTHERN DENMARK

PHD THESIS

Active nanophotonic circuitry based on surface plasmons

Author:
Martin THOMASCHEWSKI

Supervisor:
Prof. Dr. Sergey I.
BOZHEVOLNYI

*A thesis submitted in partial fulfillment of the requirements
for the degree of Doctor of Philosophy*

at the

Centre for Nano Optics
Mads Clausen Institute

June 2, 2020

ii

Active nanophotonic circuitry based on surface plasmons

UNIVERSITY OF SOUTHERN DENMARK

Abstract

Center for Nano Optics
Mads Clausen Institute

Doctor of Philosophy

Active nanophotonic circuitry based on surface plasmons

by Martin THOMASCHEWSKI

This PhD thesis presents investigations of active plasmonic circuitry with high efficiencies designed for compact and ultra-fast conversion of signals between the electrical and optical domain. Owing to a strong enhancement of electromagnetic fields in metal nanostructures and a high field-overlap between the optical and electrostatic fields, the presented plasmonic devices can serve as an alternative to traditional optical telecommunication devices by offering faster device operation at much more compact footprints. The experimental and theoretical studies consider nanophotonic waveguides and couplers based on surface plasmon polaritons, which are collective electron oscillations propagating along a metal-dielectric interface. The nanophotonic circuits are designed and optimized by analytical and numerical methods, and subsequently fabricated by electron-beam lithography and thin-film deposition techniques. The first part of the thesis outlines the development of highly-dense integrated plasmonic circuits, which allow the realization of branchless interferometric systems consisting of two parallel plasmonic waveguides which are excited via ultra-compact antenna couplers. The thesis continues with the development of active plasmonic structures, incorporating optoelectronic phenomena for spin-selective photodetection and electro-optic modulation. The device operation is characterized by their optical and optoelectronic response using optical spectroscopy techniques, revealing a record-high electro-optic efficiency of the proposed plasmonic modulator as compared with competitive devices based on the same material platform. Further studies on utilizing long-range plasmonic waveguides suggests the development of low-loss plasmonic electro-optic modulators. The thesis ultimately arrives at the conclusion that active plasmonic technology can meet the future needs of active integrated circuits and optical communications systems.

iv

Resumé

Denne ph.d.-afhandling præsenterer undersøgelser af aktive plasmoniske kredsløb med høj effektivitet designet til kompakt og ultrahurtig konvertering af signaler mellem det elektriske og optiske domæne. På grund af en stærk forstærkning af elektromagnetiske felter i metalnanostrukturer og en høj feltoverlapning mellem det optiske og elektrostatiske felt, kan de præsenterede plasmoniske enheder tjene som et alternativ til traditionelle optiske telekommunikationsindretninger ved at tilbyde hurtigere enhedsdrift ved meget mere kompakte fodaftryk. De eksperimentelle og teoretiske undersøgelser betragter nanofotoniske bølgeledere og koblere baseret på overfladeplasmon-polaritoner, som er kollektive elektronoscillationer, der forplantes langs en metal-dielektrisk grænseflade. De nanofotoniske kredsløb er designet og optimeret ved hjælp af analytiske og numeriske metoder og fremstilles derefter ved elektronstråle litografi og tyndfilmaflejringsteknikker. Den første del af afhandlingen skitserer udviklingen af meget tætte integrerede plasmoniske kredsløb, som tillader realisering af grenløse interferometriske systemer, der består af to parallelle plasmoniske bølgeledere, som tilgås via ultrakompakte antennekoblere. Specialet fortsætter med udviklingen af aktive plasmoniske strukturer, der inkorporerer optoelektroniske fænomener til spin-selektiv fotodetektion og elektrooptisk modulation. Komponentens drift undersøges gennem sin optiske og optoelektroniske respons ved anvendelse af optiske spektroskopiteknikker, hvilket afslører en rekordhøj elektrooptisk effektivitet af den foreslåede plasmoniske modulator sammenlignet med konkurrencedygtige anordninger baseret på den samme materialeplatform. Yderligere undersøgelser omkring anvendelse af langtrækkende plasmoniske bølgeledere viser muligheden for udvikling af plasmoniske elektrooptiske modulatorer med lavt tab. Afhandlingen kommer til sidst til den konklusion, at aktiv plasmonisk teknologi kan imødekomme fremtidige behov for aktive integrerede kredsløb og optiske kommunikationssystemer.

Preface & Acknowledgements

This thesis is based upon studies conducted during my PhD at the Centre for Nano Optics, University of Southern Denmark, from December 2016 to Mai 2020, under the supervision of Dr. Scient. Sergey I. Bozhevolnyi. The project included a one-month stay at the University of Burgundy, Dijon, France, where I collaborated with researchers from the group of Jean-Claude Weeber. Three peer-reviewed publications constitute the PhD thesis, appearing in appendices A-C, as they pertain to the subject of this thesis, namely developing active nanophotonic waveguides and devices based on surface plasmon polaritons. A complete list of my publications can be found in the section "Publications and presentations".

My time as a PhD student at the Centre for Nano Optics, University of Southern Denmark has been an unforgettable experience where I could learn, grow and thrive both professionally and personally thanks to the following amazing individuals.

First and foremost, I would like to express my respectful gratitude to Prof. Dr. Sergey I. Bozhevolnyi for his skilful, patient and caring guidance. The steadfast trust and outstanding support I received during the time as a doctoral student were the basis on which this dissertation grew. I certainly couldn't have imagined having a better supervisor for my PhD.

I would also like to sincerely thank Professor Jean-Claude Weeber and Alain Dereux for welcoming me as a visiting PhD student to their research group. Though unfortunately interrupted due to the COVID-19 pandemic, I truly enjoyed the time during my research stay and sincerely hope that our research activity of realizing LR-DLSPP waveguide modulators will continue.

Further, I am deeply thankful to all current and former members of the Centre for Nano Optics. Special thanks goes to Yuanqing Yang, Alexander S. Roberts, Vladimir Zenin and Christian Wolff for the support I received throughout our collaborative work. Furthermore, I highly appreciate the support of Jeanette Holst for helping the centre run smoothly and assisting me in administrative matters.

Finally, I would like to thank my friends and family for their infinite love and support. I am thankful to Fanni Lengyel for keeping me grounded and supporting me through all these years. Your positive mindset is inspiring and generated encouragement in all the countless times you have been there for me. Deep and sincere gratitude to my family for their continuous love, help and support. I thank my sister Martha and my brother Michael for their encouragement, moral support and care. I am forever indebted to my parents for their endless love, dedication, encouragement that enabled me to explore new directions in life and seek my own destiny.

List of Publications

Journal Papers

A. C. Lemke, T. Leißner, A. Klick, J. Fiutowski, J.W. Radke, <u>M. Thomaschewski</u>, J. Kjelstrup-Hansen, H.-G. Rubahn and M. Bauer, *The complex dispersion relation of surface plasmon polaritons at gold/para-hexaphenylene interfaces*, Applied Physics B **116** , 585–591 (2014)

B. M. Großmann, <u>M. Thomaschewski</u>, A. Klick, A.J. Goszczak, E. K. Sobolewska, T. Leißner, J. Adam, J. Fiutowski, H.-G. Rubahn and M. Bauer, *Single-Mode to Multi-Mode Crossover in Thin-Load Polymethyl Methacrylate Plasmonic Waveguides*, Plasmonics **13** , 1441–1448 (2018)

C. <u>M. Thomaschewski</u>, Y. Yang and S.I. Bozhevolnyi, *Ultra-compact branchless plasmonic interferometers*, Nanoscale **10**, 16178-16183 (2018)

D. <u>M. Thomaschewski</u>, Y. Yang, C. Wolff, A.S. Roberts, S.I. Bozhevolnyi, *On-Chip Detection of Optical Spin–Orbit Interactions in Plasmonic Nanocircuits*, Nano Letters **19**, 1166-1171 (2019)

E. <u>M. Thomaschewski</u>, V.A. Zenin, C. Wolff, S.I. Bozhevolnyi, *Plasmonic monolithic lithium niobate directional coupler switches*, Nature Communications **11**, 748 (2020)

Conference papers and presentations

F. <u>M. Thomaschewski</u>, Y. Yang and S. I. Bozhevolnyi, *Polarization conversion within ultra-compact on-chip all-plasmonic nanocircuits*, SPIE Nanophotonics VII **10672**, SPIE Photonics Europe in Strasbourg, France, conference proceeding and poster presentation (2018)

G. <u>M. Thomaschewski</u>, Y. Yang and S. I. Bozhevolnyi, *Controlled coherent excitation of ultra-compact double plasmonic slot waveguide systems*, Nanotechnology and Innovation in Baltic Sea Region 2018 in Sønderborg, Denmark, poster presentation (2018)

H. <u>M. Thomaschewski</u>, Y. Yang, C. Wolff, A.S. Roberts, and S.I. Bozhevolnyi, *On-chip detection of photonic spin Hall dynamics in plasmonic nanocircuits*, 7th International Topical Meeting on Nanophotonics and Metamaterials in Seefeld, Austria, poster presentation (2019)

I. <u>M. Thomaschewski</u>, V.A. Zenin, S.I. Bozhevolnyi, *All-plasmonic directional coupler modulator based on strip-loaded waveguides on lithium niobate*, 9th International Conference on Surface Plasmon Photonics (SPP9) in Copenhagen, Denmark, oral presentation (2019)

J. <u>M. Thomaschewski</u>, V.A. Zenin, C. Wolff, S.I. Bozhevolnyi, *High-performance ultra-compact lithium niobate plasmonic modulators* , Nanolight in Benasque, Spain, oral presentation (2020)

Contents

List of Figures

List of Abbreviations

AFM	Atomic force microscopy
ATR	Attenuated total reflection
BTO	Barium tin oxide
CMT	Coupled-mode theory
EBL	Electron beam lithography
EM	Electromagnetic
ENZ	Epsilon-near-zero
E/O	Electrical-to-optical
EO	Eelectro-optic
EQE	External quantum efficiency
FDTD	Finite-difference time-domain
FLAG	Fiber-optic Link Around the Globe
FTTP	Fiber to the Premises
HTOL	High temperature operation lifetime
IMI	Insulator-metal-insulator
IOT	Internet of Things
IQE	Internal quantum efficiency
ITO	Indium tin oxide
LCP	Left-handed circularly polarized
LDOS	Local density of states
LN	Lithium niobate
LR-DLSPP	Long-range dielectric- loaded surface plasmon polariton
LR-SPP	Long-range surface plasmon polariton
LSP	Localized surface plasmons states
MIM	metal-insulator-metal
MZM	Mach-Zehnder modulator
O/E	Optical-to-electrical
PMMA	Poly (methyl methacrylate)
QCSE	Quantum Confined Stark Effect
RCP	Right-handed circularly polarized
SAM	Spin angular momentum
SNOM	Scanning near-field optical microscopy
SPP	Surface plasmon polariton
SR-SPP	Short-range surface plasmon polariton
WDM	Wavelength division multiplexing
WG	Waveguide

Dedicated to my parents.

Chapter 1

Introduction

1.1 The rise of the information society

In the past decades, a rapid development in digital technology caused a phenomenal increase in the volume and detail of data collected and transmitted all over the globe. The growing use of social networks, cloud computing and Internet of Things (IoT) technologies in today's information society demands a network infrastructure of huge information capacity and networks with ever-higher data transmission bandwidth. As opposed to copper cable networks where electrical pulses are used to carry data, optical data communication based on wavelength division multiplexing (WDM) technology in optical fibers utilizes near-infrared light pulses that allow data transmission rates of Tbit/s with negligible energy dissipation and high degree of transmission reliability and security. Due to these excellent characteristics, a dense global optical fiber terrestrial and submarine cable network, e.g. the Fibre-optic Link Around the Globe (FLAG), was established, which spans in total more than 2 billion kilometers (around 50000 times around our planet) and carries more than 99% of the world's intercontinental communications traffic [1].

In addition to the long-haul transcontinental network, optical communication within short-haul applications like Fiber to the Premises (FTTP), inter- and intra-rack transmission, shelf-to-shelf, and eventually intra-chip optical interconnects has been established.

At the linking fiber nodes of our long-haul, terrestrial optical fiber network, enormous data centers store, process and distribute data and information. Since most of the data is still electrically processed and stored, a conversion of the optical signal to an electrical signal, followed by re-routing in the electrical domain and finally electro-optic conversion back to the optical domain are required. The fundamental reasons for this division of labour is the small energy needed to transmit information in the form of photons while electronic components provide much more compact computing and storing capabilities than photonics. The data translation is realized by electro-optic devices which function as electrical-to-optical (E/O) or optical-to-electrical (O/E) signal transducers (Figure 1.1). Considering hundreds of thousands of optical fiber links in such processing centers, highly miniaturized device geometries are of paramount importance. In fact, scalability and bandwidth limitations are the major challenges faced towards meeting the requirements of optical-interconnect modules in future data centers. Operation in harsh environments, such as high temperatures, imply further requirements such as stable thermal and mechanical properties e.g. defined by the Telecordia HTOL (high temperature operation lifetime) testing the operation at 85°C for 2000 hours [2].

Another major concern is the power consumption of the devices which significantly contribute to the overall power consumption in data communication. Already today, between 5% and 9% of global energy consumption is due to the information and communications technology sector which, by 2030, will increase to 20%, accounting for up to 5% of all carbon emissions [3].
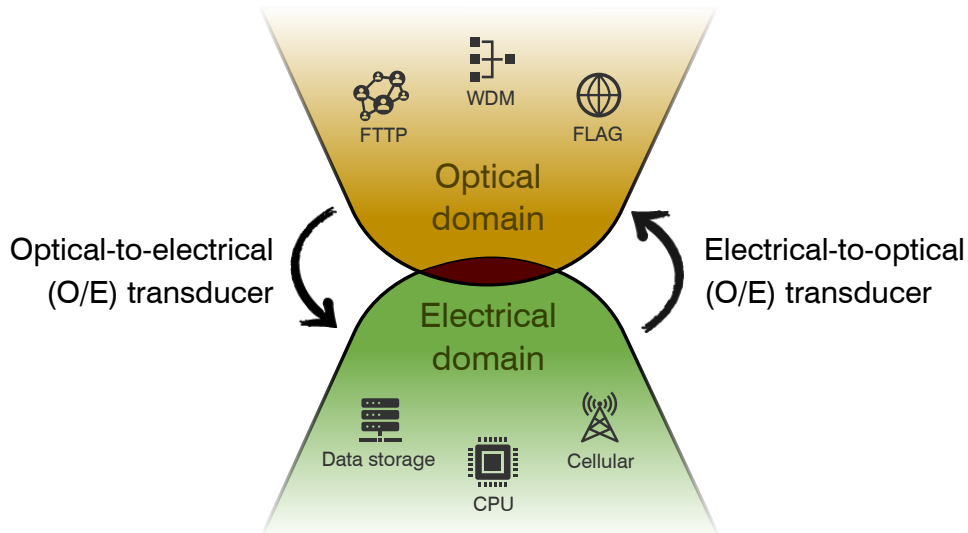
FIGURE 1.1: The purpose of optical-to-electrical and electrical-to-optical (plasmonic) transducers is to convert optical signals into the electrical domain, and vice versa. A seamless integration of optical and electronic technologies requires compact, broadband and low-power opto-electronic devices.

To support the insatiable demand of enourmous density of optical interfaces, it is crucial to improve the performance of electro-optic devices in terms of efficiency, compactness, speed and energy-consumption. Nanophotonic technologies represent a qualitative leap forward in the design of future optical communication systems addressing the growing demand for high bandwidth, small device footprint and low energy consumption [4]. However, this approach still needs to overcome several hurdles for the practical realization of highly-integrated electro-optic devices. This includes the size mismatch between micrometer-scale bulky components of photonics and nanometer-scale electronic chips. Dielectric photonic devices and systems are limited in reduction in size by the fundamental laws of diffraction to about half a wavelength of light. This is about one or two orders of magnitude larger than their nanoscale electronic counterparts, which are only limited by quantum mechanical electron tunneling within nm spacings. Furthermore, the potential of enhanced light–matter interaction in nanophotonic devices is largely underexploited. Research in the field of nanophotonics is aiming for a substantial miniaturization of photonic components, but also for improvements of optoelectronic device performances.

Plasmonics as a separate branch of nanophotonics has the potential of merging the fields of photonics and electronics at the nanoscale, with the attribute of offering highly-confined optical and electrical signal transmission in the same metallic nanostructure, enabling unprecedented bandwidth and miniaturization potentials [5].

1.2   Glamour of plasmonics

On December 29$^{\text{th}}$, 1959, future Nobel laureate Richard Feynman considered in his lecture "There's Plenty of Room at the Bottom: An Invitation to Enter a New Field of Physics" the possibility of manufacturing miniaturized devices and nanosystems and inspired the new field of nanoscience and nanotechnology [6], associated to the study and engineering of matter, particles and structures on the nanometer scale. He not only imagined this new field, but he also had an idea on how it could be implemented and what tremendous
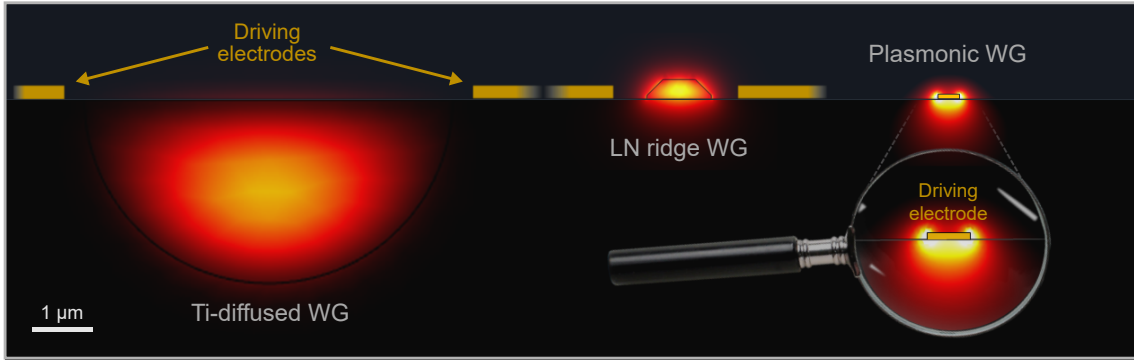
FIGURE 1.2: The trend towards further miniaturisation of lithium niobate (LN) electro-optic modulators at $\lambda = 1.55\ \mu$m. From the early success of Ti-diffused waveguides in lithium niobate, recently developed LN ridge waveguide drastically decreased the mode size, and therefore improved the overall device performance of electro-optic modulators. The proposed plasmonic lithium niobate modulator elegantly unifies the driving electrode with the optical waveguide, enabling exceptionally compact and efficient device performances.

role it could play in future science and technologies. For instance, he suggested to use beams of electrons to etch lines with the width of a few atoms. This technique became an ubiquitous nanofabrication processes, later called electron beam lithography (EBL), and is used in this thesis as a tool for the fabrication of nanophotonic circuitry. In fact, by then, rapid conceptual developments and progress in nanofabrication technologies had brought many revolutionary developments in physics that successfully demonstrated Feynman's ideas.

One field which emerged from the nanotechnology revolution is the field of nanophotonics that encompasses the science and engineering of optical interactions with nanostructures. Plasmonics, as a subfield of nanophotonics particularly related to the study of the unique optical properties of metal nanostructures with subwavelength dimension, enables a broad range of fascinating applications in photonics (light manipulation and control) or optoelectronics. It is a crucial feature in these applications, that electromagnetic (plasmonic) waves that propagate along metal-dielectric interfaces can be guided beyond the diffraction limit. This can be understood by expressing the uncertainty principle (or likewise the Fourier transformation)

$$\Delta(\hbar k_x)\Delta x \geq \hbar/2 \tag{1.1}$$

in one direction for the wavevector $k = \sqrt{k_x^2 + k_y^2 + k_z^2}$ with the spatial components k_i with $i = x, y, z$. This expression says that the product of the smallest size Δx to which a plane wave can be focused in one dimension and the maximum possible spread of the wavevector component Δk_x cannot become arbitrarily small. Due to the evanecent wave nature of plasmonics, at least one spatial component of the wave vector is imaginary, thus providing larger spatial components k_j in the other directions. Hence, the minimal possible size Δx decreases according to Equation 1.1 for electromagnetic waves bound to metallic surfaces, compared to a freely propagating electromagnetic wave. This offers a drastic improvement in size reduction of optical systems facilitated by plasmonic sub-diffraction light confinement and accordingly addresses the size mismatch between current electronic and photonic components.

Furthermore, plasmonic circuitry offers the opportunity of carrying optical signals

and electrical signals in the same metallic structure, thus enabling highly-integrated elec-tro-optically active devices, such as plasmonic photodetectors or modulators which can fulfill the demands of future O/E and E/O transducers. The seamless transition from the optical (plasmonic) domain into the electrical domain (and vice versa) is provided by plasmonic-assisted devices that merge photonic and electronic circuitry into ultra-compact scales.

To illustrate the miniaturzation potential of plasmonics, current integrated optical platforms for electro-optic modulation are compared with the plasmonic system pro-posed in this thesis (Figure 1.2). Optical waveguides formed by the diffusion of tita-nium oxide in lithium niobate are a widely spread technology, exhibiting large modal sizes of several μm^2. The driving electrodes are located around the optical mode, leading to a poor overlap between the optical and electrostatic fields. This substantially lim-its the overall device performance for electro-optic modulation. The same applies for the recently emerged technology of lithium niobate ridge waveguides: although exhibit-ing significantly higher optical confinement, they still demand relatively long (on the mm-scale) interaction lengths due to their fundamental limits in electro-optic efficiency. Unifying the optical sub-diffraction (plasmonic) waveguide consisting of a metal stripe with the driving electrode provides a tremendous miniaturisation potential. This ap-proach promises substantial improvement in device performance regarding speed, effi-ciency and energy consumption due to the strong light-matter interaction and a large overlap integral between the enhanced optical and electrostatic fields provided by the same metallic nanostructures. In the course of this thesis, several types of plasmonic electro-optic devices are proposed and developed.

Chapter 2

Fundamentals of plasmonics

This chapter presents the main theoretical aspects of electromagnetic (EM) waves in metal/dielectric interfaces and their interaction with matter. Starting from the basis of electromagnetics through Maxwell's equations and light propagation in anisotropic crystals, a brief introduction of the field of plasmonics and the main characteristic features are provided. We introduce the concept of surface plasmon polaritons (SPP), discuss several types of SPP supported by plasmonic waveguides and their excitation methods.

2.1 Maxwell's equations and electromagnetic wave propagation

The fundamental property of matter that causes interaction with electromagnetic fields is the electric charge. In particular, a particle of charge q and speed v is subject to the Lorentz force

$$\mathbf{F} = q(\mathbf{E} + \mathbf{v} \times \mathbf{B}),$$ (2.1)

where $\mathbf{E}$ and $\mathbf{B}$ are the electric and magnetic field vectors in three-dimensional space, respectively. Together with Maxwell's equations of macroscopic electromagnetism in the modern form, here written in SI units

$$\nabla \cdot \mathbf{D} = \rho_{ext}$$

$$\nabla \cdot \mathbf{B} = 0$$

$$\nabla \times \mathbf{E} = -\frac{\partial \mathbf{B}}{\partial t}$$ (2.2)

$$\nabla \times \mathbf{H} = \frac{\partial \mathbf{D}}{\partial t} + \mathbf{J_{ext}},$$

the above listed equations constitute the foundation of classical electrodynamics. The Maxwell's equations 2.2 link the dielectric displacement $\mathbf{D}$, the electric field $\mathbf{E}$, the magnetic induction $\mathbf{B}$ and the magnetizing field $\mathbf{H}$ with the external charge and current density, ρ_{ext} and $\mathbf{J_{ext}}$, respectively. All fields are functions of space ($\mathbf{r}$) and time (t). Hereby, the charge density and the charge current density in a medium obey the continuity equation

$$\frac{\partial \rho_{ext}(\mathbf{r},t)}{\partial t} + \nabla \cdot \mathbf{J_{ext}}(\mathbf{r},t) = 0.$$ (2.3)

In order to apply the above equation in a particular optical material, Maxwell's equations are supplemented by the constitutive relations which describe the influence of the

material media on the electromagnetic fields by

$$\mathbf{D} = \epsilon_0 \mathbf{E} + \mathbf{P}$$

$$\mathbf{H} = \frac{1}{\mu_0} \mathbf{B} - \mathbf{M},$$

(2.4)

that define the relationship between the pairs of fields, namely the electric displacement field $\mathbf{D}$ and magnetizing field $\mathbf{H}$ with the electric field and magnetic induction and the electromagnetic response of a material, where $\epsilon_0 = 8.85 \times 10^{-6}\,\mathrm{A\,s\,V^{-1}\,m^{-1}}$ is the vacuum permittivity and $\mu_0 = 1.26 \times 10^{-6}\,\mathrm{V\,s\,A^{-1}\,m^{-1}}$ is the vacuum permeability. The latter two are connected to the speed of light in vacuum by

$$c = \frac{1}{\sqrt{\epsilon_0 \mu_0}}.$$

(2.5)

The material's optical response is represented by the electrical polarization and magnetization. They can be defined by the electrical dipole moment $d\mathbf{p}$ and the magnetic dipole moment $d\mathbf{m}$ per volume element dV, respectively:

$$\mathbf{P} = \frac{d\mathbf{p}}{dV} = \epsilon_0 \chi^{(1)} \mathbf{E}$$

$$\mathbf{M} = \frac{d\mathbf{m}}{dV} = \chi_m^{(1)} \mathbf{H}.$$

(2.6)

The term on the right-hand side are first-order Taylor expansions of $\mathbf{P}$ and $\mathbf{M}$ as a function of the electric and magnetic field, respectively. This approximation is only describing the linear response of the electric susceptibility $\chi = \chi^{(1)}$ and magnetic susceptibility $\chi_m = \chi_m^{(1)}$. Non-linear effects are taken into account by introducing higher-order terms to the response function of the polarization and magnetization, as it will be later discussed in Chapter 3.2.1.

Combining the equations 2.4 and 2.6, leads to

$$\mathbf{D} = \epsilon_0 \epsilon_r \mathbf{E}$$

$$\mathbf{B} = \mu_0 \mu_r \mathbf{H},$$

(2.7)

with $\chi^{(1)} = \epsilon_r^{(1)} - 1$ and $\chi_m^{(1)} = \mu_r^{(1)} - 1$, where $\epsilon = \epsilon_r^{(1)} \epsilon_0$ and $\mu = \mu_r^{(1)} \mu_0$ are the linear dielectric function and magnetic permeability which are in general complex and dependent on the angular frequency ω, respectively. For simplicity, in the following we assume a non-magnetic media, i.e. $\mu_r = 1$ and consequently $\mathbf{M} = 0$. Furthermore, we assume fields with harmonic time dependence $e^{-i\omega t}$ so that

$$\mathbf{E} = \tilde{\mathbf{E}}_0 e^{i(-\omega t + \phi)},$$

(2.8)

with the amplitude $\tilde{E}_0$ and the phase ϕ. By separating the phase ϕ from the exponential argument, we can rewrite Equation 2.8 to

$$\mathbf{E} = \tilde{\mathbf{E}}_0 e^{i(-\omega t + \phi)} = \mathbf{E}_0 e^{-i\omega t}.$$

(2.9)
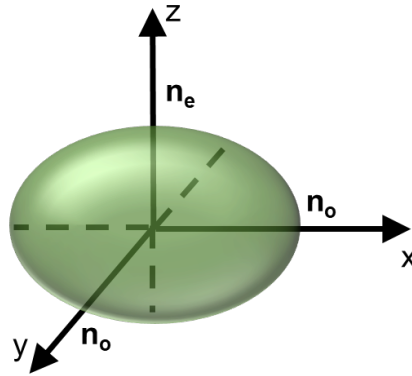
FIGURE 2.1: Refractive index ellipsoid of a negative birefringent material ($\epsilon_e < \epsilon_o$). Rotating a uniaxial material around the optic axis (z-axis) does not change its optical properties.

If the field is present in a uniform, isotropic, and linear medium, then we can derive the Helmholtz equation

$$\nabla^2 \mathbf{E} + \epsilon_r(\omega) \left(\frac{\omega}{c}\right)^2 \mathbf{E} = 0. \tag{2.10}$$

A solution of Equation 2.10 in a domain consisting of an arrangement of different materials can be found under consideration of appropriate boundary conditions at the interface between two media. This is further investigated in Chapter 2.3, where a solution for an electro-magnetic wave (surface plasmon polariton, SPP) propagating along a metal-dielectric interface is found that satisfies the Helmholz equation under consideration of the corresponding boundary conditions.

For plane waves propagating in the z-direction, i.e. with the possible solution $\mathbf{E} = \tilde{\mathbf{E}}_0 e^{i(kz-\omega t)}$, we obtain the relationship between the wave number k and the frequency ω

$$k(\omega) = k_0 \sqrt{\epsilon_r(\omega)} = \left(\frac{2\pi}{\lambda}\right) \sqrt{\epsilon_r(\omega)} = \left(\frac{2\pi}{\lambda}\right) n(\omega). \tag{2.11}$$

From Equation 2.11, we can define the phase velocity

$$v_{ph} = \frac{\omega}{k(\omega)} = \frac{1}{\sqrt{\epsilon_r(\omega)}} = \frac{c}{n(\omega)}, \tag{2.12}$$

with the complex refractive index

$$n(\omega) = n'(\omega) + in''(\omega) = \sqrt{\epsilon_r(\omega)}. \tag{2.13}$$

More generally, $\mathbf{D}$ can be dependent on the orientation of the electric field. The constitutive relation between the displacement $\mathbf{D}$ and the electric field vector $\mathbf{E}$ may then be written in matrix form

$$\begin{pmatrix} D_x \\ D_y \\ D_z \end{pmatrix} = \begin{pmatrix} \epsilon_{xx} & \epsilon_{xy} & \epsilon_{xz} \\ \epsilon_{yx} & \epsilon_{yy} & \epsilon_{yz} \\ \epsilon_{zx} & \epsilon_{zy} & \epsilon_{zz} \end{pmatrix} \begin{pmatrix} E_x \\ E_y \\ E_z \end{pmatrix}. \tag{2.14}$$

in which the permittivity has become a second-rank tensor. By diagonalizing the permittivity matrix in Equation 2.14, we obtain a simplified relationship derived by rotation

into the principal axis of the medium:

$$\epsilon = \begin{pmatrix} \epsilon_{11} & 0 & 0 \\ 0 & \epsilon_{22} & 0 \\ 0 & 0 & \epsilon_{33} \end{pmatrix} \xrightarrow[\text{crystal}]{\text{uniaxial}} \begin{pmatrix} \epsilon_o & 0 & 0 \\ 0 & \epsilon_o & 0 \\ 0 & 0 & \epsilon_e \end{pmatrix} = \epsilon_0 \begin{pmatrix} n_o^2 & 0 & 0 \\ 0 & n_o^2 & 0 \\ 0 & 0 & n_e^2 \end{pmatrix}. \tag{2.15}$$

When all elements of the tensor are equal, the material is said to be isotropic. In an uniaxial (birefringent) material (tetragonal, trigonal and hexagonal crystals, e.g. $LiNbO_3$), two of the diagonal entries of the permittivity matrix are equal and one is different. Then the material possesses two ordinary principal axes governed by the ordinary permittivity ϵ_o and one extraordinary (optic) axis governed by the extrodinary permittivity ϵ_e. The material has a positive birefringence when $\epsilon_o > \epsilon_e$, while a negative birefringence means $\epsilon_o < \epsilon_e$. For birefringent materials, it is common to state the ordinary and extraordinary refractive index (Equation 2.15). The quadratic refractive index tensor can then be represented by the index ellipsoid

$$\frac{x^2}{n_x^2} + \frac{y^2}{n_y^2} + \frac{x^2}{n_x^2} = 1, \tag{2.16}$$

with the principal crystal axis used as the coordinate system. The optical properties of a material can be described by the index ellipsoid depicting the orientation and relative magnitude of refractive indices in the uniaxial crystal (Figure 2.1). Are all tensor elements unique, the material is said to be biaxial (e.g. triclinic, monoclinic and orthorhombic crystals).

2.2   Optical properties of noble metals

In metals, the majority of optical effects can be described by the classical free-electron model. In this model, the electrons in the material are treated as point-like particles freely-moving around fixed ions within the metal. The immobile positively charged ions comprise the crystal's lattice in the solid. Paul Drude (1863 - 1906) described in his model [7, 8], that the electrons behaviour in such a system is expressed through the differential equation

$$m_e \frac{\partial^2 \mathbf{r}}{\partial t^2} + m_e \gamma \frac{\partial \mathbf{r}}{\partial t} = e \mathbf{E} e^{-i\omega t}, \tag{2.17}$$

where e and m_e are the charge and effective mass of the free electron, respectively, and γ is the term which describes friction or damping of the electrons. The concept of the effective electron mass allows to treat the electrons as quasi-particles composed of collective excitations of the interacting electrons, and are therefore treated as if they were freely moving around the background of heavy immobile ions. Assuming that the solution for the electron's position $\mathbf{r}$ has a harmonic behaviour $\mathbf{r} = \tilde{\mathbf{r}} e^{i\omega t}$ when interacting with the harmonic electric field $\mathbf{E} = \tilde{\mathbf{E}} e^{i\omega t}$, one can rewrite the Drude Equation 2.17 as

$$\left(-m_e \omega^2 - i m_e \omega \gamma \right) \tilde{\mathbf{r}} = e \tilde{\mathbf{E}}. \tag{2.18}$$

The origin of a macroscopic polarization lies in the formation of a number of individual dipoles (N dipoles per unit volume) associated with a dipole moment $d(\mathbf{r}) = e\mathbf{r}$. The resulting macroscopic polarization $\mathbf{P}$ can be expressed for N linear individual dipoles per unit volume as

$$\mathbf{P} = \epsilon_0 \chi^{(1)}(\omega) \mathbf{E} = N d(\mathbf{r}) = N e \mathbf{r}. \tag{2.19}$$

Combining Equation 2.17 and 2.19 leads to

$$\frac{-e^2 N}{m_e \omega^2 + i\omega\gamma m_e}\mathbf{E} = Ne\mathbf{r},\tag{2.20}$$

from which the linear susceptibility

$$\chi^{(1)}(\omega) = \frac{-e^2 N}{m_e \epsilon_0 (\omega^2 + i\omega\gamma)}\tag{2.21}$$

and the dielectric function

$$\epsilon(\omega) = 1 + \chi^{(1)} = 1 + \frac{-e^2 N}{m_e \epsilon_0 (\omega^2 + i\omega\gamma)} = 1 - \frac{\omega_p^2}{\omega(\omega + i\gamma)}\tag{2.22}$$

can be extracted. The plasma frequency in Equation 2.22 is defined as

$$\omega_p = \sqrt{\frac{e^2 N}{m_e \epsilon_0}}\,.\tag{2.23}$$

The solutions of Equation 2.22 in the high-frequency limit $\omega \to \infty$ according to which the permittivity should become

$$\epsilon(\infty) = \epsilon_\infty = 1\,,\tag{2.24}$$

results to the same permittivity as in vacuum. The Drude model explains this by the charge carriers which cannot instantaneously respond to a rapidly varying electric field. Thus, electromagnetic waves with high-frequencies are propagating without any notice of the material (as in vacuum). By considering a residual polarization $\mathbf{P}_\infty = \epsilon_0(\epsilon_\infty - 1)$ in the metal due to the positive background of the ions, we can describe the total polarization by including the material specific high-frequency permittivity ϵ_∞ to the Drude Equation 2.22 and we obtain

$$\epsilon(\omega) = \epsilon_\infty - \frac{\omega_p^2}{\omega(\omega + i\gamma)}\,.\tag{2.25}$$

At low frequencies $\gamma \ll \omega$, we can simplify this equation to

$$\epsilon(\omega) = \epsilon_\infty - \left(\frac{\omega_p}{\omega}\right)^2,\tag{2.26}$$

which is in the following referred as plasma-model without damping. As is it described later in Chapter 2.3, it is desired for practical plasmonic applications that the real part of the dielectric function is negative, which is satisfied if the targeted frequency of interest is smaller than the plasma frequency. Therefore, Equation 2.26 is commonly used to describe the optical response of the medium at the frequency regime which is relevant for the study of propagating plasmonic modes. Note that the plasma frequency ω_p, the damping term γ and the high-frequency permittivity ϵ_∞ are depending on the specific meterial. Table 2.1 summarizes the parameters for the commonly used metals in the field of plasmonics. The applicability of the free-electron Drude model is examined in Figure 2.2, by comparing the real in imaginary components of the permitivitty for the most relevant metals in plasmonics (gold, silver, aluminum - while gold is chemically stable, silver and aluminium oxidizes rapidly, therefore leading to deteriorated optical properties). Evidently at low frequencies, the Drude model provides excellent quantitative description of the essential optical features. When approaching the visible spectral

TABLE 2.1: The parameters for the Drude-like permittivity of gold, silver and aluminum [9]

	ω_∞	$\omega_p(eV)$	$\omega_p(10^{15}s^{-1})$	$\gamma(10^{15}s^{-1})$	$\omega_{int}(eV)$
Gold	10	9,1	13.8	0.011	2.3
Silver	3.8	9.1	14.0	0.032	3.9
Aluminum	1	15.1	22.9	0.91	1.41
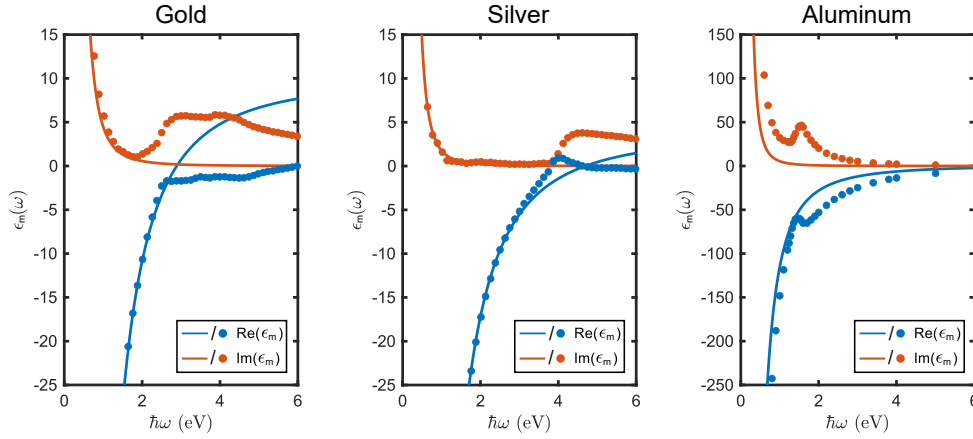
FIGURE 2.2: The Drude model in comparison with experimentally measured permittivites for gold, silver and aluminum. The experimental data for gold and silver are taken from the measurements of Johnson and Christy [10] and for aluminum from Rakié [11]. The colored circles correspond to experimentally determined values and the Drude model curves are obtained by using Equation 2.25 with the material parameters in Table 2.1.

range ($\hbar\omega \approx 2.0\text{eV}$ corresponding to a wavelength of about 620 nm) in the case of gold, the free-electron model begins to fail due to interband transitions, i.e. the excitation of electrons from lower-lying bands into higher empty energy levels. This leads to a significant contribution to the optical response and is going beyond the description provided by the Drude model. The transitions are driven by absorption of photons, thus leading to a rapid increase of the imaginary part of the dielectric function. In practice, corrections for the interband transitions are described by summed Lorentzian oscillator terms

$$\sum_n \frac{f_n\omega_n^2}{\omega_n^2 - \omega(\omega + i\gamma_n)}, \tag{2.27}$$

with oscillator strengths f_n, transition frequencies ω_n, and decay rates γ_n. When combined with the Drude model, the description is typically referred to as the Lorentz–Drude model. The frequencies ω_{int} at which interband transitions occur are listed in 2.1 for the considered materials. Are the frequencies of interest below the onset of those interband transitions, the Drude model serves as a simple model which can explain the main features of the optical response in metals.

2.3 Surface plasmon polaritons at metallic interfaces

In the previous section it has been shown how electromagnetic fields can lead to collective oscillations of the free electron gas of a metal. For the derivation of surface plasmon polaritons, we consider for now the simplest case of a single interface of a metal and a dielectric with semi-infinitely extended media on either side (Figure 2.3). Therefore, we assume a propagation along the $y = 0$ plane in z-direction (i.e. $k_x = 0$). Furthermore, we consider only a transverse-magnetic solution (TM) mode, as it can be shown that no transverse-electric solution exists for a plain surface mode. For the TM mode $\mathbf{k} \cdot \mathbf{H} = k_y H_y + k_z H_z$ holds and the time-independent electric field consequently reads

$$\mathbf{E}(x,y,z) = \begin{cases} \mathbf{E_0} e^{(ik_{SPP}z + \kappa_d y)} \text{ for } y \geq 0 \\ \mathbf{E_0} e^{(ik_{SPP}z + \kappa_m y)} \text{ for } y \leq 0 \,, \end{cases} \tag{2.28}$$

where the imaginary part of $k_y = \kappa_d$ and $k_y = \kappa_m$ causes an exponential decay of the electric field into both media, the dielectric and the metal, respectively, with its maximum at the metal/dielectric interface (Figure 2.3). For a bounded propagating mode and under consideration of the boundary condition for the normal electric-field components at the interface, one can find the following implicit condition for the SPP dispersion relation

$$\frac{k_{y,d}}{\epsilon_d} = \frac{k_{y,m}}{\epsilon_m} \,. \tag{2.29}$$

The propagation along the interface (z-axis) is described by the wave number $k_z = k_{SPP} = k'_{SPP} + ik''_{SPP}$, which is also stated as the propagation constant β. To put this in relation with the free-space wave number k_0, we introduce the mode effective index n_{eff}, which follows the relation

$$k_{spp} = n_{eff} k_0 \,. \tag{2.30}$$

Generally, the propagation constant $k_{SPP} = k'_{SPP} + ik'_{SPP}$ and the mode effective index $n_{eff} = n'_{eff} + in''_{eff}$ are complex. The real part of k'_{SPP} determines the wavelength of the propagating SPP

$$\lambda_{SPP} = \frac{2\pi}{k'_{SPP}} = \frac{\lambda_0}{n'_{eff}} \,, \tag{2.31}$$

which is smaller than the wavelength of freely-propagating light in the corresponding dielectric ($\lambda_{SPP} < \lambda = \lambda_0/\epsilon_d$). The imaginary part k''_{SPP} defines the intensity propagation length

$$L_{SPP} = \frac{1}{2k''_{SPP}} = \frac{\lambda}{4\pi n''_{eff}} \,, \tag{2.32}$$

which represents the length over which the intensity of the SPP is decreased along the propagation direction to $1/e$ of its maximum value.

By inserting Equation 2.28 into the Helmholtz Equation 2.10, while ensuring the continuity conditions of the field components at the metal/dielectric interface, one can find an expression for the wave vector

$$k_{SPP} = \frac{\omega}{c} \sqrt{\frac{\epsilon_m(\omega)\epsilon_d(\omega)}{\epsilon_m(\omega) + \epsilon_d(\omega)}} \,, \tag{2.33}$$

with frequency-dependent complex permittivities $\epsilon_m(\omega)$ and $\epsilon_d(\omega)$ of the metal and the dielectric, respectively. For a surface mode to exist in this configuration, one can show
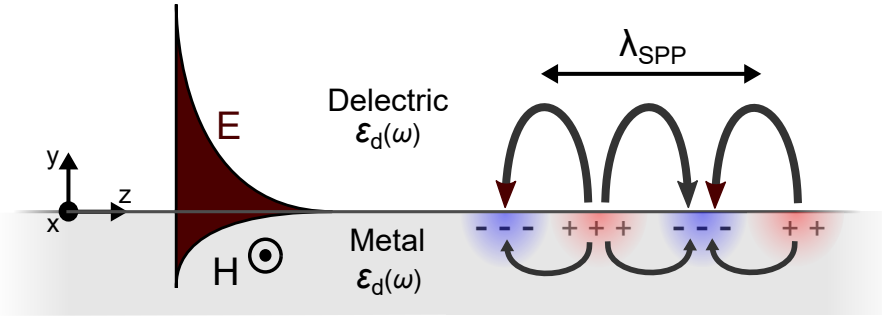
FIGURE 2.3: Schematic illustration of the intensity distribution and
the electric field of a surface plasmon polariton supported by a
metal/dielectric interface; ϵ_m and ϵ_d denote the permittivity of the metal
and dielectric material, respectively. The SPP intensity decreases exponen-
tially into both media. The mode has electric field components normal
to the interface (y-axis) and along the propagation direction (z-axis). The
magnetic field H is oriented perpendicular to the direction of propagation,
exhibiting the transverse magnetic (TM) nature of SPPs.

that the two conditions

$$\text{Re}(\epsilon_m + \epsilon_d) < 0 \text{ and } \text{Re}(\epsilon_m \epsilon_d) < 0 \tag{2.34}$$

must be fulfilled. Consequently, the required condition of the dielectric function of the
metal is

$$\text{Re}(\epsilon_m(\omega)) < -\epsilon_d, \tag{2.35}$$

which is fulfilled for the most metals at the small frequency-regime (Figure 2.2) where

$$\omega < \frac{\omega_p}{\sqrt{2}} = \omega_{sp}, \tag{2.36}$$

defining the surface plasmon frequency ω_{sp} (SPP resonance). Given the dielectric func-
tion ϵ_m for a Drude metal fitted to the optical properties of gold and the permittivity
of vacuum $\epsilon_0 = 1$, one can calculate the dispersion relation for surface plasmon polari-
tons propagating along an Au/vacuum interface (Figure 2.4). In the lossless case (Figure
2.4a), there are two distinct branches of the dispersion relation. One branch, located left
to the light line and above the plasma frequency, corresponds to bulk plasmon polaritons,
where the optical field is coupled to the internal degrees of freedom of the plasma, induc-
ing oscillation of free electrons along the bulk of a metal. The other branch corresponds
to surface plasmon polaritons as surface electromagnetic waves coupled to collective os-
cillations of the free electrons in the metal.

Crucially, the dispersion of SPPs and the light line do not intersect, which means
that there is a momentum mismatch of freely propagating light and surface plasmon
polaritons. This means that a freely propagating electromagnetic wave cannot excite
SPPs by simply irradiating the metal surface since this would violate the conservation
of momentum and energy. Hence, alternative methods are needed for generating SPPs
with freely propagating light. Some relevant methods that have been used to excite SPPs
in various waveguide architectures in this thesis are described in Chapter 2.5. Note that
SPPs, like all evanescent waves which have an imaginary longitudinal component of the
electric field $E_y = i\frac{k_z}{\kappa}E_z$ with the complex wave vector $\mathbf{k} = k_z\hat{\mathbf{z}} + i\kappa\hat{\mathbf{y}}$, intrinsically bears
a transverse spin as they exhibit a rotation of the electric-field vector in the (y-z)-plane
which is fundamentally locked to the propagation direction (z-direction). Thereby, one
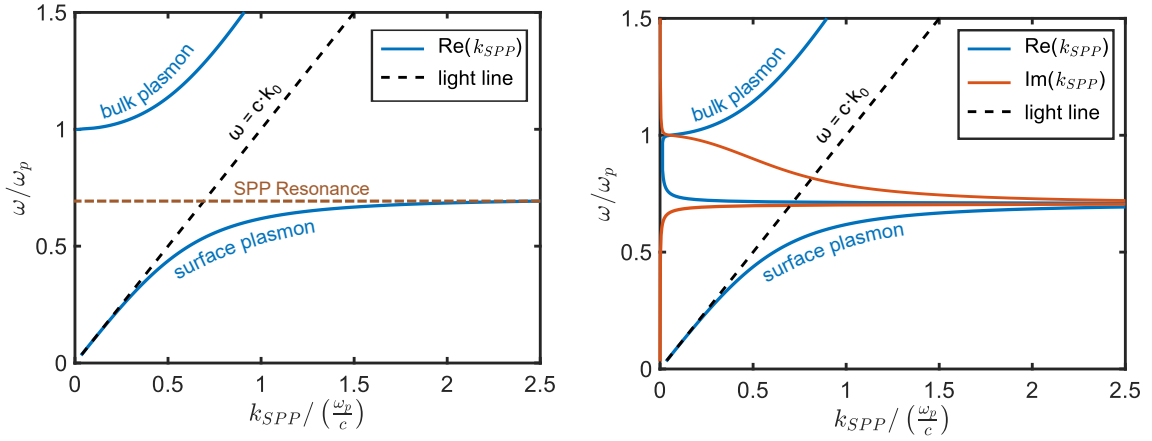
FIGURE 2.4: Dispersion of surface plasmon polaritons propagating along metal/dielectric interface for a lossless and lossy Drude metal response fitted to the properties of gold.

can associate a spin angular momentum (SAM) directed orthogonal to the propagation direction of the SPP. Taking into account both electric and magnetic contributions, the transverse SAM can be written in the universal form [12]:

$$\mathbf{s}_\perp = \frac{\text{Re}(\mathbf{k}) \times \text{Im}(\mathbf{k})}{\text{Re}(\mathbf{k})^2} \ . \tag{2.37}$$

The photonic spin-momentum locking described by Equation 2.37 holds the analogy to the electronic quantum spin-Hall effect, where the spin of electrons causes a unidirectional edge spin transport, i.e. the edge states with opposite spins propagating in opposite directions. Here, the plasmonic (evanescent) waves propagating in +z direction with the wave vector $k_z > 0$ and the wave propagating in opposite direction (-z direction) with $k_z < 0$ are having opposite transverse spins $s_\perp > 0$ and $s_\perp < 0$, respectively. This suggests to utilize the reverse scheme for spin-dependent unidirectional plasmonic excitation, where the spin of irradiating photons (tied to the handedness of circularily polarized light) is coupling to the transverse spin of surface plasmon polaritons, and are consequently unidirectionally excited by the incident radiation. This excitation scheme is further describes in section 2.5.

2.4 Waveguide architectures based on surface plasmon polaritons

In the previous section, we have introduced the most simple waveguide configuration consisting of an infinitely wide metal/dielectric interface which can support a propagating plasmonic wave. For practical applications, however, it is essential to confine SPPs laterally by structuring the material, which eventually allows more complex and operational plasmonic circuitry on small footprints i.e. for subwavelength on-chip optical communication. To date, a variety of plasmonic waveguide architectures differing in terms of topology or the material composition has been proposed and investigated. These include insulator-metal-insulator (IMI), metal-insulator-metal (MIM), metal slot, metal strip and dielectric-loaded surface plasmon polariton (DLSPP) waveguides. It is evident that due to the structural diversity, e.g. their individual topology and materials composition, each waveguide architecture possesses different waveguiding characteristics, such as mode

confinement and propagation length. Therefore, it is important to investigate the waveguide characteristics for choosing the appropriate type of plasmonic waveguide suiting the specific application. Generally, the key challenge of choosing and designing the appropriate waveguide architecture is the trade-off between the optical confinement and the propagation losses.

We evaluate the geometrical dependence on the waveguide characteristics for several waveguide architectures. Here, three different waveguide architectures deserve special attention, as they are the most relevant within the scope of this thesis. Those are the plasmonic slot waveguides, metal strip waveguides and long-range dielectric-loaded SPP waveguides. Firstly, plasmonic slot waveguides, which are composed of a subwavelength slot in a thin metallic film, have been used as a waveguide platform for ultracompact Mach-Zehnder interferometers (see Appendix A or [13]) and for on-chip detection of spin-selective routing in plasmonic circuitry (see Appendix B or [14]). Secondly, metal strip waveguides, consisting of a metal nanowire supported by a dielectric substrate, serve as the main building block for on-chip lithium niobate plasmonic modulation (see Appendix C or [15]). Finally, we propose low-loss plasmonic modulators based on long-range dielectric-loaded SPP waveguides (Chapter 3.2.4).

To get insights into the propagation characteristics accompanied by those waveguide geometries, we study the mode effective index n_{eff} (which in the following shall only refer to the real part), the propagation losses and the optical confinement depending on the material composition and geometrical shape by numerically calculating the eigenmodes in the particular geometry using a finite element method solver (Comsol Multiphysics 5.2a). The optical response of a medium is included in this model by assigning the bulk dielectric constants to the specific geometrical domain. The dielectric permittivities of Au, SiO_2, Ge and $LiNbO_3$ for telecommunication wavelengths are provided by Johnson and Christy [10], Maltitson [16], Nunley et al. [17] and Zelmon et al.[18], respectively. Throughout this chapter, the vacuum wavelength is assumed to be $\lambda_0 = 1550$ nm, i.e. the targeted operation wavelength of the plasmonic devices in this thesis. It is evident that the waveguide geometry and the choice of the materials that form the waveguides, strongly affects the modes propagation properties. For instance, geometric squeezing of the optical fields to the metal surface leads to a enhanced mode confinement, which however is accompanied by increased transmission losses due to resistive heating in the metal. In order to consistently quantify the optical confinement, we calculate the mode effective index, the propagation losses and the effective mode area defined by

$$A_{\text{eff}} = \frac{\left[\int_\infty E(r)^2 \mathrm{d}A\right]^2}{\int_\infty E(r)^4 \mathrm{d}A}, \tag{2.38}$$

where $E(r)$ is the transverse electric field components in the cross section of the waveguide at position r. This quantity provides a quantitative measure of the area which is covered by the waveguide mode in its transverse plane and allows a fair comparison of different waveguide geometries. Note that the mode field area for plasmonic waveguides investigated in this chapter is usually smaller than the diffraction-limited mode area defined as

$$A_0 = \left(\frac{\lambda_0}{2n}\right)^2 = \frac{\lambda_0^2}{4}, \tag{2.39}$$

with the free-space wavelength λ_0. The capability of these waveguides to strongly confine the mode to sizes more than 100 times smaller than the area of a diffraction-limited beam is crucial for the realization of the compact active plasmonic devices presented in

this thesis.

2.4.1 Slot waveguide

The slot waveguide (also known as gap or channel waveguide) can provide extreme field concentration of the electromagnetic mode localized in a deep subwavelength dielectric gap between two metal strips (Figure 2.5). For the symmetric slot waveguide, the metal film is embedded in an infinite homogeneous dielectric. The calculated mode profile in the cross section reveals that the mode is strongly concentrated in the slot region and only slightly extends in the adjacent dielectric region above and below the slot (Figure 2.5b). This fundamental mode supported by the symmetric architecture is always a bound mode regardless of the thickness of the metal.

The asymmetric structure, in which the surrounding dielectric materials above and below the metal film are different (e.g. with unequal permittivities), exhibits a cutoff metal film gap below which the mode becomes leaky. In particular for a slot waveguide supported by a SiO_2 substrate without an index-matching dielectric cladding layer ($n_1 = n_{air} = 1$), the cutoff gap width for a 100 nm thick slot is 60 nm, with an optical loss of 0.7 dB/μm at $\lambda_0 = 1550$ nm. Considering the practical limitations on fabrication, and significant optical loss at small waveguide gaps, we apply a dielectric cladding consisting of 300 nm thick Poly(methyl methacrylate) (PMMA), which has a refractive index ($n_{PMMA} = 1.49$) and is therefore similar to to refractive index of SiO_2 ($n_{SiO_2} = 1.44$). In this configuration, the waveguiding characteristics regarding mode effective index, propagation losses and mode confinement are very similar to the symmetric plasmonic slot waveguide composed of an symmetric and infinitely extended SiO_2 environment. The effective mode index is larger than the mode index of the radiation modes in the dielectric, therefore, the fundamental mode is bound over the entire investigated range of slot widths, similar to the case of a symmetric plasmonic slot waveguides. As a consequence, the optical leakage into the substrate at the slot waveguides used in Appendix A and B can be avoided and the optical attenuation due to leakage is reduced.

The size of the mode is deeply subwavelength, representing the most confined waveguide configuration in this thesis. Since the majority of the mode field is localized inside the slot region, the effective mode area is smallest for narrow gap widths, while the mode effective index and the optical losses increase drastically due to the increased penetration into the metal.

In the opposite limit of large slot widths, the mode effective index and the propagation losses asymptotically approach the effective index of the surface plasmon mode of a single metal–dielectric interface, with a continuous decrease of the effective mode size. For the 150 nm wide slot waveguide, which is used in Appendix B, the normalized effective mode area is $A_{eff}/A_0 \approx 0.007$. This is a size reduction by a factor of 150 compared to the diffraction limit in freely propagating light in air. It seems prudent to utilize the drastic increase of the optical density provided by the slot waveguide configuration for sensing or optoelectronic applications. For instance, by filling the slot with an electro-optic polymer material, the phase of the gap SPP can be modulated by an externally applied static electric field [19].

In this thesis, we aim to realize an ultra-compact plasmonic photodetectors, in which the slot is locally filled with semiconductor material. The dense optical field provided by the SPPs exhibits an excellent confinement in the active semiconductor core, and therefore significantly increases the free carrier concentration by photoexcitation in the semiconductor. By applying an external electrostatic field at the parallel metal plates formed by the sidewalls of the slot waveguide, the free charge carriers are efficiently collected
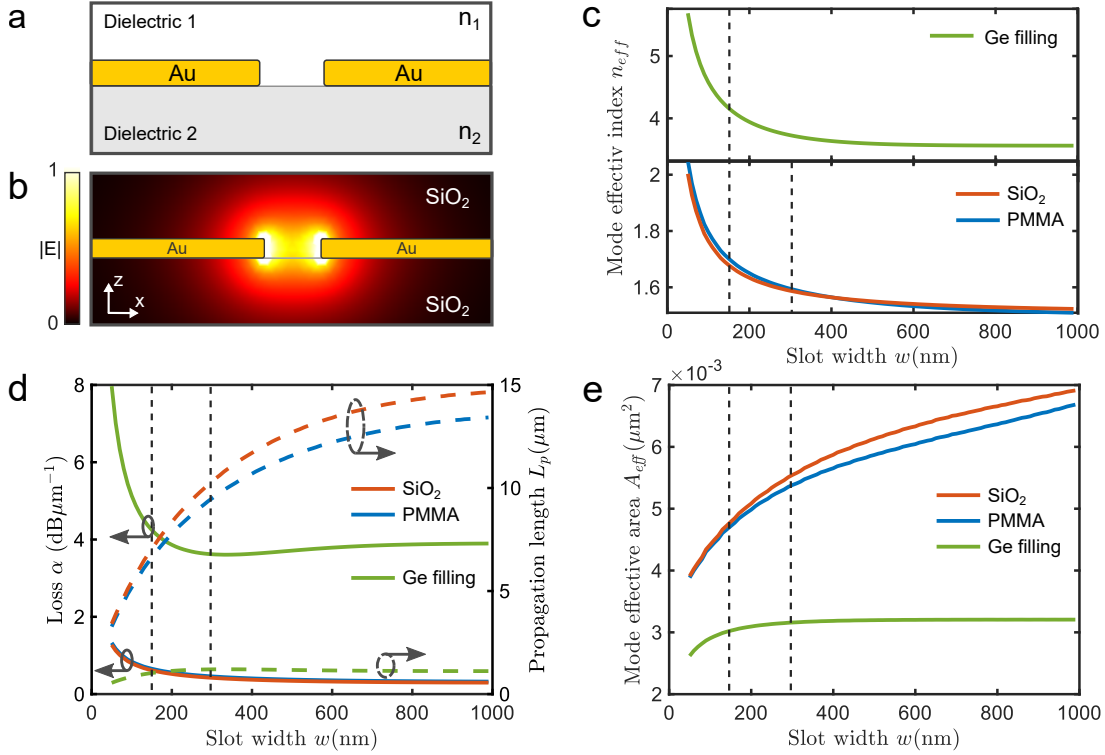
FIGURE 2.5: Plasmonic slot waveguide characteristics for different material compositions for 100 nm thick gold. **a** Cross-section of the waveguide architecture. **b** Mode profile of the fundamental mode supported by a symmetric plasmonic slot waveguide. The dashed lines in **c-e** represent the design configurations used in Appendix B ($w = 150$ nm) and Appendix A ($w = 300$ nm), respectively. Slot waveguides for various upper cladding materials (SiO$_2$, PMMA and Ge) are studied. **c** Effective mode index of the investigated configurations as a function of the slot width w. **d** Propagation loss α and propagation length L_p of the investigated configurations as a function of the slot width w. **e** Effective mode area defined by Equation 2.38 as a function of the slot width w.

(See 3.1.2 and Appendix B for more details). In this section, we consider only the optical properties of the plasmonic waveguide photodetector, in which the slot is locally filled with germanium with the complex refractive index $n_{\text{Ge}} = 4.65 - i0.298$ provided by Aspnes and Studna [20]. Since Ge exhibits a high real part of the refractive index at telecommunication wavelengths, the mode effective index is significant higher than for a PMMA filling. Furthermore, an improved localization of the mode is obtained due to the high refractive index in the slot, at the cost of immense optical losses, also contributed by larger optical absorption related to the high imaginary refractive index of the medium. This originates from the generation of free charge carriers in the semiconductor material. It is evident that the absorption of photons in the semiconductor material is favourable for the realization of semiconductor-based plasmonic photodetectors, providing the functionality of converting light into electrical energy.

2.4.2 Metal strip waveguide

Contrary to the plasmonic slot waveguide, the plasmonic metal strip waveguide essentially consists of a single rectangular slab of metal surrounded by a dielectric (Figure 2.6). In its simplest form, the surrounding dielectric is uniform and infinitely extended so that
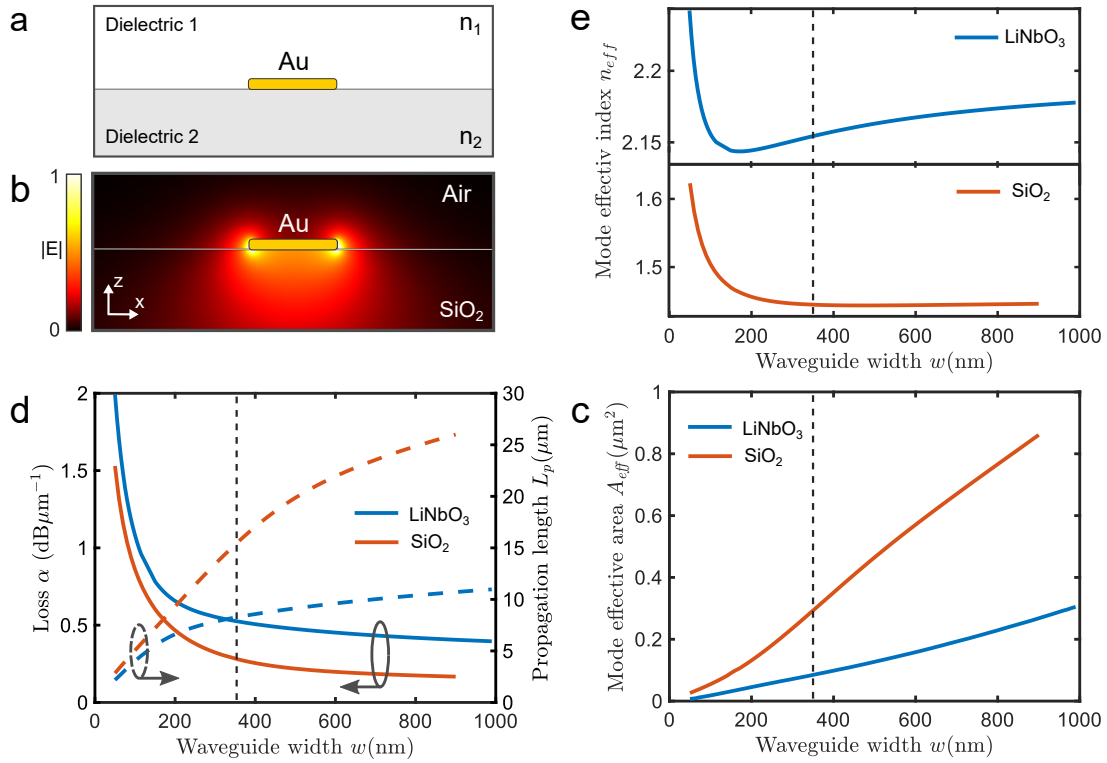
FIGURE 2.6: Plasmonic metal strip Waveguide characteristics on LN and SiO$_2$. **a** Cross-section of the waveguide architecture. **b** Mode profile of the waveguide mode supported by a 350 nm wide Au strip on SiO$_2$. Effective mode index **c**, propagation loss **d** and mode effective area **e** of the investigated configurations as a function of the strip width w. The dashed lines represent the design configurations used in Appendix C ($w = 350$ nm on LiNbO$_3$ substrate)

the metal strip is completely embedded in the homogeneous dielectric. In this symmetric environment, there are two bound modes that are supported by the structure which have opposite symmetry, the long-range SPP (LR-SPP) and short-range SPP (SR-SPP) modes, identified by their drastic difference in propagation loss and mode confinement. As the name implies, the long-range SPP exhibits very low propagation losses (Sub-dB/mm) due to a weak mode confinement.

The symmetric waveguide configuration has been used by Berini et al. [21] for electro-optic modulation of LR-SPP transmission in a several mm long gold strip waveguide buried in LiNbO$_3$. Conversely, the short-range SPP is significantly more concentrated at the metal–dielectric interface and exhibits consequently much shorter propagation distances due to the increasing ohmic losses in the metal. However, increasing the optical energy density can significantly enhance light-mater interaction inside the active material, thus enabling plasmonic devices to be much shorter due to an increased efficiency. Following this approach in this thesis, short-range SPP (SR-SPP) modes supported by a metal strip placed on a bulk LiNbO$_3$ substrate are investigated, using air ($n_1 = n_{\text{air}} = 1$) as low-index upper dielectric material. The waveguide characteristics of short-range SPP modes are studied for gold strips of different widths and supporting substrate materials, while the gold thickness is kept constant at 50 nm (Figure 2.6). For a gold strip on SiO$_2$ substrate ($n_2 = n_{\text{SiO}_2} = 1.44$), the decrease of the strip width leads to an increase of the mode confinement, accompanied by a reduction of the propagation length and a continuous increase of the effective mode index. For a strip waveguide on z-cut LiNbO$_3$

($n_2 = n_{\text{LiNbO}_3}; n_x = n_{o,\text{LiNbO}_3} = 2.21, n_z = n_{e,\text{LiNbO}_3} = 2.14$) [18], the strip width dependence shows a similar behavior, with a continuous decrease of the effective mode width for narrower waveguides, at the cost of increased optical loss. Compared to the mode confinement provided by metal strip waveguides on SiO_2, the mode is stronger confined to the Au/LiNbO$_3$ interface, due to the larger refractive index of LiNbO$_3$. Interestingly, the mode effective index exhibits a local minimum at ~ 150 nm. This can be explained by the fact that the optical mode, while being squeezed into smaller lateral sizes, is becoming more present in the upper low-index dielectric ($\epsilon_{air} = 1$), thus experiences a decrease of the mode effective index. For smaller waveguide widths, the influence of the plasmonic interaction becomes dominant, leading to a continuous increase of n_{eff} for narrower waveguides ($w < 150$). At the waveguide width of $w = 350$ nm used in Appendix C for the realization of ultra-compact electro-optic modulation, the mode area $0.12A_0$ is almost one order of magnitude smaller than the diffraction-limited area in air, and half as small as the diffraction limited area $0.5A_{0,LN}$ in lithium niobate. The enhanced light-mater interaction that comes along with smaller mode widths combined with the high integration capability led to a record-high electro-optic efficiency in the studied plasmonic lithium niobate modulator in this thesis. This is further discussed in Chapter 3 and 4.

2.4.3   Dielctric-loaded surface plasmon polariton waveguide

The majority of plasmonic waveguide configurations, such as the two waveguide designs presented above, suffer from inherently high propagation losses due to their metallic nature. The losses in the range of 0.5 dB/μm present a major hurdle in their deployment in long-range nanophotonic systems. However, there have been many studies looking for configurations that overcome the drastic optical attenuation while keeping the attractive features of tight confinement and high integration density in plasmonic systems [22–27]. These approaches all function on the same design methodology, i.e. by minimizing the presence of metal in the waveguide configuration, and by providing a symmetric dielectric environment to reduce strong fields inside the metal where ohmic loss occurs. Thereby, plasmonic waveguiding with several millimeters of propagation distance and losses of $\sim 1 - 2$ dB/cm were experimentally demonstrated [28, 29] and employed in active device platforms. In this thesis, long-range dielectric loaded surface plasmon polariton (LR-DLSPP) waveguides are investigated for the realization of low-loss plasmonic electro-optic modulation (Chapter 3.2). This waveguide configuration consists of a dielectric ridge placed on top of a thin metal film which is supported by a dielectric film on top of a low-index substrate (Figure 2.7a). Following the approach of reducing propagation losses, the metal strip must be thin (typically ~ 15 nm), but still far above the material's percolation threshold to avoid scattering. It is also kept narrow to be fully embedded into the dielectric ridge. A symmetric optical environment around the metal film, which is beneficial for reducing losses, can be ensured by using dielectrics with similar refractive indices. Alternatively, a balanced field distribution can be achieved by either varying the height of the ridge or the thickness of the dielectric film.

   Let us more precisely discuss the characteristics of this waveguide configuration, by investigating waveguides with the material composition used in this thesis at the free-space wavelength $\lambda = 1.55\mu$m. Therefore, we consider a 15 nm thin Au strip embedded into a TiO$_2$ ($n = 2.3$) ridge deposited on top of a 500 nm thick z-cut LiNbO$_3$ layer supported by a SiO$_2$ substrate. Considering an equal thicknesses of the ridge and the LN layer, the electric field is predominantly located in the dielectric region around the Au strip, but appears to be tighter confined in the TiO$_2$ ridge (Figure 2.7b) due to its slightly larger refractive index. This behaviour correlates with the higher effective mode index by
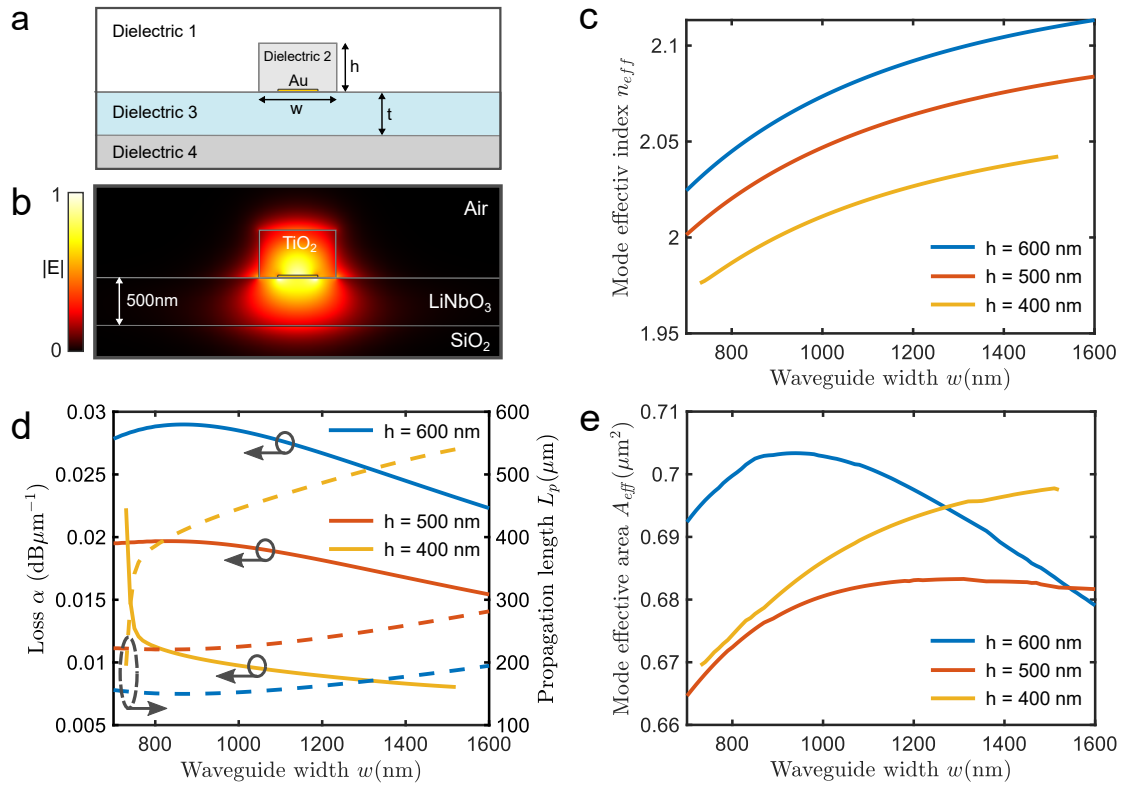
FIGURE 2.7: Long-range dielectric-loaded SPP waveguide characteristics for air (dielectric 1), TiO$_2$ (dielectric 2), 500 nm thick LiNbO$_3$ (dielectric 3) on a SiO$_2$ (dielectric4) substrate. **a** Layout of the corss-section of the waveguide structure. **b** Mode profile of the waveguide mode supported by a 800 nm wide and 500 nm thick ridge. Effective mode index **c**, propagation loss **d** and mode effective area **e** of the investigated configurations as a function of the ridge width w.

increasing the ridge thickness (Figure 2.7c), when a larger fraction of the mode is present in the TiO$_2$ ridge. When investigating the loss of such structures (Figure 2.7d), it turns out that the propagation lengths are significantly increased compared to the previously discussed waveguides and therefore provide propagation length of several hundred micrometers. Comparing the three ridge height of 400 nm, 500 nm and 600 nm, the lowest losses are observed in the waveguide with small ridge heights. By decreasing h even further, the mode becomes less confined due to mode leakage into the LN layer. This behaviour can also be observed with narrow ridges below 800 nm, when the losses increase due to mode squeezing out of the ridge region. Generally, this waveguide configuration provides relatively tight mode confinement below 1 μm^2 (Figure 2.7e). While this value is conceptionally larger than in other plasmonic waveguides, LR-DLSPP waveguides have been proven to be preferable for compact applications where low loss with high integration density is of major interest. The presence of the metal near the optical field can fully replace external control electrodes e.g. utilized for thermo- or electro-optic modulation. By directly addressing the thin Au strip with an electrical potential, optoelectronic devices can be built with extraordinary efficiency and compactness, while having reasonably low losses. This possibility is further discussed and specified in Chapter 3.2 where a plasmonic Pockels modulator based on LR-DLSPP waveguides is proposed.

2.5 Excitation of surface plasmon polaritons

After understanding the properties of surface plasmon polaritons and the variety of different waveguide geometries, the excitation techniques of generating SPPs should be discussed. As shown in Chapter 2.3, the dispersion relation of SPPs lies to the right of the light line and without overcoming the momentum mismatch between light in air and the SPP, the direct excitation via propagating light is impossible. There are two major approaches to overcome the momentum mismatch, namely by using prism coupler or optical scatterers. A prism coupler enhances the momentum of the optical wave propagating through it by the high refractive index n_p of the prism. The momentum-matching condition in the presence of a prism attached to a metal surface is $k_0 n_p \sin \theta_p = k_{spp}$ and can be fulfilled at a specific angle of incidence θ_p, by attenuated total reflection (ATR). The two widely used configurations with regard to the prism coupling technique are the Kretschmann configuration [30] and the Otto configuration [31]. Since prism coupling is not the technique used to excite SPPs in this thesis, this approach is not further discussed here. Rather we focus on the variety of optical scatterers which serve as excitation couplers for the demonstrated plasmonic devices in this thesis. In general, there are several geometries of scatterer-based couplers which capture the radiation from the free space and launch it into the plasmonic waveguide by providing the wave vector for the excitation of SPPs. Those can be categorized in three different types of scatterers [32], namely grating coupler, antenna couplers and random scatterers. While the first two scatterer types are usually designed to intentionally couple light into the desired waveguide mode, random scatterers, e.g. implemented by (nonideal) interfaces exhibiting surface roughness, can unintentionally excite plasmonic modes. Thus this mechanism is also called parasitic coupling. Considering the universal principle of reciprocity in optical systems, the inverse process leads to (radiative) losses in the plasmonic waveguide transmission. The scattering losses caused by roughness of the metal surfaces in non-ideal plasmonic waveguides, can lead to a significant underestimation of the total transmission losses in numerical calculations, where perfectly smooth surfaces are considered which inhibit radiative decay caused by scattering on roughness features.

When discussing and comparing the efficiency of the excitation of waveguide and surface plasmon modes, it is common to state the coupling efficiency (in percent or dB), which represents the fraction of power of the incident light that is coupled into the waveguide. It is therefore defined as

$$\eta = \frac{P_{WG}}{P_{inc}} \,. \tag{2.40}$$

Achieving a high coupling efficiency is one of the main goals in designing optical couplers. Therefore, lots of efforts are devoted to theoretically analyze and experimentally demonstrate coupling schemes that improve the efficiency of light coupling into various waveguide modes. This eventually minimizes the overall optical losses in integrated optical circuit elements. In addition, other relevant parameters that influence the coupler design geometry and eventually impact its practical deployment for a specific configuration are the operation wavelength, polarization sensitivity, coupler footprint and the fabrication feasibility. Considering the applicability with respect to the plasmonic excitation schemes used in the presented plasmonic devices in this thesis, we discuss in the following grating couplers and antenna couplers in more detail.

2.5.1 Grating Coupler

To gain an insight on how to design the parameters of a grating coupler, the basic condition to overcome the momentum mismatch between freely-propagating light and surface plasmons is discussed. For light coupling, the conservation of momentum dictates that the tangetial wavevector component of an incident wave must be matched with the wavevector of the waveguide mode. The required momentum can be provided by periodically arranged scatterers (ridges), which exhibit a geometrically-tunable grating vector $\mathbf{k_g} = 2\pi/\Lambda$, controlled by the grating period Λ of the arrangement of the scatterers. Then, efficient coupling through gratings is achieved by fulfilling the phase-matching condition

$$\mathbf{k}_\parallel = \mathbf{k}_{SPP} \pm m\mathbf{k}_g, \tag{2.41}$$

with the in-plane wavevector $\mathbf{k}_\parallel$ of the incident beam, and the wavevector $\mathbf{k_{SPP}}$ of the waveguide mode, with an integer number m. With the azimuthal angle ϑ being zero, Equation 2.41 becomes

$$nk_0 \sin\varphi = k_{SPP} \pm mk_g, \tag{2.42}$$

where k_0 is the free-space wavevector, φ is the polar angle of incidence and n is the refractive index of the medium. Following this condition, impinging light is scattered in various directions dependent on the diffraction order m, which provides control of the radiation being scattered into a specific propagation direction. By finding a grating geometry which fulfills Equation 2.42, grating couplers are very efficient vertical coupling solutions where incident light is redirected towards the waveguide propagation direction. As an example of finding an optimized grating design for a specific waveguide configuration, we calculate the phase-matching condition for a plasmonic waveguide composed of an infinitely wide Au strip with a thickness of 50 nm placed on a z-cut LiNbO$_3$ substrate. Considering the first order of diffraction ($m = +1$) and the calculated mode effective index of ($n_{eff} = 2.19$) for light illumination under normal incidence ($\varphi = 0°$) through air ($n = 1$) with the wavelength of $\lambda_0 = 1.55\mu$m, the phase-matching condition becomes

$$0 = k_{SPP} \pm k_g \rightarrow \Lambda = \frac{\lambda_0}{\text{Re}(n_{eff})} \approx 0.7\mu\text{m}. \tag{2.43}$$

This implies that the grating period for efficient excitation of the corresponding SPP mode should be $\Lambda \sim 700$ nm.

The topology optimization of grating couplers can further be extended by introducing the filling factor l/Λ defined as the ratio between the grating line element width l and the periodicity Λ. Typical filling factors are around 0.5, which is an appropriate initial value for further numerical design optimization. The results of the optimization problem of finding a grating design for an efficient and compact grating design feeding the considered plasmonic waveguide configuration mentioned above (50-nm thick Au strip on a z-cut LiNbO$_3$ substrate) is shown in Figure 2.8. A diffraction limited (NA= 0.9) Gaussian beam with $\lambda_0 = 1550$ nm is centrally and normally ($\varphi = 0$) illuminating an all-metallic grating coupler consisting of three semi-infinite wide gold wires. By considering the grating design used in Appendix C, which represents the simplest design fulfilling the phase-matching condition 2.43 (with periodicity of 700 nm and a filling factor of 0.5) a coupling efficiency of approximately 8% (-10 dB) is achieved. This value is very close to the maximum coupling efficiency, provided by the uniform metallic grating (Figure 2.8b). By using more complex grating designs, e.g. consisting of non-uniform grating elements or staircase-shaped gratings, significantly higher coupling efficiencies have been demonstrated [33–36]. However, these grating geometries usually require much more complex fabrication processes.
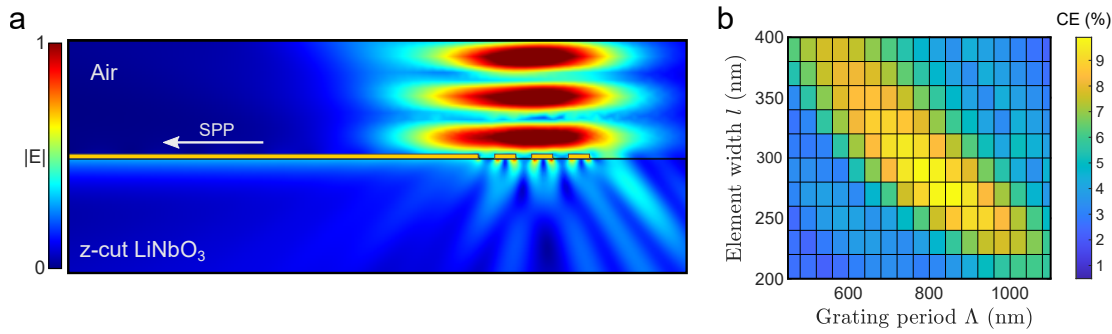
FIGURE 2.8: Plasmonic grating coupler for a metal strip waveguide. The grating is designed for normal incidence operation for a diffraction limited (NA=0.9) Gaussian beam at 1550 nm. **a** Electric field distribution simulated for the grating design used in Appendix C. The confined electric field at the Au/LiNbO$_3$ interface reveals the excitation of surface plasmon polaritons (SPPs). **b** Simulated coupling efficiency for varying grating line width l and grating periodicity Λ.

2.5.2 Optical antennas

Although there is a significant difference in the plasmonic excitation strategy used in Appendix A and Appendix B, they both rely on infrared antennas, whose fundamental operation principle is discussed in the following.

The objective of a optical (infrared) antenna is equivalent to that of classical antennas for microwave and radiowave applications, namely providing efficient energy transfer between a localized source or receiver and the free-radiation field [37]. Based on the same principles of electromagnetic theory for microwave antennas, optical antennas emit electromagnetic waves due to oscillating electric charges in the metallic antenna structure. Hereby, the characteristic radiation pattern depends on the antenna design and the operation frequency. Besides, a receiving antenna operates in the inverse sequence, by collecting incident electromagnetic energy and converting it into oscillating charges. For an antenna to emit efficiently, it should be operated at the electromagnetic resonance, which implies that its characteristic dimensions are in the order of the wavelength of the incident wave. For radio or microwave communications, the typical size of antennas ranges from tens of metres to a few millimetres. However, optical antennas operated at much smaller (optical) wavelengths require much more demanding fabrication accuracy down to the submicron or nanometer scales. Since nanoscale fabrication became increasingly accessible, antennas operated at the visible and infrared region of the electromagnetic spectrum are subject of a growing number of recent scientific studies and form the basis of many novel nanophotonic applications [37]. The majority of antennas operated in the optical and infrared are based on metal nanostructures, whose optical response is attributed to the excitation of localized surface plasmons (LSP). The excited charge oscillations in the nanoantenna can couple to a mode of an adjacent waveguide positioned in the near-field of the plasmonic antenna. The excited LSPs provides an enlarged local density of optical states (LDOS) and thereby bridges the wave vector mismatch between plasmonic mode and far-field radiation. For several reasons, the captured electromagnetic radiation cannot be fully directed into the waveguide. Firstly, as for plasmonic waveguides, charge oscillations in the nanoantenna exhibit large ohmic losses at optical frequencies. The corresponding dissipated power can't contribute to the energy transfer between free radiation and the plasmonic waveguide mode. Secondly, due to re-radiation of the captured electromagnetic energy back into free space, there is a theoretical limit of
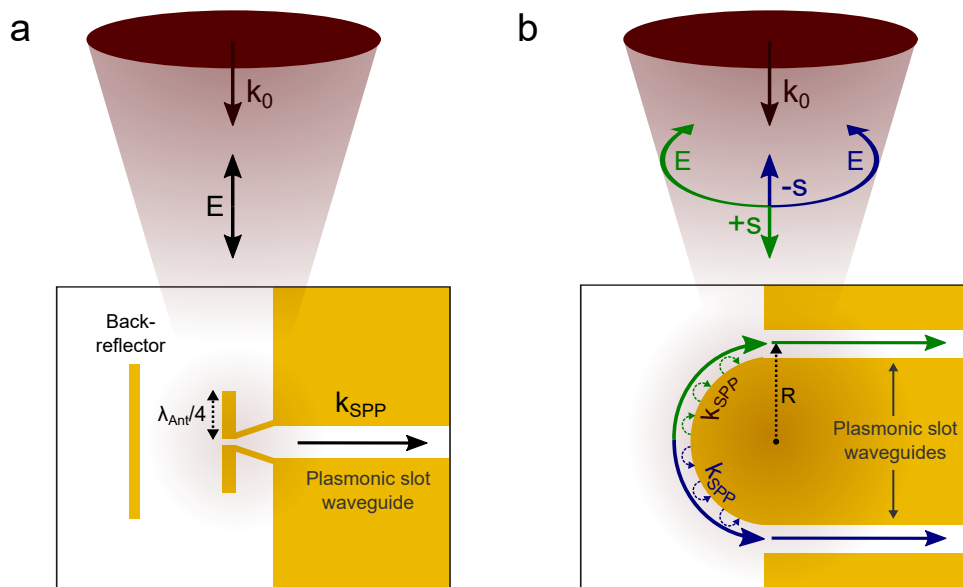
FIGURE 2.9: Plasmonic antenna structures for light coupling into plasmonic slot waveguides. **a** Plasmonic dipole antenna with back-reflector for directional and efficient coupling of an incident beam with the electric field linearly polarized along the antenna axis. **b** Curved metal antenna for helicity-controlled unidirectional coupling into a plasmonic slot waveguides. The handedness of circular polarized light determines the dominating excitation direction. For left circular polarized light (blue), the lower plasmonic slot waveguide is excited, while for a right circular polarized light, the opposite waveguide is excited.

50% of the power that can be transferred by a plasmonic antenna embedded in a symmetric dielectric environment [38]. Nevertheless, the achieved coupling efficiencies (highest experimentally demonstrated coupling efficiency is ~ 26 % [39]) are fairly close to this theoretical limit. Additionally, the small footprint makes plasmonic nanoantennas to a compact system for the excitation of SPPs.

There is a multitude of plasmonic nanoantennas geometries that have been reported in the literature. Among them, dipole antennas exhibit a comparably simple architecture. This antenna formed by two metal nanorods with the length L_{ant} separated by a gap g_{ant} between those. The geometry for an ideal microwave dipole antenna is dictated by its resonance condition, which implies that the length of half-wave dipole antenna is equal to one-half of the wavelength of the incident electromagnetic wave (with each antenna arm having the length of $\lambda_0/4$). However, this simple relationship fails for optical antennas: contrary to incident electromagnetic microwave which are perfectly reflected from the metal, optical radiation penetrates into the metal and introduces plasmonic oscillations along its surface. Therefore, the optimum antenna length is no longer governed by the incident radiation wavelength, but by the shorter effective wavelength $\lambda_{ant} < \lambda_0$ which depends on the antenna's material properties [40]. The optical dipole antennas for infrared radiation ($\lambda_0 = 1550$ nm) used in this thesis rely on the numerical antenna design optimizations presented in [39] and [13], exhibiting an antenna arm length of $L_{ant} = 380$ nm. The subwavelength gap ($g_{ant} = 80$ nm) between the antenna arms is a region of high local field intensity when the incoming light is polarized along the length of the antenna. The gap is connected to an tapered transmission line, enabling seamless energy transfer between the nanoantenna and the plasmonic slot waveguide. An additional metal reflector is positioned next to the antenna such that the waves emitted from the antenna
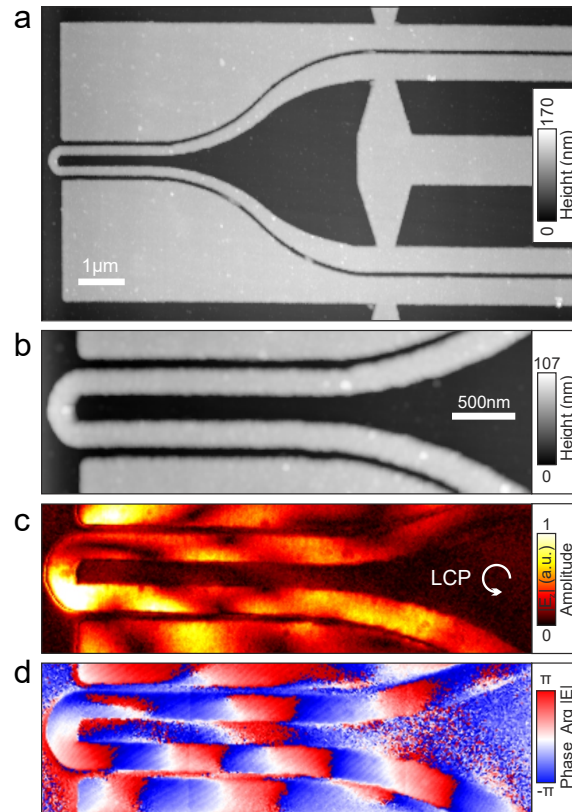
FIGURE 2.10: Near-field measurements of the chiral coupler utilized for spin-selevtive routing in the plasmonic nanocircuit. **a,b** AFM measurements of the investigated structure. The near-field amplitude $|E|$ and phase Arg $|E|$ are imagiged in **c** and **d**, respectively. SNOM measurements were conducted by Mike Prämassing in the group of Prof. Dr. Stefan Linden, University of Bonn, Germany.

return back in phase, thus coherently adding to the energy transfer between transmitting/receiving antenna and the plasmonic slot waveguide. Due to the small footprint of the coupling antenna used in Appendix A, two parallel antenna elements are deployed to excite an array of plasmonic waveguides by one diffraction-limited incident beam. This allows the realization of branchless Mach-Zehnder interferometers, which exclusively consists of the coupling antennas and the interferometer arms, thus providing a small-footprint solution for sensing or electro-optic applications.

Another antenna geometry deployed in this thesis is depicted in Figure 2.9b. This antenna configuration allows helicity-controlled unidirectional coupling to a slot SPP mode. The concept is based on the transfer of the angular momentum provided from an incident beam to a guided mode propagating along a sharply curved trajectory. This phenomenon, also known as photonic spin Hall effect, has recently attracted considerable attention due to its potential applications in spin-selective light manipulation [41–47].

In this thesis a subwavelength curved antenna is used as a helicity-sensitive coupler element. The curved gold element depicted in 2.9b supports two counter-propagating plasmonic edge modes, which posses the opposite twisted electric-field evolution of the near-field at the curved element. The inherent transverse spin vector is pointing in opposite directions for the trajectories of each elemental portion of the curved element. Due to the preserved spin-momentum locking of the evanescent (surface plasmon) waves (See Chapter 2.3), incident radiation with particular spin-state ($s = \pm 1$) can couple to the

transverse spin of the corresponding edge modes, and unidirectional feed the seamlessly integrated plasmonic slot waveguides. Generally, efficient unidirectional coupling arises when the condition

$$R = \lambda_{SPP}/2\pi \tag{2.44}$$

is fulfilled, which dictates the dimension of the radius R of the curved element [47].

In Appendix B, this excitation scheme is used for the spin-dependent unidirectional excitation and subsequent optoelectronic detection of plasmonic slot waveguide modes in a single plasmonic circuit. The coupling efficiency of a semi-ring antenna is experimentally measured by optical far-field waveguide excitation and subsequent collection of the optical signal emitted from the terminating plasmonic dipole antennas. A passive plasmonic circuit without integrated Au-Ge-Au photodetecors is investigated, where the slot waveguides are fully covered by a 300 nm thick PMMA layer over their entire waveguide length, to reduce mode leakage into the underlying SiO_2 substrate. The semi-ring exhibits a coupling efficiency of $(9 \pm 1)\%$ which is slightly lower than the calculated coupling efficiency of 12.1% using FDTD.

Further experimental studies of the passive device has been performed by AFM-based phase-resolved scattering-type scanning near-field optical microscopy (SNOM) in collaboration with the group of Prof. Dr. Stefan Linden, University of Bonn, Germany. Details on the experimental method can be found in [48–51].

The experimental near-field analysis was conducted for a quantitative investigation of the optical near-field evolution in the chiral coupler by using a scanning near-field optical microscope from NeaSpec operated in a transmission configuration (Figure 2.10). Therefore, the same sample was characterized after removing the PMMA cladding by soaking it into acetone. This is necessary for the optical near-field above the excited gold nanostructures to be able to couple to the AFM tip which serves as a near-field probe. This forms a scattering signal which contains information on the amplitude and phase of the local out-of-plane component of the optical near-field at the probing position of the nanostructure. For the excitation of SPPs, a focused laser beam with the wavelength of $\lambda = 1520$ nm is transmitted through the substrate and fixed onto the semi-ring coupler during the measurement. Left-handed and right-handed circularly polarized light (LCP and RCP, respectively) is generated by placing a monochomatic circualar polarizer into the beam path before the beam is focused onto the antenna coupler from the substrate side by a parabolic mirror.

Atomic force microscopy (AFM) images of the investigated structure are depicted in Figure 2.10a-b. Note that the apparent lateral dimensions are strongly distorted by tip convolution effects, leading to an overestimation of the Au feature sizes and consequently to an underestimation of the waveguide slot width. The amplitude $|E|$ and phase Arg $|E|$ of the measured near-field distribution under excitation with LCP light, reveals unidirectional excitation in the lower waveguide branch. The predominant presence of local fields at the waveguide and the characteristic asymmetry of the waveguide mode with a phase jump of π across the slot indicate the presence of the bound plasmonic slot waveguide mode (2.10c-d). This observation is much less pronounced in the opposite waveguide. There, the field amplitudes of the waveguide mode are much smaller, but still existent which may result from direct SPP excitation e.g. due to scattering at surface roughness features.

The spin-hall effect induced by the chiral coupler antenna in this plasmonic circuit can be investigated more clearly by studying the near-field evolution for three different polarization states of the incident beam (Figure 2.11). By comparing the measurements with circularly polarized excitaion with opposite handedness (2.11a and c), opposite waveguide excitation is clearly evident. The coupler exhibits a characteristic positive phase
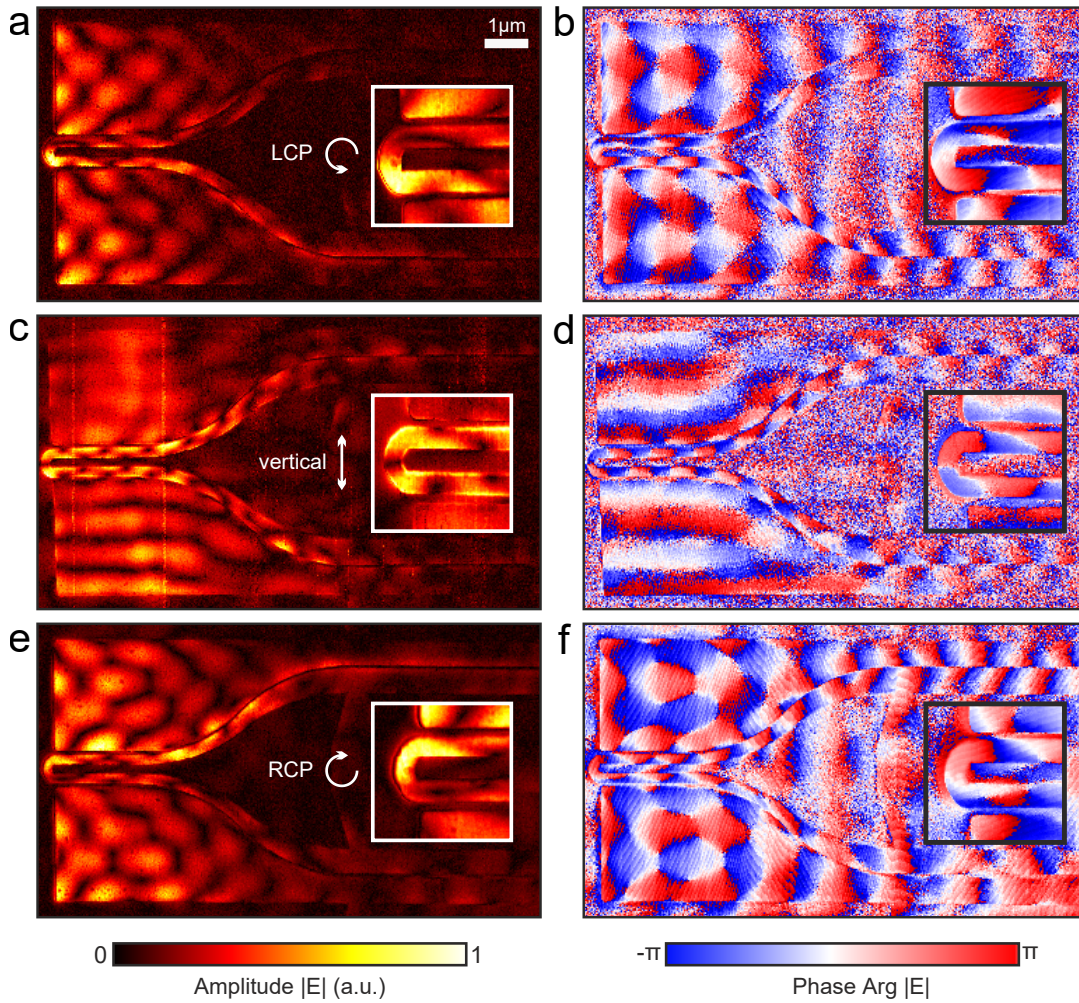
FIGURE 2.11: Large scale SNOM measurements of spin-selective routing in a plasmonic circuit. The excitation beam with the wavelength of $\lambda = 1520$ nm is positioned at the chiral coupler for LCP (**a,b**), horizontally-linear (**c,d**) and RCP (**e,f**) light. The insets depict high resolution s-SNOM images of the chiral coupler antenna. SNOM measurements were conducted by Mike Prämassing in the group of Prof. Dr. Stefan Linden, University of Bonn, Germany.

gradient around the half ring during mode propagation towards the lower waveguide for LCP and upper waveguide for RCP light, respectively. Furthermore, the field is locally enhancement at the corresponding waveguide edge. In contrast, linear polarization shows no directionality due to a symmetric optical coupling process, resulting from the superposition of LCP and RCP light of equal amplitude and phase (2.11b). Additionally to the excitation of the slot waveguide mode, freely propagating SPPs are excited at the illuminated Au edges at all polarization states, since the excitation spot is large enough to excite SPPs at the left and top/bottom edge of the gold layer. For LCP and RCP light, the interference of the SPPs launched from all three edges leads to a 2D standing wave pattern on top of the gold film, which can be observed in the near-field images of the unstructured gold area in Figure (2.11a and b). This unintentional excitation of SPPs could be suppressed by extending the gold film around the chiral coupler antenna.

In Appendix B, the straight part at the end of the two plasmonic slot waveguides is locally filled with germanium for on-chip photodetection of the investigated spin-selective unidirectional excitation.

Chapter 3

Optoelectronic phenomena and devices

In this chapter, we embark the exploration and classification of various optoelectronic phenomena and integrated devices employing those. Starting from the semiconductor photodetector which converts an optical signal into an electrical signal by utilizing the photoelectric effect, the particular benefits associated with plasmonic photodetection systems are described. As the counterpart of electrical detection, we continue with the description of the electro-optic (Pockels) effect, utilized to electrically modulate optical signals. The non-centrosymmetric materials that exhibit this effect are introduced and compared. Eventually, the design concepts and operating principles of various modulator configurations, distinguished essentially by the geometry of the underlying system, are outlined. Hereby, we introduce performance metrices for a reasonable comparison of optoelectronic device performances.

3.1 Semiconductor photodetectors

Semicondoctor photodetectors, commonly referred to as photodiodes, are currently the dominating types of photodetectors utilized in optical communication systems. Those devices convert light signals into electrical signals, which can then be further processed in the electrical domain. The conversion process can be divided into three major steps:

 i. Light is absorbed in the semiconductor material and photoinduced free charge carriers (electron-hole pairs), also called hot carriers, are generated. This phenomenon is referred to as photoelectric effect.

 ii. The free charge carriers are transported through the semiconductor material to the electrodes. This relates to the carrier lifetime and the distance the carriers have to travel until they reach the electrodes. Generally, the carrier lifetime is limited in a semiconductor due to the recombination process of electron-hole pairs.

 iii. A photocurrent is formed by extracting the generated carriers at the device electrode contacts connected to a resistive load.

Each individual step is relevant and has a significant impact on the overall device performance. It is of major importance to optimize the device parameters for a maximum yield of harvested photoinduced carriers. For instance, the choice of the used semiconductor material or the doping concentration are significantly affecting each sub-process, therefore determining the overall device performance. In the following, the process of photoinduced carrier generation for various semiconductor materials is described and compared. Finally, the optical design considerations are discussed, hereby primarily focusing on the strategy of utilizing the metal in the photodetector for both, strong light

a

b
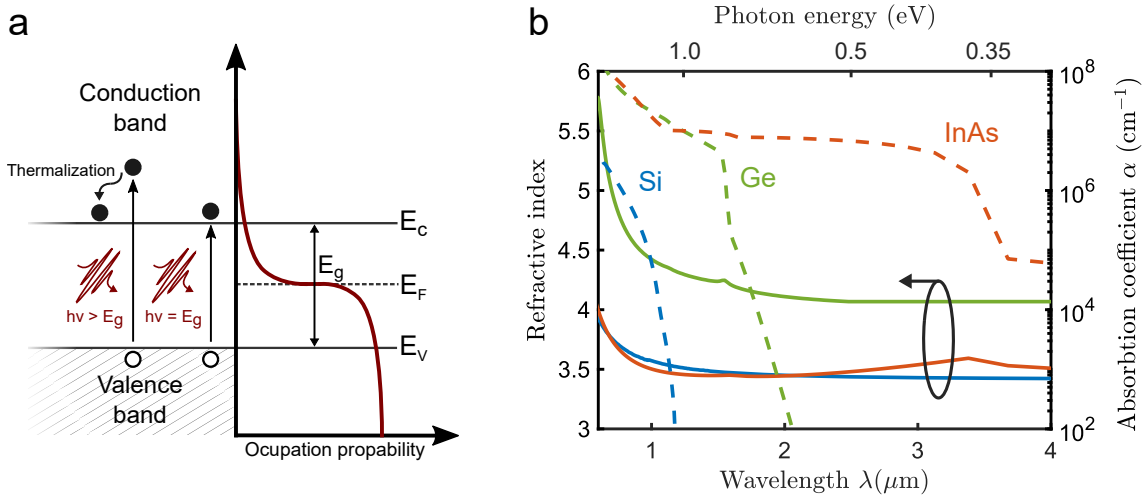
FIGURE 3.1: Photoelectric effect in semiconductors. **a** Electron-hole pair creation by optical absorption. Photons of energy equal to and greater than the band gap cause the excitation of free charge carriers. Higher energy electrons thermalize to the band edges. The initial probability of occupying the vacant energy levels is governed by the Fermi-Dirac distribution funtion. **b** Absorption coefficient of crystalline silicon, germanium, and indium ardsenide taken from [52–54]. Silicon and germanium as indirect semiconductors, have a steeper increase of the absorption coefficient at higher photon energies than their bandgap energies, compared to the direct semiconductor indium arsenide.

concentration into the active material and for applying an external electric field to efficiently extract photoinduced free-carriers.

3.1.1 Photoelectric effect in semiconductors

Bulk solid materials have a continuous range of allowed electron states that are called energy bands. Since electrons are Fermions, they obey the Pauli exclusion principle which states that each energy level can only be occupied by a maximum of two electrons of opposite spin. Accordingly, the occupation of energy levels by electrons that are filling those bands follow the Fermi-Dirac distribution

$$f(E) = \left(1 + e^{(E-E_F)/k_B T}\right)^{-1} , \tag{3.1}$$

where f is the probability that the energy level E is occupied, E_F is the Fermi level, defined by the energy level with 50% chance of being occupies at finite temperatur T, and k_B is the Boltzmann constant. The position of E_F defines the electrical properties of a solid. For insulators, E_F is between the highest occupied band (valence band) and the band with the next lowest energy level (conduction band). The band gap between the valance band and the conduction band is in this case much greater than $k_B T$, such that the occupation probability of the conduction band is nearly zero. In metals, E_F falls within an energy band, providing the availability of vacant states close to the highest occupied states, meaning the material is highly conductive. Semiconductors, on the other hand, have a small band gap E_g that allows electrons in the valence band to move into the conduction band given a certain amount of energy (Figure 3.1a). Apart from the thermal excitation caused by the tail of the Fermi distribution function which is occupying states above the Fermi level, the energy can also be provided by a photon with the energy $E_P \geq E_g$. The photon then

provides enough energy to excite an electron from the valence band to the conduction band, leaving an electron vacancy (hole), itself capable of carrying current, behind.

In an n-type semiconductor, electrons are the majority carriers, while in p-type the current is carried predominantly by the positively charged holes, considered as quasi-particles representing electron vacancies in the valance band.

A band gap is called to be direct if there is no additional momentum required for this transition process to happen. As such, the maximum energy level of the valence band must align at the same momentum as the minimum energy level of the conduction band. In an indirect band gap semiconductor, the maximum energy of the valence band occurs at a different value of momentum than the minimum in its conduction band, thus requiring additional momentum from lattice vibrations (phonon) for an electron transition. This multiparticle interaction is improbable, causing a lower recombination efficiency in an indirect band gap material than in direct bandgap semiconductors. It is evident that the more efficient and faster absorption in direct bandgap semiconductors is more favorable for optoelectronic application.

While the photogenerated free charge carriers may recombine and reemit light or couple energy to phonon modes, they can also be collected by applying an external electric field as measurable photocurrent in an external circuit. The generated photocurrent depends of the number of absorbed photons which have generated free carriers. The efficiency of this extraction depends on the strength of the external electric field, the mobility of the free carriers and the carrier lifetime which is defined as the average time it takes for a carrier to recombine. Furthermore, each semiconductor material has a specific band gap, which determines the operating wavelength range suitable for a specific applications.

Considering a light beam with a particular wavelength traveling through an semiconductor, its intensity decreases according to Beer-Lambert's law

$$I(x) = I_0 \cdot e^{-\alpha x}, \tag{3.2}$$

with the light intensity $I(x)$ after penetrating the distance x into the material, the initial light intensity I_0 and the absorption coefficient α. Studying the absorption coefficient for various commonly used semiconductors at ≈ 300 K as a function of the vacuum wavelength of light, reveals its dependence on the photon energy (Figure 3.1b). Below a certain cutoff wavelength (meaning also at higher energy of photons), the absorption increases significantly due to the photon absorption associated to the generation of electron-hole pairs. Comparing the commonly used semiconductors, silicon has a band gap energy of 1.12 eV corresponding to an absorption cutoff wavelength of 1100 nm, while germanium has a much smaller bandgap of 0.66 eV. This makes germanium more suitable for near-infrared optoelectronic application as targeted in this thesis. Apart from elemental semiconductors (group IV of the periodic table), the properties of compound semiconductors can be engineered by alloying, e.g. IV-IV (SiC, SiGe), III-V (GaAs, InAs,InP, etc.) and II-VI (CdSe, ZnSe, etc.). Photodetectors based on narrow bandgap compound semiconductors (i.e. InAs with a bandgap energy of 0.36 eV) allow a much wider wavelength range of operation in the far-infrared. Table 3.1 summarizes material properties of some commonly used semiconductors.

Besides having a semiconductor matching the operation wavelength, another indispensable factor is a high carrier mobility in the semiconductor. Higher charge mobility leads to shorter charge transit times through the device and a decrease of the probability of charge recombination. For high-speed applications, a fast and efficient carrier extraction is important, which can be achieved by increasing the charge mobility and/or by decreasing the electron transit length through the device. The latter approach stimulates

TABLE 3.1: Properties of bulk semiconductor materials at room temperature. [20]

	Si	Ge	GaAs	InAs
Electron mobility $(\text{cm}^2\text{V}^{-1}\text{s}^{-1})$	1600	3900	9200	40000
Hole mobility $(\text{cm}^2\text{V}^{-1}\text{s}^{-1})$	430	1900	400	500
Bandgap (eV)	1.12	0.66	1.424	0.36

the current optoelectronic miniaturization trend. Reducing the size of the active area, which in addition reduces the photodiode's capacitance, enables high-speed detection applications. In particular, plasmonic photodetectors with the capability of reducing the active area to subwavelength sizes, can meet future requirements for efficient photodetection at operation bandwidths beyond 100 GHz [55].

3.1.2 Plasmonic semiconductor photodetectors

In this section, we classify semiconductor-based photodetectors by their mechanism of detection. We exclude in this description hot carrier-based detectors [56–59] that exploit metallic absorption to achieve a hot carrier current upon photoexcitation in a metal. On this level, we can more finely distinguish between the photoconductors and photovoltaic photodetectors (such as p-n or p-i-n detectors or Schottky detectors) (Figure 3.2).

The photoconductor detector consists of a semiconductor material between two non-rectifying ohmic contacts where current can pass through equally in both ways. Under illumination, the absorption in the semiconductor creates free carriers, which reduce the electrical resistance across the metal electrodes. This change of the conductivity of the semiconductor is measured in an external circuit, providing an electrical signal proportional the absorbed radiation. For measuring the change in conductivity, an electric field is introduced by applying a bias voltage between the electrodes. Without illumination, the majority carriers in the semiconuctor travel towards the electrode, which results in a bias current I_{dark} flowing through the semiconductor layer. Typically, this dark current in photoconductor detectors is high due to the absence of a depletion region. Under illumination, the semiconductor material produces photogenerated charges, when $E_{\text{P}} > E_{\text{g}}$. Those are extracted by the externally applied electric field, leading to a photocurrent I_{ph} which is added to the dark current I_{dark} by the photoinduced increase of the conductivity in the semiconductor.

A PIN detector, on the other hand, is formed by a sandwich of three semiconductor layers, each with different band structure modified by adding impurities (doping) to a base material. The types of dopant of the semiconductor layers are arranged to have an undoped (intrinsic) semiconductor sandwiched by an n-type (doped with acceptor atoms donating electrons) and p-type semiconductor (doped with acceptor atoms donating holes). The bend in the conduction band and the gradient in the Fermi energy, leads to an intrinsic region without free carriers. Thus, the device is exhibiting high resistance, leading to a desirably low dark current. Under illumination, the photoinduced free carriers are pulled in opposite directions due the intrinsic voltage difference between the doped semiconductors. The carriers that reach the contacts at the doped semiconductors, are measured as a photocurrent I_{ph}.

Depending on the energy difference between the work function (difference between Fermi energy and vacuum level) of the metal and semiconductor, a Schottky barrier is formed by a rectifying junction of a semiconductor and a metal if the Fermi energy of
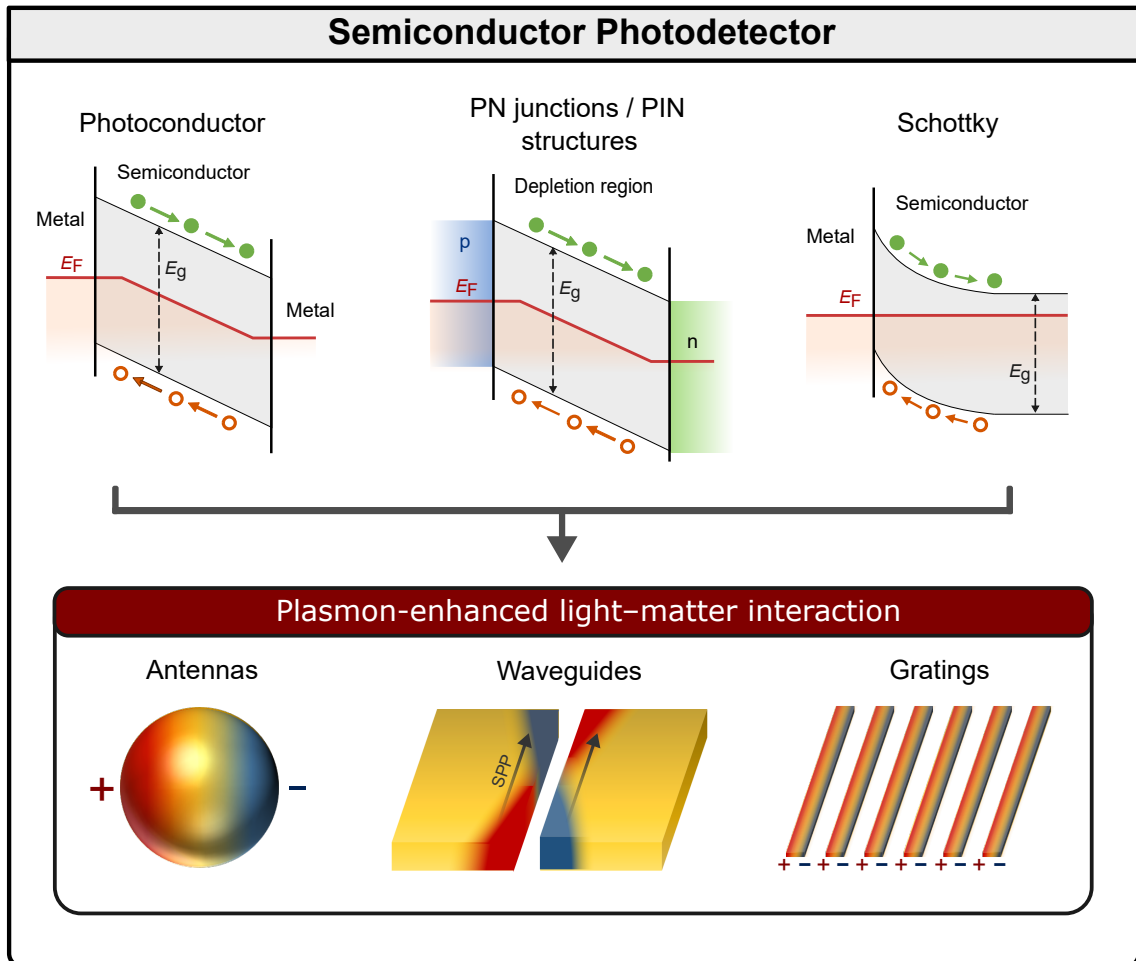
FIGURE 3.2: Types of plasmonic integrated photodetectors. Commonly used semiconductor photodetector geometries are photoconductors, p-n or p-i-n junctions and Schottky diodes which works on the general principle of the creation of electron-hole pairs due to the photoelectric interaction of incoming photons in a semiconductor. Each device architecture can be plasmonically enhanced, by utilizing strong local fields in plasmonic nanoantennas, waveguides or gratings. Metallic structures embedded in the semiconductor enabling enhanced light-semiconductor interactions can be simultaneously used as low resistive contacts for the collection and transport of photogenerated charges.

the metal is between the conduction and valence band edge of the semiconductor. A resulting charge transfer at the interface between the metal and the semiconductor creates a depletion region of mobile carriers. In equilibrium, the intrinsic electric field at the metal-semiconductor junction is comparable to that formed in a p-n or p-i-n junction. Under illumination, free electron hole pairs generated in or near the depletion region contribute to a photocurrent across the contacts.

With the broad variety of photodetectors, it is important to define common device performance metrices used to characterize and evaluate the effectiveness and quality of photodetectors. One of the most important figures of merits for optical detection is the quantum efficiency, defined by the number of signal electrons created per photon. To distinguish between the number of photons illuminating the device and the photons interacting with the active material, we formulate the internal and the external quantum efficiency. The internal quantum efficiency (IQE) includes the fraction of photons that are absorbed in the semiconductor material, but excludes any injection loss of the incident radiation such as light reflection at the semiconductor interface or other external parasitic losses (e.g. plasmonic losses). Then we can define the IQE as

$$\eta_{int} = \frac{I_{ph}}{e\phi_{abs}} = \frac{I_{ph}}{e} \left(\frac{hc}{\lambda P_{opt}} \right) , \tag{3.3}$$

where I_{ph} is the photocurrent generated from the photon flux ϕ_{abs} which is absorbed by the active medium, directly related to the absorbed optical power P_{opt}. Note that the internal quantum efficiency for most semiconductor photodetectors do not reach the theoretical optimum due to the recombination process of electron-hole pairs and thermal energy dissipation.

Besides the IQE, the external quantum efficiency (EQE) is the other fundamental parameter which includes the effect of parasitic optical losses and is defined by

$$\eta_{ext} = \eta_{int}\eta_c = \eta_{int} \left(\frac{P_{opt}}{P_{inc}} \right) = R \left(\frac{hc}{e} \right) , \tag{3.4}$$

with the coupling efficiency η_c, which accounts for the fraction of optical power that interact with the active medium in relation to the total incident power P_{inc}.

The responsivity R is another often referred parameter which is closely related to the EQE according to Equation 3.4, and is expressed in Amperes per Watt. Note that the definition can be easily expanded by including the wavelength dependence. Broadband detectors require a flat responsivity over a large spectral range, while single wavelength detectors call for a sharp and spectrally narrow response. Generally, the external quantum efficiency and the responsivity can be maximized by engineering the device architecture (i.e. by applying anti-reflection coatings, etc.) to increase the amount of optical power absorbed in the active medium. For plasmonic structures, the parasitic losses also include the ohmic loss, since the attenuated optical energy does not contribute to the generation of electron-hole pairs in the semiconductor.

As another crucial figure of merit for photodetectors, the response speed indicates how fast a device responds to a varying optical signal. More precisely, it represents the time of the electrical signal to go from 10% to 90% of the final response output, initiated by an instantaneous change of absorbed optical intensity. In the frequency domain, the detection speed is quantified by the response bandwidth, which is stating the frequency at which the responsivity is reduced by 3 dB. While moderate speeds ($\sim$ kHz) are acceptable for sensing or imaging applications, fast operation speeds (up to tens of GHz) become indispensable for state of the art telecommunication systems which rely on ultra-fast detectors with high responsivity. As mentioned in the previous Chapter 3.1.1, an

increase of the charge mobility and the reduction in device dimensions can enable ultra-fast detector operation by shortening the charge transit time and decreasing the device capacitance. In case the semiconductor layer is reduced to only a few tenths of nm, fast carrier transport is expected due to near-ballistic transport of the photogenerated carriers, with transit lengths close to its mean free-path length. Following this approach, operation speeds up to 100 GHz have been demonstrated in [55, 60, 61].

The performance of photodetectors can be plasmonically enhanced by three different approaches, namely by integrating metal nanoparticles, plasmonic waveguides or gratings into the detector device [62]. The plasmonic nanostructures utilize the plasmonic field confinement for enhanced light-matter interactions. Eventually, the device performance can be improved in many respects. Since metallic structures are naturally included in plasmonic devices, the metal elements can be utilized simultaneously for increasing the detector responsivity and for driving the photodetector device. Thus, this approach provides convincing miniaturization capability.

An example for utilizing metal nanoparticles for enhanced detection performance is demonstrated in [63], where the detection in a graphene-based p–n junction is plasmonically enhanced by Au nanodisk antennas. The optical field is concentrated in the area of a p–n junction by the local field enhancement around the resonant Au nanostructures, leading to a 20-fold increase in the photovoltaic response. By further exploring polarization-dependent nanoantennas, the generated photoresponse can be engineered to be sensitive to specific polarization states, thus allowing ultra-compact and efficient polarimetric systems for a direct determination of the polarization state of incident radiation [64]. Other devices utilizing the local field enhancement in plasmonic nanoparticles or nanoantennas are demonstrated in [65–67].

The second strategy is represented by SPP-based field enhancement in plasmonic waveguides, which additionally allow subwavelength light guiding in nanophotonic circuity. By engineering the plasmonic waveguide in such a way that the strongest field enhancement is present at the active semiconductor region, the photoresponse can be significantly increased. A proposed waveguide configuration is based on plasmonic slot waveguides, which are utilized for chip-integrated and plasmonically-enhanced photodetection [14, 55, 68]. In this thesis, a subwavelength plasmonic slot waveguide is utilized, in which a 150 nm wide slot is locally filled with photoconductive polycrystalline germanium (Appendix B). The optical field is concentrated in the germanium between the vertical metallic sidewalls of the slot waveguide, which simultaneously act as electrodes to apply an external electric field for harvesting the photogenerated charge carriers. The great field overlap between optical and electrostatic field ensures a high carrier extraction efficiency. Although at the targeted wavelength of $\lambda_0 = 1550$ nm only a fraction of the interacting photons are absorbed in germanium (Figure 3.1.1), an IQE of 1 % could be measured. It was shown by Salamin et al. [55] in a very similar device, that the IQE can exceed 15% at an operation wavelength around 1310 nm. Furthermore, the short transit lengths of the photogenerated carriers enable high-speed operation beyond 100 GHz.

Plasmonic gratings is the third commonly used approach for implementing plasmonic-field enhancement in a photodetector. Light incident on a nano-structured metallic diffraction grating can excite surface plasmon polaritons propagating along the grating. According to Equation 2.41, the grating can be designed to concentrate and enhance the absorption at a specific wavelength. Besides the optical benefits, the electronic characteristics of the photodetectors can be improved in some respects: the metal grating, used as interdigitated metallic electrodes, increases the active area of the photodetector and therefore improves the responsivity. Studies following the approach of interdigitated metal fingers on a semiconductor can be found in [69, 70].
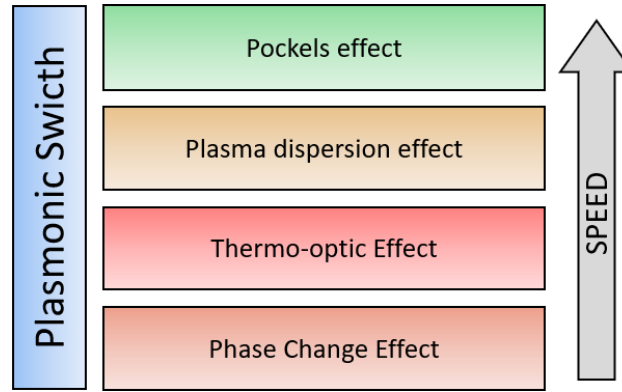
FIGURE 3.3: Commonly used effects that have been employed for the realization of plasmonic switching, sorted by their fundamental limit in the response speed. Adapted from [71]

.

In most cases, the performance metrics require trade-offs against each other. For instance, increasing the foot-print of a photodetector may increase the responsivity, but also decreases the operation speed. Similarly, the operation speed can be significantly boosted by device miniaturization i.e. provided by plasmonic devices, but at the cost of decreased responsivity due to parasitic optical losses and increased fabrication complexity.

3.2 Electro-optic modulation

Electrical manipulation of optical signals, referred to as electro-optic modulation, is indispensable for many photonic and optoelectronic applications such as optical interconnects and sensing. Depending on the manipulated optical properties of the material introducing the optical modulation, the physical effects can be categorized as electro-absorptive or electro-refractive modulation. For both types, an active material that alters its complex index of refraction needs to be introduced: absorptive modulation relies on electrical tuning of the imaginary part of the refractive index ($\Delta n''$), while the refractive modulator operates by changing the real part of the refractive index ($\Delta n'$). Although the Kramers-Kronig relations prohibit the existence of pure absorptive and refractive modulation, we distinguish in this classification between the dominant effect on the electro-optic operation in a device.

Electro-absorptive modulation relies e.g. on the Franz–Keldysh effect [72], Quantum Confined Stark Effect (QCSE) [73] or other rather novel mechanisms such as gate-induced band-filling (i.e. Pauli blocking) in graphene [74] or the electrochemical metallization effect in photonic memristors [75, 76].

In this thesis, the primary focus is set on plasmonic electro-refractive modulators which are used to implement phase modulation or intensity modulation via phase sensitive devices that rely on embedded phase shifters such as interferometers, directional couplers or resonators (See Chapter 3.2.3). There are various physical effects that can be deployed for the realization of electro-refractive modulation (Figure 3.3). The first effect historically to be implemented for electro-optic modulation in a plasmonic modulator was the thermo-optic effect introduced by resistive heating in polymer materials [77]. Here, the modification of the refractive index arises from a temperature variation in the optical material, e.g. due to the change in the material density or polarizability. The variation is characterized by the thermo-optic coefficient dn/dT, where n and T are the refractive index and the temperature in Kelvin, respectively. Light that travels through

this medium will undergo a phase shift caused by temperature gradients, thus forming the basis of various thermally-tuneable optical switches. The thermo-optic coefficients are generally small for the most applicable materials (in the order of 10^{-3} K^{-1} to 10^{-6} K^{-1}), thus devices which rely on the this effect require large footprint for their practical deployment. Research efforts have been dedicated towards the development of novel thermochromic polymers with higher thermo-optic coefficients, exhibiting an order of magnitude larger coefficients than those of inorganic materials such as SiO$_2$ ($1.1 \cdot 10^{-5}$ K^{-1}) or LiNbO$_3$ ($4 \cdot 10^{-5}$ K^{-1}) [78, 79]. Generally, this effect provides only moderate switching times of a few microseconds and relatively high power consumption due to the heat diffusion process. Nevertheless, by employing plasmonic waveguides which also act as resistive heating wires, a large overlap between the confined optical field and the thermally induced local change of the refractive index in the surrounding medium enables extraordinary efficient electro-optic switching capabilities [77, 80–86].

By changing the temperature of a material, the medium can also experience an abrupt structural phase transition leading to substantial refractive index changes. This phenomenon, referred to phase change effect, can provide enormous changes of the real and imaginary part of the refractive index in the order of unity, when a material's temperature is brought to the transition temperature T_c, where a phase change occurs. Prominent materials used for integrated plasmonic devices are germanium antimony telluride (Ge$_2$Sb$_2$Te$_5$, GST) and vanadium dioxide (VO$_2$), where switching is induced by local heating of the material, either optically or electrically [87, 88]. The high electrical energy consumption and the operation at only moderate speeds ($\sim \mu$s) in those devices are the major disadvantages that determines the suitable area of application of this effect.

Another optical phenomenon is the plasma dispersion effect [89], which is commonly used for driving active components in silicon photonic circuits. This effect is related to the density of free carriers in a semiconductor, which can be tuned by voltage-induced free carrier injection. In analogy to the well known Drude model, carrier concentrations translate to a change in refractive indices (Equation 2.22). From the first demonstration of a refractive modulator based on the plasma dispersion effect in Si embedded in a plasmonically-enhanced platform [90], several other studies achieved efficient and fast modulation [91]. The response times are only limited by the carrier diffusion times in the injection region and are in the order of nanoseconds, which complies with current switching requirements in CMOS-compatible telecommunication applications and became commercially available for optical interconnects [92]. Recently, other active materials such as indium tin oxide (ITO) have been used. Electro-absorption modulation based on ITO operated at its epsilon-near-zero (ENZ) regime, promotes strong changes in the absorption by altering the permittivity between negative and positive values. Very recently, ITO has been deployed for efficient electro-refractive modulation in photonic and plasmonically-enhanced systems [93, 94].

The effect which plays a major role in the realization of electro-optic modulation in this thesis, is the Pockels effect. It refers to the change in the birefringence of a medium which varies linearly proportional to the applied electric field and originates from the re-orientation of electric dipoles in the material. It occurs only in crystals that lack inversion symmetry, consequently, they present ferroelectric phases. Common electro-optic materials exhibiting the Pockels effect are lithium niobate, barium titanate or electric-field poled polymers or glasses. The impact of the external electric field on the change of the refractive index is governed by the nonlinearity, i.e. the nonlinear susceptibility coefficients, in the material. A detailed comparison between the applicable Pockels materials is given in Chapter 3.2.2. The Pockels effect, which is the most widely used effect in communication technologies, is particularly well suited for achieving high data rate operation due to its practically instantaneous (i.e. fs) response times. Recent breakthroughs in

plasmonic platforms operating by virtue of the Pockels effect demonstrated record high-speed (> 100 Ghz), compact and power-efficient electro-optic devices [95, 96], which are demanded in future telecommunication applications. Because of its relevance in this thesis, the following sections are dedicated to the mathematical description of the Pockels effect and its practical deployment in electro-optic devices.

3.2.1 Pockels effect

The Pockels effect is a nonlinear optical phenomenon, introduced by the nonlinear dependence of an induced polarization in a medium on the electric field. While in linear optics the material's optical responses to an electric field is described by only the first order of the Taylor-series expansion of the polarization, nonlinear effects rely on higher orders. The second- and third-order nonlinearities are the dominant phenomena in nonlinear optics, while even higher order nonlinear processes are weak and can usually be neglected. Assuming an instantaneous dielectric response, the polarization can then be expressed as

$$\mathbf{P} = \epsilon_0 \left(\chi^{(1)} \mathbf{E} + \chi^{(2)} \mathbf{E^2} + \chi^{(3)} \mathbf{E^3} + ... \right), \tag{3.5}$$

where $\chi^{(n)}$ is the nth-order susceptibility, which are tensors of rank $(n+1)$ and subject to symmetry constraints. For isotropic media ($\chi^{(2)} = 0$), third-order nonlinear processes, such as the optical Kerr effect, exist. The Pockels effect is a second order nonlinear effect, which implies that it occurs only in non-centrosymmetric media. It can be described in matrix form by

$$P_i^{nl} = \sum_{j,k} \chi_{ijk}^{(2)} E_j E_k, \tag{3.6}$$

with the electric susceptibility tensor $\chi_{ijk}^{(2)}$, having $3^3 = 27$ components, not all of which are independent of each other. Which components are related or even zero is determined by details of the crystal symmetry. The susceptibility tensor $\chi_{ijk}^{(2)}$ is connected to the electric permitivity tensor ϵ_{ij} by

$$\epsilon_{ij} = \epsilon_0 \left(1 + \chi_{ij}^{(1)} \right) + 2\chi_{ijk}^{(2)} E_k = \epsilon_{ij}^L + d_{ijk} E_k, \tag{3.7}$$

with the direction indices i, j, k, the electrostatic field E_k along direction k and the nonlinear coefficient d_{ijk}. In the literature, the electro-optic tensor r_{ijk} is commonly stated and its relationship with the susceptibility tensor is defined by

$$r_{ijk} = -\frac{\chi_{ijk}^{(2)}}{(1 + \chi_{ii}^{(2)})(1 + \chi_{jj}^{(2)})}. \tag{3.8}$$

The modification of the electric susceptibility of the medium, and consequently its refractive index, can then be described by

$$\Delta \left(\frac{1}{n_{ij}^2} \right) = \sum_k r_{ijk} E_k. \tag{3.9}$$
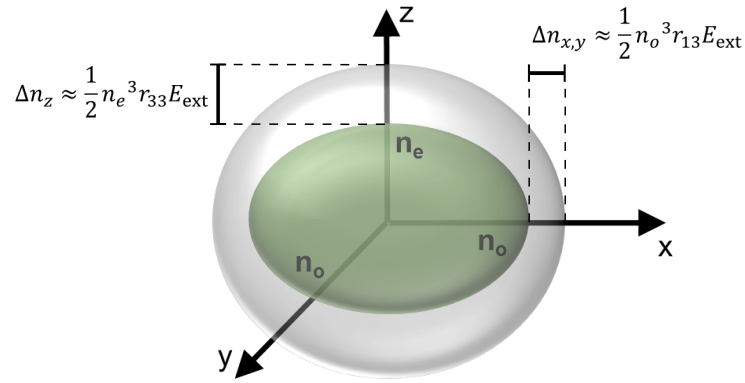
FIGURE 3.4: Refractive index ellipsoid of a negative birefringent material. Electrically-induced birefringence for a crystal with 3m-point symmetry for the case of an electric field pointing along the crystal optic axis lead to a deformation of the index ellipsoid (grey color) compared to the ellipsoid in the absence of an electric field (green color)

Following the abbreviated notation for symmetric second-order tensors [97], the number of electro-optic coefficients can be reduced according to $r_{hk} = r_{ijk}$, where

$$h = \begin{cases} 1 & \text{for } ij = 11 \\ 2 & \text{for } ij = 22 \\ 3 & \text{for } ij = 33 \\ 4 & \text{for } ij = 23,\ 32 \\ 5 & \text{for } ij = 13,\ 31 \\ 6 & \text{for } ij = 12,\ 21 \end{cases} . \tag{3.10}$$

Often, symmetry arguments can be further used to simplify the electro-optic (Pockels) tensor r_{hk} to just a few non-zero elements. For point group 3m materials (e.g. LiNbO$_3$, LiTaO$_3$) the Pockels tensor is given in the contracted Voigt notation by

$$r_{hk} = \begin{pmatrix} 0 & -r_{22} & r_{13} \\ 0 & r_{22} & r_{13} \\ 0 & 0 & r_{33} \\ 0 & r_{42} & 0 \\ r_{42} & 0 & 0 \\ -r_{22} & 0 & 0 \end{pmatrix}, \tag{3.11}$$

where the relations between the Pockels coefficients, e.g. $r_{22} = -r_{12} = -r_{61}$ and $r_{41} = r_{51}$, are exploited. The corresponding index ellipsoid in the presence of an electric field is given in cartensian coordinates by

$$\left(\frac{1}{n_x^2} - r_{22}E_y + r_{13}E_z \right) x^2 + \left(\frac{1}{n_y^2} - r_{22}E_y + r_{13}E_z \right) y^2$$
$$+ \left(\frac{1}{n_z^2} - r_{33}E_z \right) z^2 + 2r_{42}E_y yz + 2r_{42}E_x xz + 2r_{22}E_x xy = 1. \tag{3.12}$$

When the direction of the electric field aligns with the optic axis (z-axis), the index ellipsoid can be reduced to

$$\left(\frac{1}{n_x^2} - r_{22}E_y + r_{13}E_z\right) x^2 + \left(\frac{1}{n_y^2} - r_{22}E_y + r_{13}E_z\right) y^2 + \left(\frac{1}{n_z^2} - r_{33}E_z\right) z^2 = 1. \quad (3.13)$$

By assuming that the changes of the refractive index are small, a Taylor series expansion of the expressions for the refractive index in the particular axis leads to the simplified and well-known Pockels equations

$$n_x = n_y \approx n_o - \frac{1}{2}n_o^3 r_{13}E_z$$

$$(3.14)$$

$$n_z \approx n_e - \frac{1}{2}n_e^3 r_{33}E_z.$$

The corresponding index ellipsoid can then be depicted as in Figure 3.4, illustrating the orientation and relative magnitude of refractive indices with the electro-optically induced deformation of the index ellipsoid. Note that the piezoelectric contributions to the optical response of the material (due to lattice deformation introduced by the external electric field) give rise to a distinction between unclamped (stress-free) and clamped (strain-free) electro-optic tensors. Considering a dynamically changing electrostatic fields, the contribution of the piezoelectric effect to the electrically-induced birefringence is dictated by the speed of the field variation. At low modulation frequencies ($\sim$ kHz), the crystal is free to mechanically deform by the piezoelectric effect. Then the unclamped electro-optic tensor, denoted as r_{hk}^T, should be used to determine the electro-optic response of the material. At higher operation frequencies ($\sim$ GHz), above the fundamental acoustic resonances of the crystal, the material does not undergo piezoelectric responses, since lattice deformation is excluded by the inertia of the crystal. The response is then described by the clamped electro-optic tensor, denoted as r_{hk}^S. For the sake of avoiding confusion, in the following and if not otherwise stated, the electro-optic coefficients r_{hk} correlates with the strain-free coefficient r_{hk}^S.

3.2.2   Electro-optic materials

The choice of the ferroelectric material exhibiting the Pockels effect will depend strongly on the specific application and certainly no single material will provide the best performance for all modulation applications. This makes it all the more important to discuss the key properties of applicable materials and their characteristics. By far, the most common and extensively studied Pockels material is lithium niobate. Over the last three decades, this inorganic and artificially synthesized material is employed in optoelectronic devices, and to this date, optical modulators for communications rely almost exclusively on this material. While first synthesized and described by Zachariasen [98] in 1928, the crystals were too small, expensive and poor in optical quality to be practically used until 1965, when Ballman [99] reported on the melt growth of large $LiNbO_3$ crystals using the Czochralski method [100]. Unless otherwise stated, the material properties of lithium niobate presented in this thesis are taken from Weis et. al [101] and are summerized in Table 3.2. Below its high Curie temperature of 1100 °C, $LiNbO_3$ is in its ferroelectric phase, exhibiting a trigonal crystal system with the non-centrosymmetric point group symmetry 3m (Table 3.2). It is a mechanically robust and chemically stable material that possesses a Mohs hardness of 5.5. The optical band gap at room temperature varies in the literature, stating values between between 3.57 eV [103] and 4.7 eV [104]. Lithium

TABLE 3.2: Physical properties of congruently grown LN [101]. The Hexagonal unit cell of the LN crystal is adapted from [102].

Crystal structure	Property	Value
	Crystal structure	Trigonal
	Point group	3m
	Space group	R3c
	Melting point [$^\circ$C]	1240
	Curie Temperature [$^\circ$C]	1140
	Density	1140
	Hardness [mohs]	5
	Relative permittivity (unclamped)	$\epsilon^S_{xx} = \epsilon^S_{yy} = 46.5, \epsilon^S_{zz} = 27.3$
	Relative permittivity (clamped)	$\epsilon^T_{xx} = \epsilon^T_{yy} = 28.1, \epsilon^T_{zz} = 84.1$
	Electrooptic tensor r [pmV^{-1}]	$r_{33} = 30.8, r_{13} = 8.6,$ $r_{22} = 3.4, r_{42} = 28$
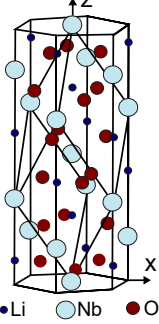
niobate exhibits negative birefringence with the principal ordinary and extraordinary refractive indexes $n_o = 2.211$ and $n_e = 2.138$, at $\lambda = 1.55\mu$m, respectively [18]. It stands out with a wide optical transparency (0.35-4.5 μm), and is thus well suited for application with operation wavelengths ranging from the visible to the mid-infrared. Its electro-optic coefficients are $r_{22} = 6.7$ pm/V, $r_{13} = 10.9$ pm/V, $r_{33} = 34$ pm/V and $r_{42} = 32$ pm/V. Lithium niobate crystal wafers can be commercially purchased in three common crystal orientations, namely the x-, y- and z-cuts, corresponding to the crystallographic planes defined by the Miller–Bravais indices (2$\bar{1}\bar{1}$0), (1$\bar{1}$00) and (0001), respectively. By choosing the correct crystal orientation with respect to the direction of the modulating electric field, the change in the refractive index can be maximized by exploiting the highest electro-optic coefficient r_{33}. For instance, a configuration in which the electric field is oriented along the out-of-plane direction of the crystal surface, z-cut lithium niobate with the principal axes of the crystal (optic axis) oriented parallel to the surface normal, maximizes the electrically-induced optical birefringence. The recently established ability to fabricate thin LiNbO$_3$ films with arbitrary crystal orientation on various substrates extended the spectrum of their possible applications. This also encountered a regain of research interest for this material as active component in nanophotonic applications. The reason for the continuing success of lithium niobate in optoelectronic applications is not because it exhibits the best properties regarding electro-optic activity, stability or processibility. Rather it provides a reasonable combination of all three. Furthermore, the relative dielectric constant ϵ_r, which determines the capacitance of a modulator device and consequently its operation bandwidth, is small in LiNbO$_3$ compared to other inorganic Pockels materials. However, there are also some significant drawbacks: its susceptibility to photorefractive damage, induced by modest intensities of light with wavelength around 480 nm, prevents high power application at visible wavelengths. Above 800 nm this effect disappears, making the material suitable for telecommunication applications with very good optical damage resistance. Another major disadvantage for the realization of miniaturized devices is that the material is notoriously difficult to process due to its inherent resistance to etching, resulting in conical structures and scattering losses caused by surface roughness. These limitations have led to the investigation of alternative materials.

Another well-studied inorganic material used in a variety of applications is barium titanate (BaTiO$_3$), which exhibits high Pockels coefficients of $r_{42} \approx 900$ pm/V and $r_{33} \approx 340$

TABLE 3.3: Comparison of the Pockels materials employed in nanophotonic applications. If not stated otherwise, the values for the physical properties are taken from the reference in which they have been employed as active material in a nanophotonic application (last column). The strain-free (clamped) relative permittivity $\epsilon_r^S = \epsilon_r$ is stated, relevant for high-speed applications. The relative permittivities of the majority of electro-optic polymers is not stated in the references, but are expected to be relatively small ($\epsilon_r \sim$ 2-5).

Material	r_{33} $[\mathrm{pmV^{-1}}]$	n at $\lambda = 1.55\mu m$	ϵ_r (strain-free)	T_C or T_g [°C]	Nanophotonic application
LN	31	$n_o = 2.22$ $n_o = 2.14$	$\epsilon_{33} = 28$ $\epsilon_{11} = 85$	1140	[109, 110], [Appendix C]
BTO	103	$n_o = 2.30$ $n_o = 2.27$	$\epsilon_{33} = 56$ $\epsilon_{11} = 2200$ [112]	120	[105, 111]
PZT	67	≈ 2.3	500-12000 [113]	180 [113]	[114]
EOP DR1	18 [115]	1.48	2.7-3.4 [116]	105	[117]
EOP SEO125	100 [118]	1.62 [118]	n/a	150 [118]	——
EOP M3	70	1.68	n/a	168	[19, 119]
EOP YLD-124	100	1.58	n/a	80-100	[96, 120–122]
EOP DLD-164	180	1.83	n/a	66 [123]	[95]

pm/V. Consequently, its electro-optically activity is more than 10 times larger than in lithium niobate. At room temperature, it has a tetragonal crystal structure with point group 4mm. At its Curie temperature of 120 °C, the material experiences a transition from the ferroelectric tetragonal to a paraelectric cubic phase (point group m3m), thus becoming centrosymmetrical and prohibiting Pockels activity above this temperature. As lithium niobate, it exhibits negative birefringence with the ordinary and extraordinary refractive indexes $n_o = 2.301$ and $n_e = 2.271$, at $\lambda = 1.55\mu m$, respectively [105]. The advantages of barium titanate as active material for electroptic modulation lie in the large Pockels coefficients, its mechanical strength, chemical durability, high optical damage threshold, wide transmission range (0.4-5 μm) and ease of processing. Over the past years, great progress has been made in integrating single crystal BaTiO$_3$ with silicon, which gave rise to the developing of a hybrid BaTiO$_3$/silicon technology [106–108]. Furthermore, it has been shown that the Pockels effect remains strong in nanoscale devices, thus emerging also as a suitable candidate for nanoscale plasmonic modulation [105].

Organic electro-optic (EO) polymers incorporating highly nonlinear chromophores are a new class of materials, which have led to new opportunities for ultra-compact integrated modulator devices. The polymer material comprises a host polymer which is doped with organic molecules (chromophores) with permanent dipole moment. For applying the material, the host polymer containing nonlinear optical chromophores is usually diluted in a solution and spun cast into films, leading to the deposition of randomly oriented chromophores. To achieve macroscopic second-order nonlinearity in this material, an electric poling process at elevated temperature close to the glass transition temperature T_g is required, in which the chromophores can freely rotate and align in response to an externally applied electric field due to the torque on their molecular dipole moments. Once the temperature is decreased far below T_g, the non-centrosymmetric orientational order is locked and second order nonlinear processes as the Pockels effect are enabled. In practice, the electrodes for driving the modulation can initially be used for applying the electric field by two on-chip coplanar electrodes, thereby enabling local and

homogeneous poling of the EO polymer between the electrodes. This technique is the most commonly used poling method and refers to the contact poling technique. It is appropriate to mention that the electric poling is considered the most troublesome processing step for the realization of polymer-based modulation. Contact poling attempts conducted throughout the PhD project demonstrated the complexity of successful and efficient poling of commercially available EO polymers. Excessive charge injection from the biased metal electrodes often results in large current that causes dielectric breakdown in polymer films due to the low dielectric strength of the material, leading to irreversible damage of the device structure. However, once efficiently poled, the material can exhibit large Pockels coefficients (ranging from 100 pm/V until 400 pm/V) which can also be incorporated at the nanoscale for ultra-compact modulator devices. From the initial difficulties of the chemical synthesis of polymers with high electro-optic coefficients and their processing to functional EO devices, recent progress reported by Dalton et al. [124] has drastically improved the material stability and reliability, which has driven recent progress in high-performance polymer modulator devices. Besides the demonstrated modulators based on silicon–organic hybrid (SOH) platforms, plasmonic devices in which the confined optical signal in a polymer-filled plasmonic slot waveguides is efficiently modulated by biasing the incorporated metal electrodes. This approach has led to the most efficient and fastest modulator operation ever presented to date. Despite the high electro-optic activity in EO polymers, there is a critical property which hinders their practical deployment in real applications. As discussed above, the thermal stability of the EO polymer is limited by T_g, at which the material looses its electro-optic activity. To date, T_g in applicable polymers is ranging between 50°C and 150°C. The fact that depoling is a thermodynamic process which occurs gradually and starts noticeably (approx. 30 °C [122]) below the material's glass transition temperature, prevents long-term environmental stability of many EO polymers and thus its applicability in many telecommunication applications. Recently, much research effort is devoted to improve the stability of EO polymer materials by further increasing the glass transition temperatures. The summarizing Table 3.3 compares the characteristic properties of applicable material platforms.

3.2.3 Device architectures and performance metrics

Due to the electro-optical modification of the refractive index in a Pockels material, light undergoes a controllable modulation in its optical phase as it travels through the medium. This is utilized in EO devices, while the exact device architecture depends on the specific application. First devices were Pockels cell type modulators, consisting of a crystal of an electro-optic material with electrodes located at two parallel crystal surfaces. Applying a voltage across those electrodes modulates the refractive index and the laser beam passing through the crystal experiences a phase shift. Accordingly, the required voltage to achieve a phase shift of π is dictated by the crystal dimension, e.g. the length L the beam travels through the crystal and the spacing d between the parallel electrodes, and therefore following the equation

$$V_\pi = \frac{d\lambda}{2r_{33}n_o^2 L} \,. \tag{3.15}$$

Low driving voltages therefore require narrow electrode spacing d and an increased length L of beam propagation through the crystal. Considering the inherent beam divergence of a focused Gaussian beam, d can only be reduced for a certain length when the beam waist is narrow, before it diverges again. This fundamental limitation in device efficiency of free-space light interconnections has led to the development of more
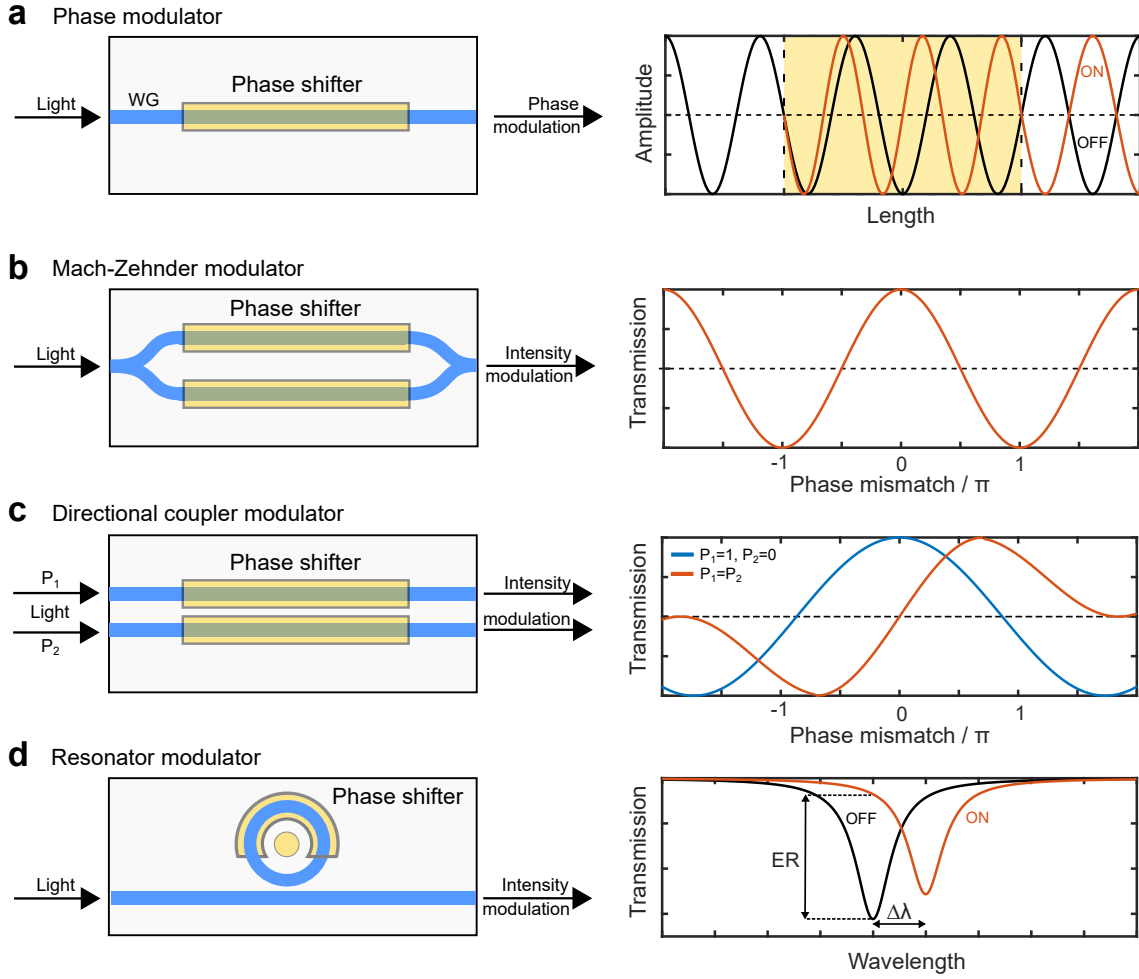
FIGURE 3.5: Schematic of waveguide-based electro-optic modulators. The simplest type of electro-optic modulator is a phase modulator (**a**), which forms the basis for amplitude modulation accomplished by embedding phase modulation in Mach-Zehnder interferometers (**b**), directional couplers (**c**) or ring resonators (**d**).

efficient integrated modulator technologies in which integrated optical waveguides are utilized to maintain high optical confinement within a small cross-section over its entire length.

In the context of developing integrated device platforms in this thesis, four basic modulator configurations are reviewed and discussed. The simplest type of electro-optic modulator is a phase modulator containing only a single waveguide and driving electrodes. The optical signal is inserted into the phase shifter, where the refractive index of the waveguide medium in which the optical signal propagates, is modulated by an electric field introduced by biased electrodes. For a guided mode, the modification of the propagation medium leads to the difference $\Delta\beta = \beta_{on} - \beta_{off}$ in the propagation constant between the ON ($\beta_{on} = k_0 n_{eff,on}$) and OFF ($\beta_{on} = k_0 n_{eff,off}$) states of the modulator. The length along the propagation direction where the modulation occurs, is naturally connected with the electrode length, which defines the length L of the phase shifter. Then, the optical carrier phase shift introduced by the Pockels effect is

$$\Delta\phi(V) = \Delta\beta(V)L,\tag{3.16}$$

where V is the voltage applied on the electrode. It is clear that the strength of phase modulation depends on the electro-optic response introduced by the applied voltage and the device length. Hence, there is a trade-off between driving voltage and device footprint. The modulated (optical) electric field at the output can be described by

$$E(V) = E_0 e^{i(\omega t - \Delta\phi(V))} . \tag{3.17}$$

The voltage required to produce a phase retardance of π at the modulator output is defined as the half-wave voltage V_π (Figure 3.5a).

The electro-optically induced phase delay alone does not affect the intensity at the device output. However, there are three ways of converting an electro-optically induced refractive index change into modulation of the optical intensity. Firstly, a phase modulator placed in one branch of an interferometer can function as an intensity modulator. By changing the refractive index in the medium of two interfering waveguides, the phase shift introduced on one waveguide relative to the reference waveguide, leads to constructive or destructive when recombined. For on-chip applications, usually a Mach-Zehnder interferometer (MZM) is used, in which light is split into two well-seperated interferometric waveguide arms and traverses the individual waveguide paths only once. A phase difference in the interferometer arms can arise either by a difference in path length producing corresponding changes in phase shift or by phase variations caused by refractive index variations in the individual waveguides. Let an MZM consists of one EO phase modulator placed in one of the interferometric arms. The optical electric field at the output can then be described by

$$E(V) = \frac{E_0}{2} \left(e^{i(\omega t - \Delta\phi(V))} + e^{i\omega t} \right) . \tag{3.18}$$

Due to the interfering electric fields, any voltage will change the intensity accordingly, thus achieving intensity modulation, described by the transfer function at the device output

$$I(V) = \frac{I_0}{2} \left(1 + \cos\left(\frac{V}{V_\pi} \pi \right) \right) . \tag{3.19}$$

It is clear that the quantity V_π denotes the voltage required to modulate from high optical intensity (maximum transmission) to no intensity (minimum transmission) or vice versa, thus also refered as driving voltage. Some MZM allow push-pull operation, where the voltage is applied across both arms with equal magnitude but opposite sign with respect to each other. The interferometer arms experience opposite phase retardance, which allows to achieve a π-phase difference in ther interferometer arms at smaller interaction lengths. In fact, the push-pull operation improves the device efficiency by reducing the required length by a factor of 2, when compared with single-arm operation at the same driving voltage. Another way of converting a change of refractive index into intensity modulation, is by utilizing a directional coupler consisting of two closely spaced waveguides, again with driving electrodes placed along the interaction length.

The interaction length is inherently chosen such that the passive device exhibits the desired intensities at the two output channels. For instance in a conventional directional coupler switch, when the input signal is present in one waveguide, the optical signal will cross over the adjacent waveguide once the interaction length coincides with the coupling length. By applying a voltage, the coupling characteristics change and optical power is transferred back to the initial waveguide. The exact behavior of the intensity distribution in the output channels as a function of the change in the propagation constants is not as

intuitive as in an interferometric system, but can be analytically described by the coupled-mode theory (CMT). The full derivation of the transfer curve in a directional coupler modulator can be found in the Supplementary Information of Appendix C. Note, that a directional coupler switch is inherently less efficient than a MZM. The voltage that needs to be applied is larger than V_π to fully switch the power, i.e. performing the transition from minimum to maximum power in one output channel. For a conventional directional coupler switch, the required voltage for full switching corresponds to $\sqrt{3}V_\pi$, while for a directional coupler which is fed with equal power distribution in the input channels, as the device demonstrated in this thesis, the required switching voltage is $\sqrt{2}V_\pi$.

Another way of transitioning Pockels modulation into an intensity modulation is to use cavity enhancement in ring resonator architectures such as shown in Figure 3.5d. By electro-optically changing the resonance condition, the device can be switched on- and off-resonance at a given operation wavelength. This has the advantage of requiring a lower drive voltage due to a high quality factor Q in the resonator, but concurrently comes at the cost of a narrow spectral range of operation. It is also to be noted that high Q resonators have a long photon lifetime which limits the rate at which optical power can be injected or extracted, so that the modulation speed is intrinsically limited.

While each of these device architectures has its advantages and disadvantages, the overall performance is dictated by the efficiency of the basic structural framework, namely the waveguide composition, of which the individual modulator architecture is build of. Generally, this includes that the performance not only depends on the Pockels coefficients of the material embedded in the device, but also on the light-mater interaction dictated by the dimensions of the waveguide and the incorporated confinement of light to the EO material. In this context the half-wave voltage-length product $V_\pi L$ has emerged as a useful figure of merit. It is the product of the active device length L and voltage required to introduce a phase shift of π with respect to the reference signal in passive operation mode. The ultimate goal of a modulator design is to achieve the smallest possible $V_\pi L$ (i.e. smallest footprint with the least required voltage). A reduced voltage-length product leads to further performance benefits with respect to modulation bandwidth and energy consumption. Shorter devices possess smaller capacitance C, which determines the -3 dB cutoff point of the frequency according to

$$f_{-3dB} = \frac{1}{2\pi RC}, \tag{3.20}$$

with the resistive load R. Similarly, the small capacitance combined with low required driving voltages leads to low electric power consumption per bit according to [125]

$$E_{bit} = \frac{1}{4}CV^2. \tag{3.21}$$

By utilizing plasmonic waveguides as the basic structural basis for the realization of EO devices, all the figures-of-merits discussed above can be significantly improved as demonstrated in Appendix C. With all the benefits that come along with a strong optical confinement in the EO material by utilizing plasmonics, there is a parameter that must be considered for some applications where the optical loss is crucial. It is commonly stated as optical insertion loss IL, which measures the loss of optical power resulting from inserting the device into the photonic circuit. In the literature, this is often including the contributions from proagation losses α rather then the total losses that come along with insertion. The coupling losses, which can even be the dominant source of loss, are often excluded from this parameter since the coupling structure is often treated independently with its own performance specifications. The propagation loss in a device underscores

the importance of improving the electro-optic device efficiency, which permits shorter devices to be employed for the same operation voltage. To evaluate the device performance, also with respect to its insertion losses, the half-wave voltage-length-loss product $V_\pi L \alpha$, commonly stated in VdB can be applied. Accordingly it specifies V_π with an insertion loss of 1 dB, or the insertion loss $IL = \alpha L$ at a specific voltage, to achieve a π phase shift. Undoubtedly, for plasmonic waveguides the ohmic losses will drastically contribute to the insertion loss. The typical propagation loss of SPPs is in the range of 0.5 dB/μm which is significant higher than the losses in nanophotonic waveguides far below 1 dB/cm. Since the improved voltage-length product in plasmonic structures cannot fully compensate the losses with respect to this FoM, to date low voltage-length-loss products of a few VdB have only been demonstrated in photonic devices [114].

3.2.4 Long-range DLSPP waveguide modulators

Following on the study of employing lithium niobate as the active medium in plasmonic strip waveguides for high-density integrated and efficient modulation, we explore in this section a less lossy modulation system by utiliizing long-range DLSPP waveguides, which features a drastically reduced voltage-length-loss product $V_\pi L \alpha$. The main idea is to advantageously exploit the circumstance that the DLSPPW mode field, with its maximum at the metal-dielectric interface, is in very close proximity to the driving electrode, thus allowing a great field overlap between driving electrostatic field and the optical field, while keeping the optical losses due to ohmic interactions in the metal low. Leaving detailed considerations of this configuration and its experimental deployment in a modulator device for future studies, here a theoretical design analysis is conducted with the goal of realizing a plasmonic modulator with reduced losses and high efficiency.

The modulator device is composed of two identical parallel waveguides. Each individual waveguide consists of a thin Au strip, which is embedded symmetrically in the vertical axis into a TiO$_2$ ridge and deposited on a 500 nm thick LiNbO$_3$. This composition is supported by a bulk SiO$_2$ substrate. In the device, the two co-planar thin metal strips, each having a thickness of 15 nm and width of 400 nm, are utilized as driving electrodes for the introduction of an electrostatic field. Applying a voltage on one electrode while keeping the counter electrode grounded, leads to an electrostatic vector field with alternating out-of-plane field components in the z-cut LN layer with strongest field out-of-plane components at the metal-LN interface of the plasmonic waveguides (Figure 3.6a). According to Equation 3.9, an opposite refractive index modification is introduced due to the Pockels effect, which inherently allows push-pull operation of the modulator device (Figure 3.6b). The plasmonic mode experiences the variations in the refractive index which affects its propagation constant. The corresponding electro-optically induced phase mismatch in the individual waveguides can eventually be used for the operation of various modulator devices.

As the optical characteristics of this plasmonic waveguide were investigated in Chapter 2.4.3 for the same material composition, it has been found that the transmission loss is generally dependent on the ridge dimensions, showing small losses when the plasmonic mode around the thin film (15 nm) gold strip is equally distributed between the 500 nm thin-film dielectric (z-cut LN) and the dielectric ridge (TiO$_2$). The modulation efficiency will be exclusively determined by the field inside the active medium, e.g. the lithium niobate film. To maximize the modulation efficiency, it is therefore beneficial to reduce the ridge height for a given LN thickness, which leads to a larger fraction of the optical field being located in the active medium. To investigate this geometrical dependence on the device efficiency and its interplay with the propagation losses, we calculate the voltage-length product $V_\pi L$ and the voltage-length-loss product $V_\pi L \alpha$. This is done
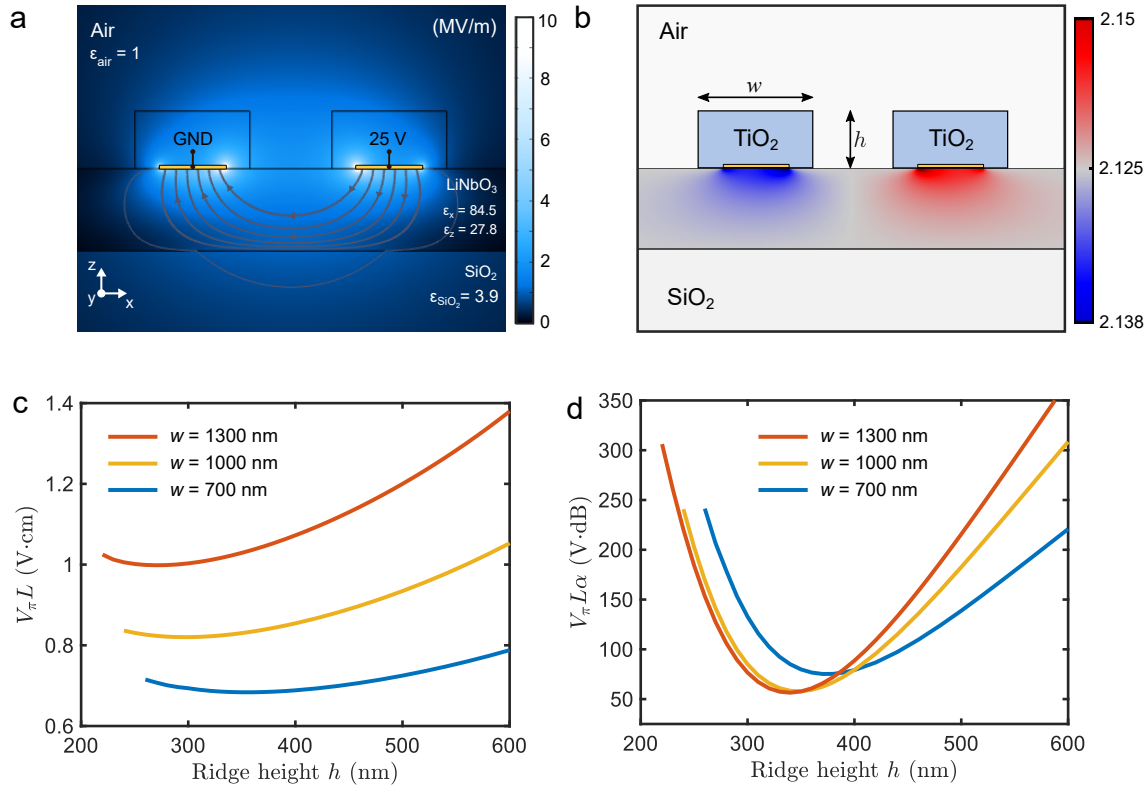
FIGURE 3.6: Electro-optic modulator based on long-range dielectric-loaded surface plasmon polariton waveguides. **a** Color-coded electric field and its contours in LN upon applying a bias of 25V. **b** Due to the linear Pockels effect in the LN substrate, the extraordinary n_e refractive index underneath the left wire is decreased, while being increased by an equal amount in the right guide. **c-d** The geometrical dependence of the voltage-length product $V_\pi L$ and the voltage-length-loss product $V_\pi L\alpha$ is analyzed.

for varying ridge height h and width w, while keeping the LN thickness constant to 500 nm, as well as the (15 nm $\times$ 400 nm) Au strip and the seperation distance ($s = 500$ nm). As previously highlighted, the electro-optic efficiency designated by $V_\pi L$ decreases with reduced ridge height for all investigated ridge widths (Figure 3.6c). Depending on the geometry, it can reach values far below 1 Vcm, which is lower than any LN modulator device based on photonic wavegudie platforms. The slight increase in $V_\pi L$ for very mall ridge heights is associated to mode leakage into the LN layer. This effect becomes more significant and dominant when considering the interplay between efficiency and loss, leading to a pronounced increase in $V_\pi L\alpha$ for small waveguide heights. Interestingly, for each waveguide width, there is an optimum waveguide height which minimizes $V_\pi L\alpha$. This serves as a guideline for the waveguide design, when aiming less-lossy modulator configurations which simulationsly exhibit high modulation efficiencies.

Chapter 4

Conclusions

Within this PhD thesis, plasmonic-bases passive and active nanophotonic technology has been developed and we explored its suitability as instrumentation for nanoscale application. Sub-wavelength routing, detection and manipulation of light has been demonstrated and quantitatively characterised in an systematic manner. Firstly, it has been shown that two subwavelength separated parallel slot waveguides can act as an ultra-compact and branchless Mach–Zehnder interferometer with promising application possibilities in sensing or optoelectronic devices. Optical losses and complexities in the fabrication process which are associated with waveguide branches are entirely eliminated. The unfavorable influence of crosstalk between the adjacent transmission channel is minimized by choosing sufficient, but still sub-wavelength, waveguide separation, leading to high extinction ratios in ultra-compact plasmonic Mach-Zehnder interferometers.

Secondly, we made use of plasmonic waveguides that provide natural integration compatibilities of electronic and photonic devices. By integrating a spin-selective directional antenna in combination with two germanium photodetectors, we demonstrated spin-controlled directional routing and detection in a single plasmonic nanocircuit. With potential applications in spin-encoded communication technology or compact polarimetry, the presented study emphasizes the attractive integration capabilities of plasmonic nanocircuits.

With the ambition of developing a reliable and efficient modulator technology, we demonstrated for the first time a plasmonically-enhanced directional coupler switch, which utilizes the Pockels effect in lithium niobate. For decades, this ferroelectric material has been the best suitable choice of Pockels materials owing to its excellent combination of mechanical and nonlinear optical properties. Incorporating the advantageous material characteristics with the attractive features of plasmonics provides improvements in the device performance compared to previously reported studies. This study thus stimulates the long-standing ambition for the photonic and telecommunication community of seeking optoelectronic devices which are more compact, efficient, reliable, high-speed, broad bandwidth, and less power-hungry than existing technologies.

This progress can be illustrated by the historical development of electro-optic modulators with respect to the device efficiency, represented by the voltage-length product $V_\pi L$ (Figure 4.1). By far, bulk lithium niobate has the longest history of being incorporated in modulator devices, which makes it the most extensively studied Pockels material. The reported efficiencies of commercially available devices are stated around 5-10 Vcm, which was believed to be saturated without much potential of improvement. New platforms such as thin-film lithium niobate emerged in the mid-2010s, which has led to a resurgence in the development of integrated photonics based on lithium niobate, by reducing $V_\pi L$ down to 1.8 Vcm. At the same time, other material platforms found their way to be employed in practical devices. Due to larger Pockels coefficients in alternative materials, device efficiencies could be drastically improved in recent years. Noticeably,
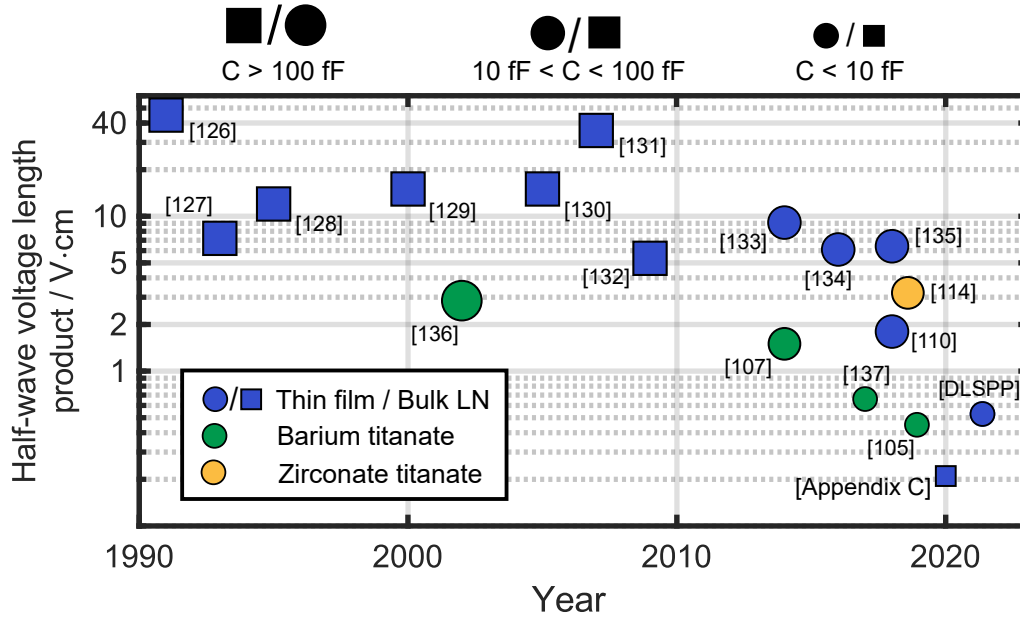
FIGURE 4.1: Development of the efficiency $V_\pi L$ and capacitance C of solid-state electro-optic modulators over the last 30 years. The size of the symbol indicates the capacitance C, limiting the speed of operation to maximum 30 GHz for $C < 100$ fF and 300 GHz for $C < 10$ at a resistive load of 50 Ω. The color and shape of the symbol indicates the material platform the particular device relies on. The considered ferroelectric solid-state material platforms are bulk lithium niobate [126–132], thin film lithium niobate [110, 133–135], barium titanate [105, 107, 136, 137] and zirconate titanate [114].

the $V_\pi L$ of 0.45 Vcm in BTO could only be obtained by taking advantage of plasmonics. The obtained $V_\pi L$ of 0.25 Vcm in this thesis is the lowest reported value achieved in inorganic Pockels modulators and is almost one order of magnitude smaller than any other reported device based on lithium niobate. Considering that this material still holds a key position in communication applications, this pioneering work of combining this material platform with plasmonics may pave the way to optoelectronic technology that meets future needs for efficiency, compactness and low power consumption. To eliminate the only major drawback of a relatively high insertion loss of 5.5 dB, we proposed a modulator device based on long-range DLSPP waveguide that reasonable compromises the modulation efficiency with a drastic reduction of propagation losses.

Appendix A

Ultra-compact branchless plasmonic interferometers

PAPER

Check for updates

Ultra-compact branchless plasmonic interferometers†

Martin Thomaschewski, [ID] * Yuanqing Yang [ID] and Sergey I. Bozhevolnyi [ID]

Miniaturization of functional optical devices and circuits is a key prerequisite for a myriad of applications ranging from biosensing to quantum information processing. This development has considerably been spurred by rapid developments within plasmonics exploiting its unprecedented ability to squeeze light into subwavelength scale. In this study, we investigate on-chip plasmonic systems allowing for synchronous excitation of multiple inputs and examine the interference between two adjacent excited channels. We present a branchless interferometer consisting of two parallel plasmonic waveguides that can be either selectively or coherently excited *via* ultra-compact antenna couplers. The total coupling efficiency is quantitatively characterized in a systematic manner and shown to exceed 15% for small waveguide separations, with the power distribution between the two waveguides being efficiently and dynamically shaped by adjusting the incident beam position. The presented design principle can readily be extended to other configurations, giving new perspectives for highly dense integrated plasmonic circuitry, optoelectronic devices, and sensing applications.

Introduction

The past few decades have witnessed impressive progress in the development of miniaturized electronic and photonic devices, driven by the ever-growing demand for faster information transfer and processing capabilities. Plasmonics – the science of utilizing engineered metallic structures to trap, guide and manipulate light *via* surface plasmon polaritons (SPPs) – has empowered us to break the diffraction limit and pave the way for truly nanoscale optical circuits with unprecedented integration and desired functionality.[1–5] In this regard, plasmonic waveguides, serving as the workhorses of such nanocircuits, have received considerable attention becoming a subject of intensive studies.[6–12] A plethora of various waveguide geometries and device configurations has thus been demonstrated, with fundamental breakthroughs and applications in various areas such as optical communication,[12–17] biosensing[18–20] and quantum optics.[21–23] In the quest to realize plasmonic nanocircuits with increasing complexity and compactness, it is indispensable to address the critical issue of crosstalk caused by adjacent transmission channels. Indeed, in any modern integrated circuits with massive parallelism, electromagnetic interference and resulting crosstalk always exist in a general sense and can signifi-

cantly affect the performance of a system. However, despite tremendous advances in the field of plasmonic nanocircuits, the majority of previous studies have only focused on individual waveguides or serial architectures with a single input.[24–28]

Here, we report a theoretical and experimental study of plasmonic nanosystems with two closely packed waveguides enabling parallel communication at telecom wavelength. Just like their electronic and microwave counterparts, plasmonic parallel transmission systems provide the cornerstone for large integrated nanocircuits and promise many practical applications due to their high speed and enhanced information density. Selective and simultaneous excitation of individual or both waveguides in the system are demonstrated by exploiting an ultra-compact nanoantenna coupler. The coupling efficiency of the system is quantitatively characterized in a systematic manner. We show that up to 17% of the free-space incident energy from the air side can be synchronously coupled to two propagating plasmon modes, and that by varying the relative position of the incident beam the power ratio between the two modes can be dynamically tuned. Furthermore, such parallel waveguiding geometry naturally offers itself the ability to function as a fundamental interference unit, without any additional bends or splitters. This enticing property can directly mitigate insertion or bending losses and make the structures substantially easier to fabricate. Developing further this idea, we propose and demonstrate a branchless plasmonic Mach–Zehnder interferometer (MZI), observing its coherent output from the two transmission channels. We envision that our findings can substantially facilitate

*Centre for Nano Optics, University of Southern Denmark, Campusvej 55,
DK-5230 Odense M, Denmark. E-mail: math@mci.sdu.dk*

further miniaturization of many plasmonic devices. For instance, the most compact plasmonic modulators demonstrated so far[13] can substantially be shrunk by replacing bulky grating couplers and splitting elements with the presented parallel design.

Results and discussion

The proposed configuration (Fig. 1) consists of two subwavelength-separated plasmonic slot waveguides, individually fed by impedance-matched nanoantennas[26,29] considered as one of the most compact solutions for a slot waveguide excitation. The pair of dipole antennas with a common side reflector is illuminated with a diffraction-limited focused Gaussian beam polarized along the long axis of the antennas. Electromagnetic radiation is captured by the antenna pair and the induced resonant charge oscillations in each individual antenna are launching surface plasmons polaritons (SPP) into the plasmonic slot waveguides (PSWs). The characterization of the proposed double PSW system is carried out in two steps. In the first step, we use the finite-difference time-domain (FDTD) method[30] to extensively investigate the modal properties supported by this system. The geometrical requirements for a coherent transmission with low cross-talk are defined. On this basis, the structures are designed, fabricated and characterized.

We start by examining the properties of a single plasmonic slot waveguide that constitute the transmission system in our study. To reduce mode leakage into the glass substrate (n_{glass} = 1.45), a 300 nm-thick dielectric layer (PMMA, n_{PMMA} = 1.49) is used to cover the PSW. Here, we focus on the PSW modes at the telecom wavelength λ_0 = 1550 nm, and employ the optical
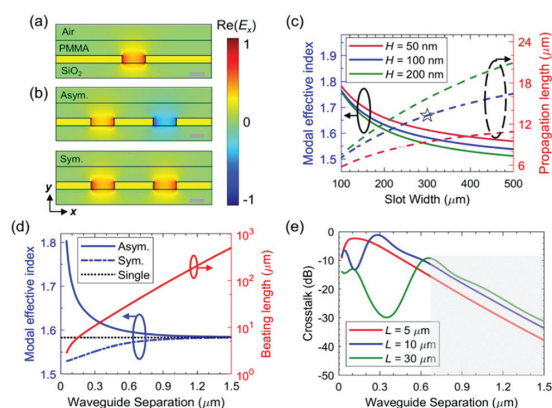
Fig. 2 Analysis of transmission systems consisting of individual or parallel plasmonic slot waveguides. (a) Mode profile Re(Ex) of a single plasmonic slot waveguide with metal thickness H = 100 nm and slot width W = 300 nm. The yellow colour represents the gold material. (b) Field distributions of anti-symmetric (upper panel) and symmetric (lower panel) modes of a parallel plasmonic waveguiding system with H = 100 nm, W_{slot} = 300 nm and W_{sep} = 500 nm. The scale bars in (a) and (b) represent 200 nm. (c) Modal effective index (solid lines, left y-axis) and propagation length (dashed lines, right y-axis) of the fundamental mode supported by single plasmonic slot waveguides with variant geometric sizes. The star symbol points out the geometric size used in our study, *i.e.*, H = 100 nm, W_{slot} = 300 nm. (d) Modal effective index (left axis) of the two eigenmodes supported by the parallel plasmonic waveguiding system with varying separations W_{sep} and fixed H = 100 nm and W_{slot} = 300 nm. The black dotted line shows the property of a referenced single plasmonic waveguide with the same H and W. Beating length L_c of the system (red line) is plotted in the right y-axis. (e) Function of the cross-talk between the two parallel plasmonic slot waveguides with respect to separation distance. Scenarios of three different device lengths L are considered and the shaded area indicates the weak-coupling region where the crosstalk C < −10 dB.
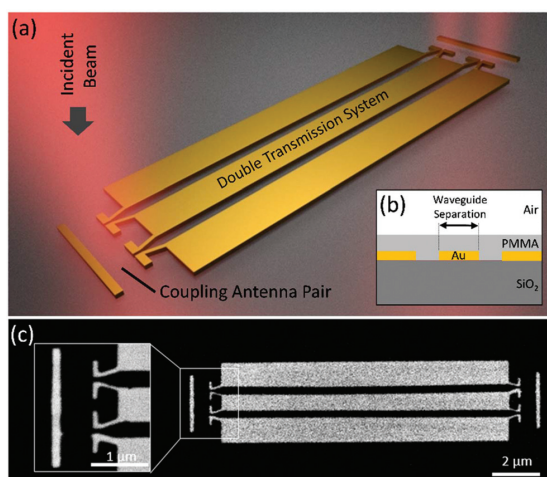
Fig. 1 (a) Three-dimensional rendering of the proposed parallel PSWs fed by a pair of optical-loaded nanoantennas with side reflectors at the input and output ports. (b) Schematic cross-section and (c) top-view SEM images of a fabricated device are illustrated.

constants of gold reported by Johnson and Christy.[31] A representative field distribution of the fundamental mode supported by single PSWs is shown in Fig. 2a. The function of its modal effective index and propagation length with respect to slot width W_{slot} and variant metal thickness H are depicted in Fig. 2c. With decreasing slot width, a larger overlap between the mode profile and the metal gives rise to an increase in the model index accompanied with a decrease in the propagation length. To maintain a relatively low loss characteristic while keeping the whole device thin and compact enough, we choose a balanced set of geometric sizes as H = 100 nm and W_{slot} = 300 nm for the single PSWs, as indicated by the star symbol in Fig. 2c. Then we investigate the optical transmission system consisting of two parallel PSWs, which is in the following stated as the double PSW. Different from the single PSW, the double PSW system can support two orthogonal eigenmodes, characterized by anti-symmetric $E_a(x, y)$ and symmetric $E_s(x, y)$ field distributions, as shown in Fig. 2b. The total electric field in the system E_{total} can thus be expressed as a linear superposition of the two modes: $E_{total} = A_a(z)E_a + A_s(z)E_s$, where modal amplitudes $A_a(z)$, $A_s(z)$ can be given by $A_a(z) = A_a(0)$exp

$(-j2\pi n_a z/\lambda_0)$ and $A_s(z) = A_s(0)\exp(-j2\pi n_s z/\lambda_0)$ with the corresponding effective modal indices n_a and n_s of the anti-symmetric and symmetric modes, respectively. In Fig. 2d, we plot the functions of these two modal indices n_a and n_s with respect to waveguide separation W_{sep}. An asymptotic behaviour can be clearly seen when W_{sep} approaches the limit $W_{sep} \sim \infty$. In this case, both eigenmodes approximate the fundamental mode of the single PSW and thus the whole system function as two uncoupled PSWs (ESI Fig. S1†). By contrast, when W_{sep} gradually approaches to the other limit $W_{sep} \sim 0$, a large spatial overlap between the fields inside two closely adjacent PSWs would cause significant coupling, which can be quantified by the beating length $L_c = \lambda_0/2|n_a - n_s|$. A smaller L_c implies stronger coupling and associated higher crosstalk between the two channels. To further unambiguously reveal the influence of the crosstalk in practical devices, in Fig. 2e we show the crosstalk between the two channels for different device lengths L. We evaluate the crosstalk C by defining it as $C = P_t/P_0$, where P_t is the power transferred from one waveguide to the other and P_0 is the power of the original signal. With the mean propagation length $L_p = \lambda_0/2\text{Im}(n_a - n_s)$ and an assumption that $\text{Im}(n_a - n_s) \ll \text{Re}(n_a - n_s)$, the crosstalk can be calculated as follows:[32]

$$C \cong 10\log_{10}\left[\exp\left(-2\frac{L}{L_p}\right)\sin^2\left(\frac{\pi}{2}\frac{L}{L_c}\right)\right].$$

The first exponential term renders the propagation loss factor in the coupler of a given length L. The sine function in the above equation reflects the power exchange of two PSWs for small separations with the coupling length becoming much smaller than the device length ($L_c \ll L$). This regime of periodic power exchange between the adjacent waveguides can also be identified from Fig. 2e, and is in the following termed as the strong coupling regime. To minimize the unfavorable crosstalk (<−10 dB), we focus in the following experimental study on the design with two PSWs being sufficiently well separated, so that their coupling falls into the weak-coupling regime. This requires the coupling length to become much larger than the investigated device lengths ($L_c \gg L$), as denoted by the shaded grey area in Fig. 2d.

For the experiment, all investigated structures are fabricated on SiO_2 using electron-beam lithography (EBL) followed by thermal gold evaporation and subsequent metal lift-off. A 300 nm thin layer of PMMA is deposited by using the spin-coating technique. The scanning electron microscope (SEM) image in Fig. 1c depicts a fabricated double PSW with the zoomed view of one nanoantenna pair. Transmission measurements were performed with a home-built inverted microscope setup, having the sample mounted on a three-dimensional stabilized piezo translation stage with 20 nm spatial resolution. A linearly polarized laser beam with the wavelength of $\lambda_0 = 1550$ nm was focused by a high numerical aperture objective (NA = 0.95 dry) to a diffraction-limited FWHM width of $\varnothing = (2.3 \pm 0.1)$ μm. We first demonstrate the transmission experiment on a structure with a waveguide separation of

1.1 μm, to ensure that the two waveguides can be selectively excited while the scattering signal of each individual antenna can still be resolved. The excitation of the two parallel gap modes was shown to be sensitive to the relative position between the feeding point (*i.e.* center of incident Gaussian beam) and antenna pair. For comparison, Fig. 3a–c shows the reflection images captured by the camera with three different relative beam positions, with the output spot moving in accord with the incident beam positioning from the upper out-coupling antenna (Fig. 3a) to the lower one (Fig. 3c). For the symmetric location of an incident laser beam, both waveguides are excited equally with two output spots indicating coherently excited and spatially separated wavefronts transmitted from the antennas (Fig. 3b). It is thereby shown that the adjustment of the focused incident beam location on the antenna pair structure enables efficient shaping of the power distribution routed through the double slot waveguide system.

To investigate quantitatively the in-coupling conditions, we designed several structures with varying waveguide separation distances. The total coupling efficiency C_{tot} can be determined by measuring the incident optical power P_{in} and the optical power P_{out} radiated from the transmitting antenna pair. The incident power P_{in} is estimated by measuring the power P_R reflected from a flat gold film on the investigated sample, and by assuming $P_R = P_{in} \cdot T_{PMMA}^2 \cdot R_{Au}$ with the transmission coefficient $T_{PMMA} = 0.96$ of 300 nm thick PMMA and the reflectance coefficient $R_{Au} = 0.98$ of 100 nm Au for $\lambda_0 = 1550$ nm. Due to reciprocity and symmetry of the system, the coupling characteristics of the receiving antenna pair are identical with the antenna pair of transmission. Considering an exponential intensity decay of the electric field amplitude along the propagation direction the total coupling efficiency can be expressed as $C_{tot} = C_{Ant} \cdot e^{-L/L_p} \cdot C_{Ant} = C_{Ant}^2 \cdot e^{-L/L_p} = P_{out}/P_{in}$, where L_p is the propagation length of the two waveguide modes and C_{Ant} is the coupling efficiency of the antenna pair.
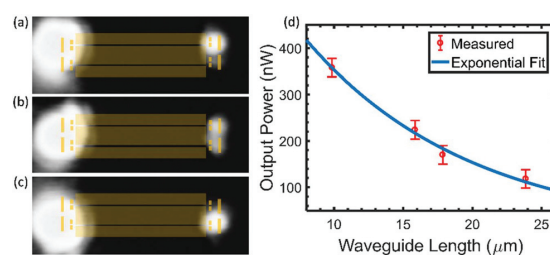
Fig. 3 (a–c) Far-field optical characterization at $\lambda_0 = 1550$ nm reveals selective waveguide excitation at beam position: (a) beam positioned at the upper antenna, (b) beam positioned centred between nanoantennas and (c) beam positioned at the upper antenna for a double PSWs with 1100 nm separation. The input and output antenna pairs with the waveguide structure are superimposed as a guide to the eyes. (d) Output intensities *versus* waveguide length are plotted and fitted as a first-order exponential decay function. The blue points represent the measured output power and the red line is the fitting graph.

To calculate the coupling efficiency C_{Ant}, we first determine the propagation length L_p by measuring the transmission for a series of double PSW systems with different lengths and the excitation beam centered at the input antenna pair (see Fig. 3d). The calculated propagation length of 12.3 μm is in good agreement with the measured propagation length of 12.0 μm, which is used in the following for the calculation of the in-coupling efficiency of the antenna pair. Fig. 4a depicts the measured in-coupling efficiencies exemplarily for four different waveguide separations as a function of the relative beam position and the waveguide separation. Structures with a large waveguide separation distance above 800 nm show a maximized coupling efficiency, when the incident beam coincides with one of the individual antennas. At this regime of separation, the energy provided by the diffraction-limited beam is mostly directed into one waveguide. For smaller waveguide separations, we observed a maximized coupling efficiency when the beam is positioned between the individual antennas. Here, more power is captured into the double waveguide system, due to a closer match between excitation spot and effective area of the antenna pair. It is noteworthy that, although the excitation beam is highly focused, and the maximum of the Gaussian beam is positioned between the antennas, it can still exceed the efficiency obtained by a single waveguide system by 10% (see Fig. 4b).

On-chip interference can be demonstrated by branching the two simultaneous excited channels. Therefore, we fabricated a set of MZI with different physical path lengths between both interferometer arms (ESI Fig. S2†), and thus inducing a phase difference between the two channels ranging from 0 and 2π. As a result, the optical signal collected from the single antenna at the output port is modulated by constructive or destructive interference (Fig. 5). For further miniaturization of the interferometer, we investigated branchless systems with waveguide separation below 800 nm. At this regime of separation, we noticed an overlap of the signal emitted from the two out-coupling antennas driven by the transmitted signal. The two lobes in the image plane merge due to spatially overlapping wave fronts. Due to the far-field interference of the waveguide-driven nanoantennas, the scattering spot can reveal

Fig. 4 Dependence of in-coupling efficiency on the waveguide separation distance and the relative beam position. (a) Measured coupling efficiencies are exemplarily shown for four different waveguide separation distances (red dots), which dependency on the relative beam position can be well approximated by a sum of two Gaussians, shown as purple lines. (b) Coupling efficiency when the relative beam position coinciding with the centre of the antenna pair, illustrated as a slice in (a). The calculated results are plotted in blue, while the red circles show the efficiencies obtained from the experiment. The black dashed line represents the maximum coupling efficiency measured for a single plasmonic slot waveguide system fed by one single nanoantenna.

Fig. 5 SEM image of Mach–Zehnder Interferometer with a nominal optical phase difference of (a) 0 and (c) 3π/4, with the corresponding far-field images (b) and (d). The scale bars in (a) and (c) represent 2 μm. (e) Measured and calculated normalized optical power output *versus* measured relative phase difference with the beam positioned between the antennas.
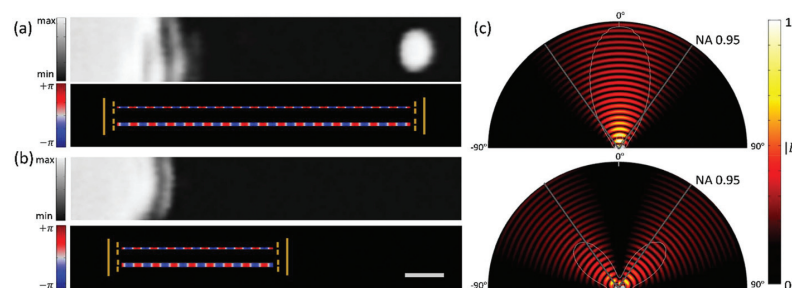
Fig. 6 Asymmetric double plasmonic slot waveguides consisting of two waveguides with the width of 150 nm and 300 nm, respectively. By varying the device length, the relative phase is adjusted to be in-phase (a) and out of phase (b). The far-field images (top) and the simulated waves (bottom) and are respectively shown for structures with a waveguide separation of 700 nm. The scale bar represent 1 μm. (c) Simulated far-field interference pattern of two separated dipole emitters radiating in phase (top) and out of phase (bottom). The white line illustrated the radiation pattern and the grey line shows the acceptable detection angle of the used optical system.

information about the relative phase and intensity of the individual emitters.[33,34] This finding implies that the waveguide system acts as an ultra-compact and branchless Mach–Zehnder interferometer. To investigate this phenomenon, we fabricated an asymmetric system consisting of a waveguide with 150 nm and 300 nm slot width. The difference Δn in the mode effective index introduces a relative modal phase shift of $\Delta\varphi = \Delta n \cdot L$, where L is the length of the waveguide system. The simulated phase evolution mapped in Fig. 6a and b for a 15.63 μm and a 7.81 μm long structure shows a 2π and π phase difference, respectively. We illustrate perfect constructive and destructive by measuring the transmission of the individual systems. Although the constructive interfering system is much longer, it shows a much higher transmission than the shorter system, where the signal emitted from the antennas are overlapping and destructively interfering in the far-field. It is noteworthy, that unequal losses in the individual waveguides and differences in coupling efficiencies can potentially be compensated by adjusting the beam position. Here, the maximum of the Gaussian beam is still positioned nearly the center of the in-coupling nanoantenna pair but the transmitted intensity is maximized for the in-phase or minimized for the out-of-phase configuration, respectively, by slightly shifting the relative beam position from the antenna pairs centroid point. Based on this capability, a high extinction ratio of 18.3 dB is observed. This value is in good agreement with the expected extinction ration of 20 dB estimated by calculating the far-field interference pattern produced by two separated point-like dipole emitters under consideration of the unequal structure lengths and the finite acceptance angle of the used microscope objective. As shown in Fig. 6c, the resulting far-field interference of the in-phase radiating antennas yield in an intensity distribution mainly directed toward the normal direction. However, assuming two dipoles oscillating out-of-phase, the wavefronts cancel towards the normal direction due to destructive inference, while showing the first-order maxima emitting at large angles, barely detectable by the used high NA objective.

Conclusion

Summarizing, we have proposed and investigated, theoretically and experimentally, a branchless waveguide configuration that allows the simultaneous coherent excitation of two plasmonic slot waveguide modes. The subwavelength separated parallel slot waveguides fed by ultra-compact nanoantennas show a reasonably large in-coupling efficiency without significant cross-talk between the two individual slot waveguides. This system is utilized to realize a novel ultra-compact Mach–Zehnder interferometer without a requirement for on-chip waveguide branching, making this system to be a very compact solution for sensing applications. Besides the miniaturization capabilities, another advantage of our design is the lateral accessibility of the metal pads forming this interferometric system. The proposed configuration allows one to seamlessly introduce electrical contacts for electro-optic modulation akin to that what has been demonstrated[12,13] and/or amorphous germanium for on-chip detection.[35] This unique attribute makes it a promising candidate for integrated plasmonic electro-optic applications.

Conflicts of interest

There are no conflicts of interest to declare.

Acknowledgements

References

1 E. Ozbay, *Science*, 2006, **311**, 189–193.

2 S. A. Maier, *Plasmonics: Fundamentals and Applications*, Springer, 2007.

3 D. K. Gramotnev and S. I. Bozhevolnyi, *Nat. Photonics*, 2010, **4**, 83–91.

4 T. J. Davis, D. E. Gómez and A. Roberts, *Nanophotonics*, 2016, **6**, 543–559.

5 Z. Fang and X. Zhu, *Adv. Mater.*, 2013, **25**, 3840–3856.

6 Y. Fang and M. Sun, *Light: Sci. Appl.*, 2015, **4**, e294.

7 Z. Han and S. I. Bozhevolnyi, *Rep. Prog. Phys.*, 2013, **76**, 016402.

8 M. Großmann, M. Thomaschewski, A. Klick, A. Goszczak, E. Sobolewska, T. Leißner, J. Adam, J. Fiutowski, H.-G. Rubahn and M. Bauer, *Plasmonics*, 2017, 1–8.

9 W. Cai, W. Shin, S. Fan and M. L. Brongersma, *Adv. Mater.*, 2010, **22**, 5120–5124.

10 C. L. Smith, N. Stenger, A. Kristensen, A. N. Mortensen and S. I. Bozhevolnyi, *Nanoscale*, 2015, **7**, 9355–9386.

11 M. Cohen, Z. Zalevsky and R. Shavit, *Nanoscale*, 2013, **5**, 5442–5449.

12 C. Haffner, W. Heni, Y. Fedoryshyn, J. Niegemann, A. Melikyan, D. Elder, B. Baeuerle, Y. Salamin, A. Josten, U. Koch, C. Hoessbacher, F. Ducry, L. Juchli, A. Emboras, D. Hillerkuss, M. Kohl, L. Dalton, C. Hafner and J. Leuthold, *Nat. Photonics*, 2015, **9**, 525–528.

13 M. Ayata, Y. Fedoryshyn, W. Heni, B. Baeuerle, A. Josten, M. Zahner, U. Koch, Y. Salamin, C. Hoessbacher, C. Haffner, D. L. Elder, L. R. Dalton and J. Leuthold, *Science*, 2017, **358**, 630–632.

14 D. Ansell, I. Radko, Z. Han, F. Rodriguez, S. Bozhevolnyi and A. Grigorenko, *Nat. Commun.*, 2015, **6**, 8846.

15 Y. Ding, X. Guan, X. Zhu, H. Hu, S. Bozhevolnyi, L. Oxenløwe, K. Jin, N. Mortensen and S. Xiao, *Nanoscale*, 2017, **9**, 15576–15581.

16 J. Chen, C. Sun, H. Li and Q. Gong, *Nanoscale*, 2014, **6**, 13487–13493.

17 Y. Yang, Q. Li and M. Qiu, *Sci. Rep.*, 2016, **6**, 19490.

18 S. Lal, S. Link and N. J. Halas, *Nat. Photonics*, 2007, **1**, 641–648.

19 J. Homola, *Chem. Rev.*, 2008, **108**, 462–493.

20 J. N. Anker, P. W. Hall, O. Lyandres, N. C. Shah, J. Zhao and R. P. Duyne, *Nat. Mater.*, 2008, **7**, 442–453.

21 S. Kumar, A. Huck and U. L. Andersen, *Nano Lett.*, 2013, **13**, 1221–1225.

22 X. Wu, P. Jiang, G. Razinskas, Y. Huo, H. Zhang, M. Kamp, A. Rastelli, O. G. Schmidt, B. Hecht, K. Lindfors and M. Lippitz, *Nano Lett.*, 2017, **17**, 4291–4296.

23 R. W. Heeres, L. P. Kouwenhoven and V. Zwiller, *Nat. Nanotechnol.*, 2013, **8**, 719–722.

24 K. C. Huang, M.-K. Seo, T. Sarmiento, Y. Huo, J. S. Harris and M. L. Brongersma, *Nat. Photonics*, 2014, **8**, 244–249.

25 C. Rewitz, G. Razinskas, P. Geisler, E. Krauss, S. Goetz, M. Pawłowska, B. Hecht and T. Brixner, *Phys. Rev. Appl.*, 2014, **1**, 014007.

26 A. Kriesch, S. P. Burgos, D. Ploss, H. Pfeifer, H. A. Atwater and U. Peschel, *Nano Lett.*, 2013, **13**, 4539–4545.

27 S. P. Burgos, H. W. Lee, E. Feigenbaum, R. M. Briggs and H. A. Atwater, *Nano Lett.*, 2014, **14**, 3284–3292.

28 H. W. Lee, G. Papadakis, S. P. Burgos, K. Chander, A. Kriesch, R. Pala, U. Peschel and H. A. Atwater, *Nano Lett.*, 2014, **14**, 6463–6468.

29 A. Andryieuski, R. Malureanu, G. Biagi, T. Holmgaard and A. Lavrinenko, *Opt. Lett.*, 2012, **37**, 1124.

30 Lumerical Inc. http://www.lumerical.com/tcad-products/fdtd/.

31 P. Johnson and R. Christy, *Phys. Rev. B: Solid State*, 1972, **6**, 4370–4379.

32 G. Veronis and S. Fan, *Opt. Express*, 2008, **16**, 2129–2140.

33 D. Wolf, T. Schumacher and M. Lippitz, *Nat. Commun.*, 2016, **7**, 10361.

34 C. Ropp, Z. Cummins, S. Nah, J. T. Fourkas, B. Shapiro and E. Waks, *Nat. Commun.*, 2015, **6**, 6558.

35 Y. Salamin, P. Ma, B. Baeuerle, A. Emboras, Y. Fedoryshyn, W. Heni, B. Cheng, A. Josten and J. Leuthold, *ACS Photonics*, 2018, DOI: 10.1021/acsphotonics.8b00525.

Appendix B

On-Chip Detection of Optical Spin-Orbit Interactions in Plasmonic Nanocircuits

NANO LETTERS

On-Chip Detection of Optical Spin−Orbit Interactions in Plasmonic Nanocircuits

Martin Thomaschewski,*[ID] Yuanqing Yang,*[ID] Christian Wolff, Alexander S. Roberts,[ID]
and Sergey I. Bozhevolnyi[ID]

Centre for Nano Optics, University of Southern Denmark, Campusvej 55, DK-5230 Odense M, Denmark

[S] *Supporting Information*

ABSTRACT: On-chip manipulating and controlling the temporal and spatial evolution of light are of crucial importance for information processing in future planar integrated nanophotonics. The spin and orbital angular momentum of light, which can be treated independently in classical macroscopic geometrical optics, appear to be coupled on subwavelength scales. We use spin−orbit interactions in a plasmonic achiral nanocoupler to unidirectionally excite surface plasmon polariton modes propagating in seamlessly integrated plasmonic slot waveguides. The spin-dependent flow of light in the proposed nanophotonic circuit allows on-chip electrical detection of the spin state of incident photons by integrating two germanium-based plasmonic-waveguide photodetectors. Consequently, our device serves as a compact ($\sim 6 \times 18 \ \mu m^2$) electrical sensor for photonic spin Hall dynamics. The demonstrated configuration opens new avenues for developing highly integrated polarization-controlled optical devices that would exploit the spin-degree of freedom for manipulating and controlling subwavelength optical modes in nanophotonic systems.

KEYWORDS: *Surface plasmon polaritons, slot waveguides, spin−orbit interaction, photodetection, photonic spin Hall effect*
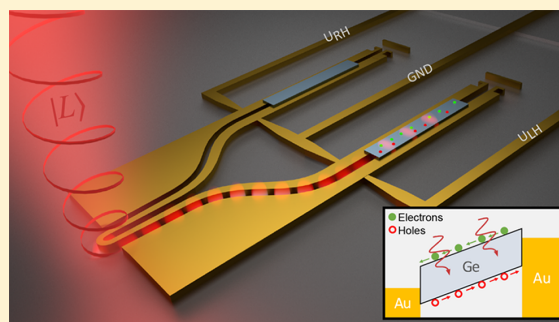
Light carries both the spin, an intrinsic form of angular momentum, and orbital angular momentum, which determines its polarization and spatial degree of freedom. Interaction between the spin and orbital degrees of freedom of photons has evoked intensive investigations owing to its potential to push the development of technologies, such as chiroptical spectroscopy,[1−3] communication,[4,5] information processing,[6] optomechanics,[7] topological photonics,[8,9] and quantum computing,[10,11] to their full potential. The limiting factor for groundbreaking developments in those fields refers to the fact that the spin−orbit interactions (SOIs) in optics are usually very weak, akin to electron SOIs found in solid-state spintronics.[12] A promising way to significantly enhance spin-controlled optical phenomena is to utilize light-matter interactions on the nanoscale that are especially strong in plasmonic nanostructures.[13−17] It has been shown that geometrically chiral metallic structures, which do not superimpose onto their mirror image, can strongly enhance chiroptical responses as a consequence of structural chirality.[18−22] Remarkably, even achiral structures exhibit the potential of SOIs in the near-field due to twisted trajectories of surface plasmons at a nanosphere.[23−26] This feature enables spin-controlled local manipulation within one nanoscale coupler, which responds equally to both photonic spin states. We utilize the strong SOI in an achiral plasmonic nanostructure to demonstrate for the first time on-chip

detection of spin-controlled directional routing in a compact plasmonic nanocircuit. We find that a subwavelength semiring can launch gap surface plasmons supported by seamlessly integrated plasmonic slot waveguides preferentially in one direction, depending on the spin state of locally incident radiation. This spin-dependent phenomenon can thus be regarded as a manifestation of the quantum spin Hall effect (QSHE) of light.[13,14,27] We bridge the fields of integrated photonics and electronics, progressing toward what has repeatedly been highlighted as the key perspective of plasmonics,[28−33] by integrating two germanium-based plasmonic photodetectors for on-chip electrical read-out of unidirectional surface plasmon polariton (SPP) excitation. We show that nonchiral optical responses, which are inherently dependent on the linear polarization degree, can be quantitatively identified and discriminated based on synchronous differential photocurrent detection, providing a signal directly proportional to the S_3 Stokes parameter of locally incident radiation. Our proposed device is thus capable of detecting the chirality of light in ultracompact dimensions, which is generally difficult to realize using conventional optics. In addition, the same structure offers the ability of identifying

linear polarization states, making it particularly interesting for fast polarimetric imaging.

Results and Discussion. Figure 1 schematically shows the proposed plasmonic device, which provides the features
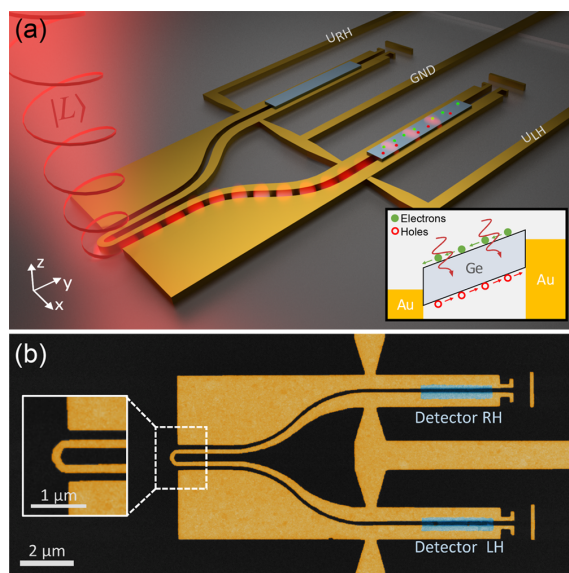
Figure 1. Schematics and design of the proposed device utilized for on-chip electrical detection of spin-controlled unidirectional plasmonic waveguiding. (a) Three-dimensional rendering illustrates exemplarily for a left circular polarized incident beam the spin-selective unidirectional routing in the plasmonic nanocircuit. The propagating waveguide mode is reaching the plasmonic MSM photodetector consisting of a Au–Ge–Au heterostructure in which electron–hole pairs are generated and subsequently collected by an externally applied reverse bias. Inset: energy band diagram of the Au/Ge/Au heterojunction MSM photodetector under bias. (b) Colorized scanning electron microscopy image showing the top view of a plasmonic device. The Ge region (azure color) embedded in the plasmonic slot waveguide forming the plasmonic detector can be readily observed in the SEM image.

mentioned above. It comprises an achiral gold semiring waveguide coupler with a width of 150 nm and a radius of curvature of 225 nm in which normally incident, focused light is preferably exciting SPPs in one of the two seamlessly integrated gold metal–isolator–metal (MIM) slot waveguides due to SOI. The excited propagating mode is strongly confined in the subdiffractional waveguide slots, which have sizes of $w \times h = 150 \times 100$ nm^2. The entire device is covered with a 300 nm thick dielectric layer (PMMA, $n_{PMMA} = 1.48$) to reduce mode leakage into the underlying SiO$_2$ substrate. To prevent adiabatic coupling between the two slot waveguides, we separate the channels along the SPPs propagation direction. Using this design, plasmonic photodetectors are integrated by locally filling the slot with germanium (Ge) semiconductor material in each individual branch. The strongly confined SPP mode is absorbed by the Ge material and the generated electron–hole pairs are collected by an external electric field. The inset in Figure 1a provides a schematic representation of the energy band diagram of the Au–Ge–Au heterostructure while the detector is biased with an externally applied voltage, which attracts the carriers toward the metal contacts. The

electrodes of the plasmonic photodetector are naturally integrated by the metal that supports the propagation of the corresponding SPP mode. For interfacing the electrical nanocircuit to macroscopic electrodes, three connecting wires are embedded, allowing for independent operation of two detectors by individual bias electrodes with respect to a common ground. In this way, fabrication imperfections that might result in unequal photoresponses of the detectors and/or unequal propagation losses within the two waveguide branches can be easily compensated by a single adjustment of the reverse bias that defines the carrier extraction efficiency of each individual detector. Consequently, the entire device allows for differential photocurrent measurements of two plasmonic photodetectors, which directly reveal accurate information about the spin state of the locally incident beam. Fabrication details of the proposed device are given in Methods.

In order to study the SOI in our device, we first focus on the interaction of incident radiation with the semiring coupler. Therefore, we validate numerically the spin-sorting functionality by utilizing finite difference time-domain (FDTD) simulations, considering that the modeled geometry is illuminated with a diffraction-limited beam ($\lambda_0 = 1550$ nm). We clearly see in Figure 2a that under left-circular polarization
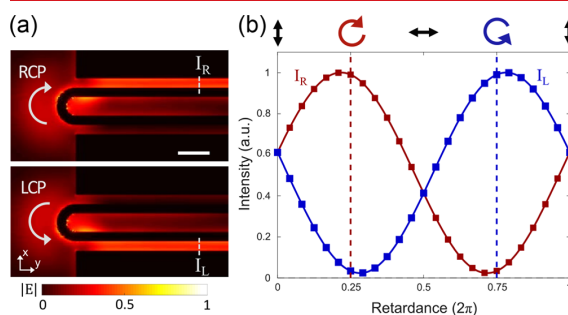
Figure 2. Nanoscale directional coupler enabling selective far-field excitation of two plasmonic slot waveguides by spin–orbit interaction. (a) Simulated near-field intensity distribution for excitation with LHC and RHC input polarization demonstrating routing to the left and right branch, respectively. The scale bar represents 500 nm. (b) Output intensities of the two channels at continuously varying retardation between the polarization axis perpendicular and parallel to the waveguide axis. The 0 and 2π retardance corresponds to linear polarization perpendicular to the waveguides axis, while π corresponds to linear polarization parallel to the waveguide. In-between, circular polarized light with opposite spin is present.

(LCP) and right-circular polarization (RCP) illumination, the field is concentrated on one side of the looped wire, respectively, and the excited plasmons stay strongly localized at the corresponding waveguide resulting in unidirectional power flow. The origin of the unidirectional excitation can thus be understood by consideration of the twisted near-field evolution within the nanocoupler.[23−26] The spin of the incident photon interacts with the inherent transverse spin of the SPP as an evanescent wave propagating along the outer edge of the semiring. The handedness of the evanescent tail self-determines the direction of the excited edge mode feeding the corresponding seamlessly integrated slot waveguide. While the majority of the incident light is coupled into one particular waveguide, a small fraction of optical power is directed into the

opposite waveguide, leading to a calculated directionality contrast of ~14.5 dB (for the considered configuration). A parametric study of the semiring geometry for optimized performance at the targeted wavelength of λ_0 = 1550 nm can be found in Supporting Information S2 including a study of the robustness on fabrication inaccuracies and non-normal incidence of the beam. To gain a deeper insight into the excitation mechanisms governing the Poynting vector flow, the directed power in the individual channels is studied for various polarizations ranging from linear to circular with intermediate elliptical polarization states (see Figure 2b). We observe that any linear polarization excites both waveguides equally due to equal contributions from LCP and RCP. However, the total power flow is enhanced at a linear polarization perpendicular to the waveguide. This observation indicates that the system exhibits a nonchiral excitation mechanism, which couples light simultaneously into both slot waveguides once the polarization coincides with the antisymmetric slot waveguide modes.[34] As the power flow is governed by two independent coupling mechanisms, the maximum of the directed intensity appears at elliptical polarization, slightly shifted from circularly polarized states toward vertical linear polarizations.

With the above numerical simulations establishing the framework for spin-selective unidirectional excitation, we now move on to the experimental realization of the on-chip device for spin-selective routing. For this purpose, we first conduct an all-optical far-field characterization of the device before plasmonic photodetectors are integrated (see Figure 3). A diffraction-limited beam with wavelength λ_0 = 1550 nm and controlled polarization is positioned onto the coupler section of the device at normal incidence. By adjusting the retardance of a Soleil-Babinet compensator, we generated a beam with LCP and RCP. Light scattering from the impedance-matched nanoantennas is observed in reflection mode for both polarization states (Figure 3b,c). The emission intensities at the impedance-matched nanoantennas reveal that the plasmonic modes generated by photons with opposite spin are efficiently directed to different waveguide branches.

After experimentally verifying the predicted spin-sorting functionality of the device, plasmonic photodetectors are integrated for the realization of full on-chip detection. Therefore, an additional lithography step was carried out to define the plasmonic detector region. Consequently, the plasmonic slot waveguide is locally filled with amorphous Ge semiconductor material by thermal evaporation. To substantiate the electrical detection of plasmons in the plasmonic slot waveguide, we comprehensively characterize the plasmonic photodetector in a simplified system from the same fabrication batch, consisting of a straight plasmonic slot waveguide equipped with plasmonic nanoantennas as shown in Figure 4. The spatial and polarization dependence of the measured photocurrent (Figure 4a−d) clearly reveals on-chip detection of the propagating slot waveguide mode, which is efficiently excited once the beam is positioned at the coupling nanoantenna port with a polarization angle that coincides with the long axis of the plasmonic coupling antenna arms. The launched plasmonic mode propagates toward the detector and penetrates the 4 μm long metal−semiconductor−metal (MSM) region. The SPPs are absorbed in the semiconductor material generating electron−hole pairs which are efficiently separated by an externally applied electric field $E \sim U/w$ in the slot with the applied bias voltage U and detected as photoinduced current (Figure 4e). Internal quantum efficien-
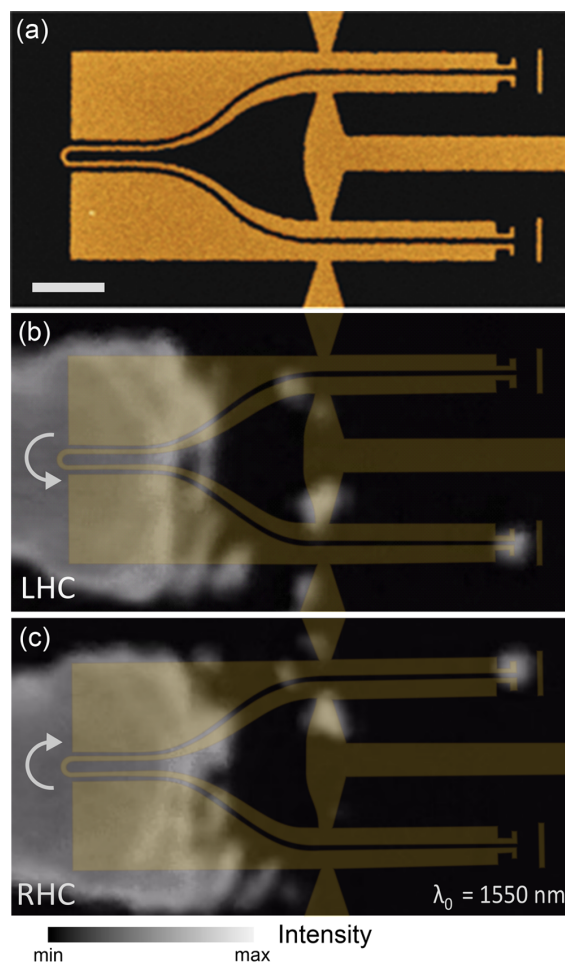
Figure 3. All-optical experimental demonstration of spin-sorting in the proposed plasmonic nanocircuit. (a) Colorized scanning electron microscopy image of the device before germanium-based photodetectors are integrated. The scale bars represent 2 μm. (b,c) The scattering images for excitation with opposite circular polarizations are superimposed with the device configuration. The integration time of the camera is adjusted to give a reasonable contrast for the output signal, leading to an oversaturation and increase in size of the incident beam spot. The appearance of the far-field scattering signal at different out-coupling antennas reveals that photons with opposite spin are efficiently directed into opposite waveguide branches.

cies (IQE) exceeding 1% are demonstrated for the individual detector at the targeted wavelength of 1550 nm (Figure 4f). For investigating the dynamic behavior of the detector, we modulate the laser intensity and measured the photocurrent response. A flat frequency response over operation frequencies from 100 Hz to 60 kHz is observed. The measured −3 dB bandwidth of 95 kHz is based on the limited response time of the used signal amplifiers. However, the presented plasmonic photodetector is expected to provide high-speed operation (>100 GHz) due to a small RC product and the short transit time of the photogenerated carriers.[31]

For the electrical detection of spin-selective routing in our proposed device, we positioned the beam on the chiral coupler section of the plasmonic circuit integrated with two Au−Ge−
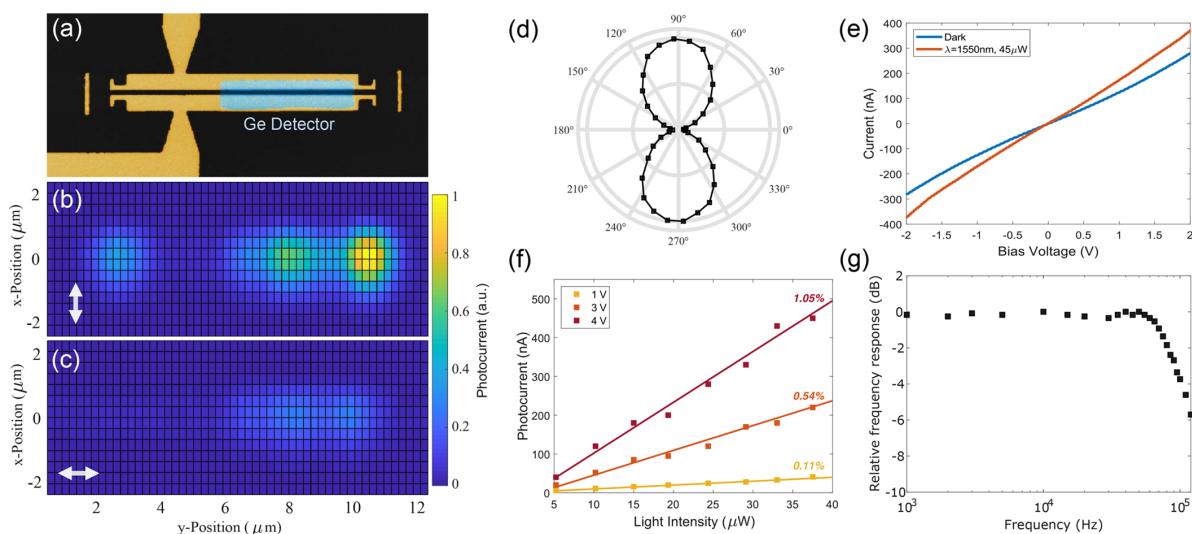
Figure 4. Full characterization of the plasmonic photodetector at a wavelength of $\lambda_0 = 1550$ nm. (a) Colorized SEM image of the device used for the detector characterization. (b,c) Two-dimensional photocurrent maps obtained by raster scanning the incident Gaussian beam with vertical and horizontal polarization, respectively. (d) Polar plot of the measured photocurrent as a function of the polarization angle of the incident beam positioned at the left coupling antenna. (e) Measured $I-U$-characteristic at bias voltages between 0 and ± 2 V under dark and illumination condition. (f) Generated photocurrent as a function of the light power in the waveguide before entering the detector. (g) Frequency response measurements of the detector show a -3 dB bandwidth of 90 kHz, which originates from the limited response time of the used signal amplifier.
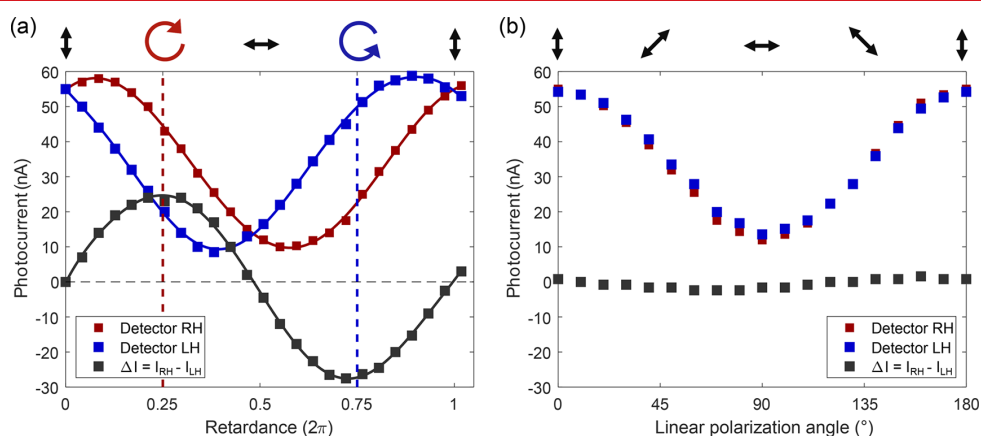
Figure 5. Measured photocurrents of the individual photodetectors with the differential signal for various polarizations. Error bars are in the order of data point size. (a) A Soleil–Babinet variable phase retarder is used to convert linearly polarized laser radiation into left and right circularly polarized states with intermediate elliptical and an orthogonal linear polarization state. The measured photocurrents reveal that the SOI process in our device is contributing to a spin-controlled unidirectional coupling process, resulting in unbalanced photocurrents in the two detectors. The differential photocurrent signal can directly be translated to the handedness and helicity of the incident beam. (b) A half-wave plate is used to measure the photocurrents for linearly polarized light at different polarization angles. A near-zero signal in the differential photocurrent signal substantiates that directionality in our device is exclusively induced by SOI.

Au detectors, one on each individual waveguide branch, as shown in Figure 1. The photocurrents of the individual photodetectors are measured for various polarization states of the incident beam. Figure 5 shows measured photocurrents with its differential signal, where the polarization angle, ellipticity, and handedness of the incident beam is continuously varied. It is seen that the SOI process in our device is directly translating the spin-controlled contribution to the coupling process into unbalanced photocurrents of the two detectors. In contrast, any linear polarization state shows no directionality due to a symmetric optical coupling process,

resulting in a near-zero signal in the differential photocurrent measurement (Figure 5b). This reveals the fact that directionality in our device is exclusively induced by SOI. Considering nonlinear states of polarization, our device has the crucial feature of providing a differential photocurrent signal which can be directly translated to the handedness and helicity of the incident beam, while being virtually insensitive to linearly polarized light (Figure 5a). Nonchiral optical effects inherently cancel out so that the sign of the corresponding signal displays the handedness and the absolute value its helicity. The directionality appears with nonresonant charac-

teristics which enables broadband operation (see Supporting Information, Figure S4). Comparing the absolute photocurrent evolutions of the individual detectors with the numerical investigation in Figure 3 indicates that nonchiral excitation mechanisms are more pronounced in the experiment than predicted by simulation. We believe that this discrepancy is associated with fabrication imperfections and surface roughness in the semiring and waveguides which serves potentially as inherent waveguide coupler due to diffraction on roughness features.

Conclusion. In summary, using SOI in an achiral semiring, on-chip electrical detection of spin-selective directional routing in a plasmonic nanocircuit has been demonstrated successfully. This study may open new routes in highly integrated plasmonic nanocircuits that include the spin degree of freedom for manipulating the optical power flow, in analogy to electron spintronics. Our proposed device not only enables spin-controlled tunable addressing of two plasmonic waveguide channels for spin-encoded communication applications but also serves as a compact polarimeter capable of determining the one-axis linear polarization state, helicity, and handedness of locally incident radiation. The device can be extended by waveguide channels that are sensitive to linear polarization along one of the ±45° axes with respect to the symmetry axis of the device, which enables a complete on-chip characterization of the polarization state. Our approach thus opens new perspectives in highly integrated nanophotonic circuits by combining strong light-matter interactions in plasmonics with semiconductor technology for future polarization encoded communication interfaces. Taken together, we believe this study further bridges the remarkable capability of nanophotonic manipulation in plasmonics with nanoscale electronic systems.

Methods. *Fabrication.* The fabrication of the device relies on a multistep lithographic process using the mix-and-match technique for lithographic overlay. First, bonding pads and connecting electrodes are patterned onto a glass chip by optical lithography, metal deposition (5 nm Ti/50 nm Au), and lift-off. The plasmonic circuits are written by electron-beam lithography (EBL) at an acceleration voltage of 30 keV in 300 nm PMMA resist and 20 nm thick Al layer to prevent charge accumulation. The alignment between the different lithography steps is performed manually using markers. After development, the circuits are formulated by depositing a 5 nm titanium adhesion layer and 100 nm gold by thermal evaporation and subsequent 12 h lift-off in acetone. For the optical characterization, a 300 nm PMMA cladding was spin-coated on the chip to reduce mode leakage into the glass substrate. The same PMMA layer serves as an electron beam resist for the last EBL step, which integrates the germanium photodetectors onto the plasmonic circuit by evaporating 2 nm Ti and 110 nm Ge onto the predefined region. The germanium material is evaporated in a sufficiently outgassed tungsten boat to prevent impurities during deposition. Finally, a 300 nm thin layer of PMMA is deposited. For electrical connection, the chip is wire bonded on a printed circuit board equipped with two on-board amplifiers.

Numerical Simulations. FDTD simulations were performed using a commercial software (FDTD Solutions v8.11.318, Lumerical). Perfectly matched layers were applied to enclose the computational domain of 3 μm × 4.5 μm × 2 μm in all calculations. A finely mesh grid size of 10 nm is used in the simulations. The optical constants of the gold were taken from

the experimental data reported by Johnson and Christy.[35] For circular polarization excitation, we employed two coherent Gaussian sources with the same intensity but orthogonal polarizations with a phase retardance of 90°. The diameter of the Gaussian beam was set to a 2 μm. To determine the coupled light into each waveguide, we integrated the time-averaged Poynting vector over the slot gap area at 3 μm away from the antenna coupler.

■ **ASSOCIATED CONTENT**

Ⓢ Supporting Information

The Supporting Information is available free of charge on the ACS Publications website at DOI: 10.1021/acs.nano-lett.8b04611.

Optical setup for the electrical detection of spin-selective routing, FDTD study of the geometric parameters of the semiring and its response under non-normal incidence, details on the detector characterization, wavelength dependence of the device (PDF)

■ **AUTHOR INFORMATION**

Corresponding Authors
*E-mail: math@mci.sdu.dk.
*E-mail: yy@mci.sdu.dk.

ORCID ⊚
Martin Thomaschewski: 0000-0003-2545-1468
Yuanqing Yang: 0000-0001-7139-1254
Alexander S. Roberts: 0000-0003-2608-6327
Sergey I. Bozhevolnyi: 0000-0002-0393-4859

Author Contributions
Y.Y. conceived the idea and performed the simulation. Y.Y. and M.T. designed the final device structure. M.T. set up the experiment and performed the device fabrication and experimental measurements. C.W. and A.S.R assisted in the experimental measurements. All authors contributed to the interpretation of the results. M.T. wrote the manuscript with contributions from all other authors. S.I.B. supervised the project.

Notes
The authors declare no competing financial interest.

■ **REFERENCES**

(1) Greenfield, N. J. *Nat. Protoc.* **2007**, *1*, 2876−2890.
(2) Schreiber, R.; Luong, N.; Fan, Z.; Kuzyk, A.; Nickels, P. C.; Zhang, T.; Smith, D. M.; Yurke, B.; Kuang, W.; Govorov, A. O.; Liedl, T. *Nat. Commun.* **2013**, *4*, 2948.
(3) Smith, K. W.; McCarthy, L. A.; Alabastri, A.; Bursi, L.; Chang, W.; Nordlander, P.; Link, S. *ACS Nano* **2018**, *12*, 11657−11663.
(4) Thidé, B.; Then, H.; Sjöholm, J.; Palmer, K.; Bergman, J.; Carozzi, T.; Istomin, Y. N.; Ibragimov, N.; Khamitova, R. *Phys. Rev. Lett.* **2007**, *99*, No. 087701.
(5) Farshchi, R.; Ramsteiner, M.; Herfort, J.; Tahraoui, A.; Grahn, H. T. *Appl. Phys. Lett.* **2011**, *98*, 162508.

(6) Gramotnev, D. K.; Bozhevolnyi, S. I. *Nat. Photonics* **2010**, *4*, 83−91.

(7) Magallanes, H.; Brasselet, E. *Nat. Photonics* **2018**, *12*, 461−464.

(8) Lu, L.; Joannopoulos, J. D.; Soljačić, M. *Nat. Photonics* **2014**, *8*, 821−829.

(9) Khanikaev, A. B.; Mousavi, H. S.; Tse, W.-K.; Kargarian, M.; MacDonald, A. H.; Shvets, G. *Nat. Mater.* **2013**, *12*, 233−239.

(10) Gao, W.; Imamoglu, A.; Bernien, H.; Hanson, R. *Nat. Photonics* **2015**, *9*, 363−373.

(11) Lodahl, P.; Mahmoodian, S.; Stobbe, S.; Rauschenbeutel, A.; Schneewiss, P.; Volz, J.; Pichler, H.; Zoller, P. *Nature* **2017**, *541*, 473−480.

(12) Wolf, S.; Awschalom, D.; Buhrman, R.; Daughton, J.; von Molnár, S.; Roukes, M.; Chtchelkanova, A.; Treger, D. *Science* **2001**, *294*, 1488−1495.

(13) Bliokh, K. Y.; Smirnova, D.; Nori, F. *Science* **2015**, *348*, 1448−1451.

(14) Bliokh, K.; Rodríguez-Fortuño, F.; Nori, F.; Zayats, A. *Nat. Photonics* **2015**, *9*, 796−808.

(15) Schaferling, M.; Yin, X.; Giessen, H. *Opt. Express* **2012**, *20*, 26326−26336.

(16) Poulikakos, L. V.; Thureja, P.; Stollmann, A.; Leo, E.; Norris, D. J. *Nano Lett.* **2018**, *18*, 4633−4640.

(17) O'Connor, D.; Ginzburg, P.; Rodríguez-Fortuño, F.; Wurtz, G.; Zayats, A. *Nat. Commun.* **2014**, *5*, 5327.

(18) Li, Z.; Li, Y.; Han, T.; Wang, X.; Yu, Y.; Tay, B.; Liu, Z.; Fang, Z. *ACS Nano* **2017**, *11*, 1165−1171.

(19) Frank, B.; Yin, X.; Schäferling, M.; Zhao, J.; Hein, S. M.; Braun, P. V.; Giessen, H. *ACS Nano* **2013**, *7*, 6321−6329.

(20) Gansel, J. K.; Thiel, M.; Rill, M. S.; Decker, M.; Bade, K.; Saile, V.; von Freymann, G.; Linden, S.; Wegener, M. *Science* **2009**, *325*, 1513−1515.

(21) Zubritskaya, I.; Maccaferri, N.; Ezeiza, X.; Vavassori, P.; Dmitriev, A. *Nano Lett.* **2018**, *18*, 302−307.

(22) Li, W.; Coppens, Z. J.; Besteiro, L. V.; Wang, W.; Govorov, A. O.; Valentine, J. *Nat. Commun.* **2015**, *6*, 8379.

(23) Pan, D.; Wei, H.; Gao, L.; Xu, H. *Phys. Rev. Lett.* **2016**, *117*, 166803.

(24) Lefier, Y.; Grosjean, T. *Opt. Lett.* **2015**, *40*, 2890−2893.

(25) Bliokh, K. Y.; Gorodetski, Y.; Kleiner, V.; Hasman, E. *Phys. Rev. Lett.* **2008**, *101*, No. 030404.

(26) Lefier, Y.; Salut, R.; Suarez, M.; Grosjean, T. *Nano Lett.* **2018**, *18*, 38−42.

(27) Yin, X.; Ye, Z.; Rho, J.; Wang, Y.; Zhang, X. *Science* **2013**, *339*, 1405−1407.

(28) Haffner, C.; Heni, W.; Fedoryshyn, Y.; Niegemann, J.; Melikyan, A.; Elder, D.; Baeuerle, B.; Salamin, Y.; Josten, A.; Koch, U.; et al. *Nat. Photonics* **2015**, *9*, 525−528.

(29) Haffner, C.; Chelladurai, D.; Fedoryshyn, Y.; Josten, A.; Baeuerle, B.; Heni, W.; Watanabe, T.; Cui, T.; Cheng, B.; Saha, S.; et al. *Nature* **2018**, *556*, 483−486.

(30) Du, W.; Wang, T.; Chu, H.-S.; Nijhuis, C. A. *Nat. Photonics* **2017**, *11*, 623−627.

(31) Salamin, Y.; Ma, P.; Baeuerle, B.; Emboras, A.; Fedoryshyn, Y.; Heni, W.; Cheng, B.; Josten, A.; Leuthold, J. *ACS Photonics* **2018**, *5*, 3291−3297.

(32) Afshinmanesh, F.; White, J. S.; Cai, W.; Brongersma, M. L. *Nanophotonics* **2012**, *1*, 125−129.

(33) Ebbesen, T. W.; Genet, C.; Bozhevolnyi, S. I. *Phys. Today* **2008**, *61*, 44−50.

(34) Thomaschewski, M.; Yang, Y.; Bozhevolnyi, S. I. *Nanoscale* **2018**, *10*, 16178−16183.

(35) Johnson, P.; Christy, R. *Phys. Rev. B* **1972**, *6*, 4370−4379.

Supporting Information for

On-chip Detection of Optical Spin-Orbit Interactions

in Plasmonic Nanocircuits

Martin Thomaschewski,* Yuanqing Yang,* Christian Wolff, Alexander S. Roberts, and Sergey I. Bozhevolnyi

Center for Nano Optics, University of Southern Denmark, Campusvej 55, DK-5230 Odense M,

Denmark

*Corresponding Authors: math@mci.sdu.dk, yy@mci.sdu.dk

S1: Optical setup for the electrical detection of spin-selective routing
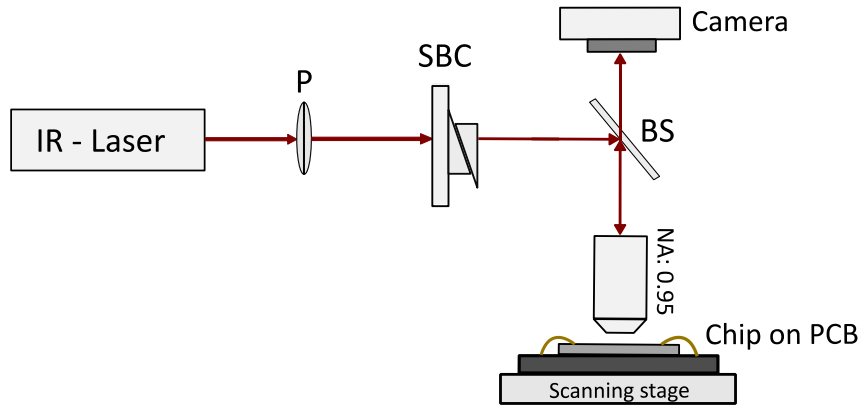
Figure S1 Schematic of the setup used for on-chip detection of spin-selective routing in the plasmonic nanocircuit. The linearly polarized light beam from a wavelength tunable IR laser is used as an illumination source. After passing a polarizer (P) and a Soleil-Babinet variable phase retarder (SBC), the laser beam is focused on the sample surface at normal incidence with an IR-objective (×100 magnification, NA = 0.95), resulting in a FWHM beam size of $\Theta = (2.3\pm0.2)$ μm. The chip is wire bonded on a printed circuit board equipped with two operational amplifiers for individual extraction of photocurrents at independent bias voltages with respect to a common ground.

S2: FDTD study of the geometric parameters of the semiring and its response under non-normal incidence

S2.1: Design optimization of the semiring coupler
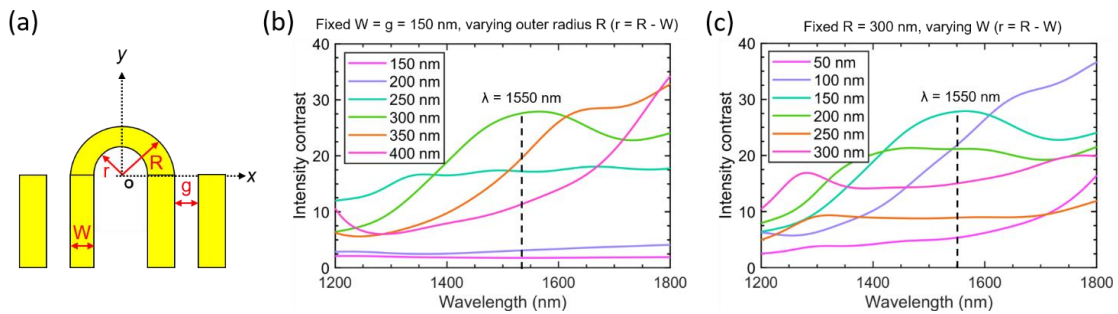
Figure S2.1. 3D-FDTD parametric optimization study of the proposed spin-selective semiring coupler for maximum intensity contrast between the two waveguide channels at the targeted wavelength of $\lambda_0 = 1550$ nm. The intensity contrast is defined as I_L / I_R at LCP light. (a) Top view of the modelled geometry with the width W of the semiring, its inner radius r and outer radius R and the waveguide slot width g. (b) Varying the outer radius R while keeping the semiring width and slot width fixed at 150 nm indicates a local maximum in the intensity contrast at the wavelength of 1550 nm for R = 300 nm. (c) Varying the semiring width W while keeping the outer radius R fixed at 300 nm reveals the optimal width of W = 150 nm. Due to the non-resonant characteristics of the coupling mechanism, broadband functionality is observed in the numerical study.

S2.2: Influence of the angle of incidence on the spin-sorting functionality
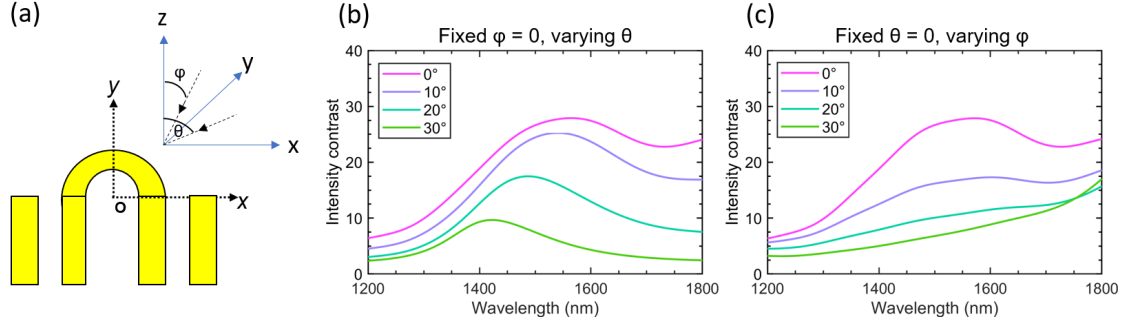
Figure S2.2 3D-FDTD study of the influence of the angle of incidence on the spin-sorting functionality. The spin-selective coupling mechanism is shown to be robust against non-normal incidence of the beam within 10° tilt to the normal axis and thus ensuring functionality. (a) The angle θ is defined as the incident angle in the x-z plane and the angle φ as the incident angle in the y-z plane. (b) By sweeping the incident angle θ we observe a decrease on the intensity contrast between the two waveguide channels accompanied with a blueshift of the maximum intensity contrast with larger angles. (c) Tilt of the incident beam along the y-z plane is shown to have stronger influence on the intensity contrast.

S3: Details on the detector characterization

The IQE relies on the ratio of the generated charge carriers to the absorbed power in the photodetector section of our device. Introducing the power in the plasmonic device before entering the on-chip detector, P_{WG}, in the device shown in Figure 4a, the IQE can be calculated by

$$\text{IQE} \; = \; 100 \; \cdot \left(\frac{I_{ph}}{P_{WG} \cdot \lambda_0} \right) \cdot \left(\frac{h \cdot c}{e} \right),$$

where I_{ph} is the measured photocurrent, λ_0 is the free-space wavelength, h is the Planck constant and c and e are the speed of light and the elementary charge. We estimated experimentally the coupling efficiency of the impedance-matched plasmonic nanoantenna to be (9 ± 1) %. Due to fabrication imperfections, this value is lower than the coupling efficiency of 12.1% calculated using FDTD. The propagation length is calculated to be 9.5 µm. By placing the incident beam with known power precisely onto the left coupling antenna in Figure 4a, we can estimate the absolute power coupled into the waveguide and the intensity decay during the mode propagation towards the detector. The power P_{WG} before entering the detector is considered (in the IQE estimation above) to be fully absorbed in the Ge volume and consequently contributing to the charge carrier generation in the semiconductor. However, due to the mode index mismatch between the SPP propagating in the Au-PMMA-Au waveguide ($n_{eff,PMMAWG}$=1.67 + 0.013i) and the mode in the Au-Ge-Au photodetector section ($n_{eff,GeWG}$ = 2.64 + 0.31i), the SPPs exhibit strong back-reflections at the PMMA/Ge interface. Using FDTD, we estimate the reflection at the PMMA/Ge interface by calculating the electric field

$$E \; = \; E_0 e^{-ikx} + r e^{-i\theta} \cdot E_0 e^{-ikL} \cdot E_0 e^{-ik(L-x)}, \qquad \text{(Eq. S1)}$$

along the Au/PMMA/Au slot waveguide induced by the forward (1st term) and backward propagating mode (2nd term) with $k = 2\pi n_{eff}/\lambda$. The reflectance $R = |r|^2$ is estimated by fitting Eq. (S1) to the calculated electric field along the waveguide (See Fig. S3(b)). We obtain a theoretical reflectance of R = 25 %. By investigating

the far-field optical images of the device while the beam is positioned at the coupling antenna, we observe diffuse scattering at the detector interfaces and the out-coupling antenna. This indicates that a significant portion of light reaching the detector is not absorbed in the semiconductor material and is thus not contributing to any charge carrier generation. Consequently, scattering and reflections within the device lead to an underestimation of the determined IQE of the plasmonic photodetector and gives prospects for future studies to clarify parasitic effects of the all-plasmonic device including further design optimization (e.g. by mode index matching).
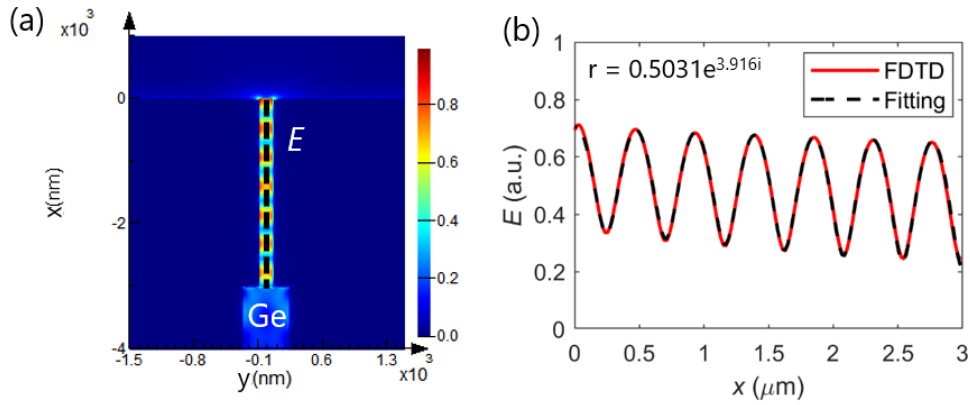
Figure S3 The electric field induced by the forward and backward propagating mode is calculated using FDTD simulations. The geometry in the simulation corresponds to the geometry of the experimentally investigated structure shown in Figure 4. (a) Top-view of the calculated electric field. The dashed black line indicates the position of the extracted field profile shown in (b) for the extraction of the reflectance R by fitting Eq. (S1) to the obtained profile.

S4: Wavelength dependence of the device
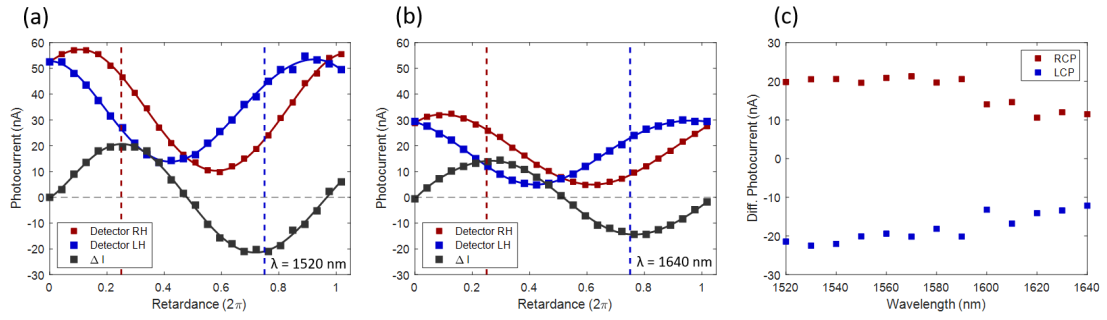
Figure S4 Wavelength dependence of the device. To demonstrate broadband functionality, we measured the photocurrents for different incident wavelengths. Electrical on-chip detection of spin-selective directional routing in the plasmonic nanocircuit is shown in (a) and (b) for the incident wavelength $\lambda_0 = 1520$ nm and $\lambda_0 = 1640$ nm, respectively. The extracted differential photocurrents at LCP and RCP are shown in (c) for the wavelength range of 1520 nm to 1640 nm. The observed decay of the photocurrent at longer wavelengths relies on less efficient light absorption of Ge at this wavelength range.

Appendix C

Plasmonic monolithic lithium niobate directional coupler switches
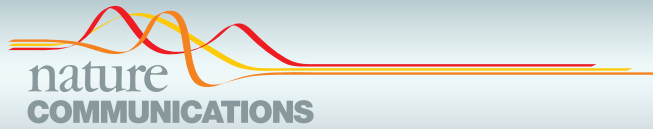
ARTICLE

Plasmonic monolithic lithium niobate directional coupler switches

Martin Thomaschewski [1*], Vladimir A. Zenin [1], Christian Wolff [1] & Sergey I. Bozhevolnyi [1*]

Lithium niobate (LN) has been the material of choice for electro-optic modulators owing to its excellent physical properties. While conventional LN electro-optic modulators continue to be the workhorse of the modern optoelectronics, they are becoming progressively too bulky, expensive, and power-hungry to fully serve the needs of this industry. Here, we demonstrate plasmonic electro-optic directional coupler switches consisting of two closely spaced nm-thin gold nanostripes on LN substrates that guide both coupled electromagnetic modes and electrical signals that control their coupling, thereby enabling ultra-compact switching and modulation functionalities. Extreme confinement and good spatial overlap of both slow-plasmon modes and electrostatic fields created by the nanostripes allow us to achieve a 90% modulation depth with 20-µm-long switches characterized by a broadband electro-optic modulation efficiency of 0.3 V cm. Our monolithic LN plasmonic platform enables a wide range of cost-effective optical communication applications that demand µm-scale footprints, ultrafast operation and high environmental stability.

[1] Centre for Nano Optics, University of Southern Denmark, Campusvej 55, DK-5230 Odense M, Denmark. *email: math@mci.sdu.dk; seib@mci.sdu.dk

In the last decades, lithium niobate has become indispensable for integrated photonics as the material of choice for electro-optic modulation due to its excellent (linear and nonlinear) optical and material properties. Being advantageous over competing platforms, lithium niobate (LN) fulfills the eligibility material requirements for optical communication systems by exhibiting wide optical transparency (0.35–4.5 µm), large electro-optic coefficients ($r_{33} = 30$ pm V^{-1}), which are preserved at elevated temperatures due to its high Curie temperature (~1200 °C), and excellent chemical and mechanical stability resulting in long-term material reliability[1]. Leading to considerable commercial significance, the early success of LN for optoelectronic applications was driven by heterogeneous integration of metal-diffused channel optical waveguides utilized for chip-scale electro-optic modulators[2–7]. However, the weak confinement of integrated metal-diffused optical waveguides is limiting the electro-optic interaction, resulting in low electro-optic modulation efficiencies and large device footprints. Recently, monolithic integration of thin-film lithium niobate modulators[8–14] has attracted an increasing attention due to significantly higher optical confinement, leading to improvements in terms of compactness, bandwidth and energy efficiency, while still demanding relatively long, on the mm-scale, interaction lengths due to conceptual limitations in the electro-optic field overlap.

Leveraging metal nanostructures to transmit simultaneously both optical and electrical signals, with the additional attribute of extremely enhancing their accompanied local fields, promises plasmonics to become a versatile platform for exceptionally compact optoelectronic applications[15,16]. The first pioneering work[17] utilizing surface plasmon polaritons (SPPs) for electrically controlled modulation was based on thermo-optic effects induced by resistive heating in polymer materials. Though this approach facilitates only moderate switching times and relatively high power consumption, the large overlap between the electromagnetic field of the plasmonic mode and the electrically induced local change of the refractive index was opening the path to exceptionally efficient plasmonic electro-optic modulators. Following this approach, tremendous efforts have been directed towards exploring other electro-optic material platforms, which drastically improved the switching performance, including two-dimensional materials[18–21], phase-change materials[22–24], and electro-optic polymers[25–31]. These studies convincingly demonstrated the capability of plasmonics to be a potential complementary technology addressing bottleneck issues in future information technology. However, combining the attractive features of plasmonics with LN[32], to date still the preferred material platform meeting all essential performance requirements, has remained largely unexplored.

Here, we introduce a monolithic plasmonic modulator/switch configuration based on two identical gold nanostripes on LN, where the metallic structure utilized for applying external electrostatic fields inherently supports the propagation of the SPP modes, resulting in an exceptionally simple device architecture. Our approach does not require patterning, etching or milling of the LN substrate, which is particularly challenging due to its mechanical hardness and chemical stability. The antisymmetric change of the refractive index of LN due to the Pockels electro-optic effect induced by an external electric field applied across two gold nanostripes affects the optical coupling between the plasmonic modes propagating along the two nanostripes. This allows high-density integration with extraordinary efficient and broadband switching of the optical power distribution (at telecom wavelengths) between the two output ports of plasmonic directional couplers.

Results

Device principles. The proposed optical switch configuration represents a plasmonic directional coupler that comprises two
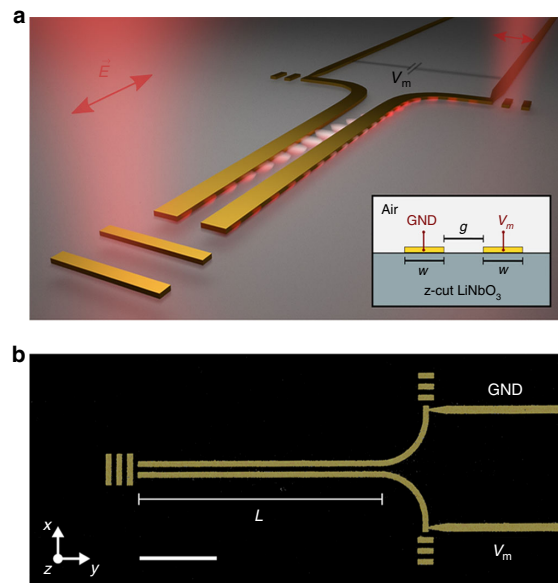
Fig. 1 Plasmonic monolithic lithium niobate directional coupler switch. a Conceptual image of power modulation in the plasmonic nanostripes by applying a bias voltage, which induces a refractive index change due to the electro-optic effect in the substrate. The inset shows the cross-section of the two identical parallel waveguides of width $w = 350$ nm, separated by a gap of $g = 350$ nm and placed on z-cut lithium niobate (LiNbO$_3$, LN). **b** False-colored scanning electron microscope (SEM) image of the investigated plasmonic directional coupler switch. The scale bar represents 5 µm. The optimal length L of interaction is chosen to be 15.5 µm.

lithographically fabricated gold nanostripe waveguides placed on z-cut LN, which have identical dimensions of $w \times h = 350 \times 50$ nm^2 and are separated by the distance of 350 nm (Fig. 1). Numerical optimization of the waveguide dimensions is given in Supplementary Note 5.

The transmission line, composed of two optically coupled plasmonic strip waveguides, supports two quasi-TEM modes, i.e., the odd and even modes, which define the geometrically dependent coupling length $L_C = \pi / |\beta_{odd} - \beta_{even}| = \lambda_0 / (2 \cdot |n_{odd} - n_{even}|)$ of the passive system with the mode effective indices n_{odd} and n_{even}, respectively. An optical near-field study is conducted to verify and quantify coupling between the two SPP modes supported by the considered configuration (Supplementary Note 9 and Supplementary Movie 1). In the modulator device, light with the free-space wavelength λ_0 is fed symmetrically into the two plasmonic waveguides by positioning a diffraction-limited beam on a metallic grating coupler. A 90° bend of the individual waveguides in opposite directions is employed to separate the coupling channels and accordingly limiting the interaction length L between the SPP modes supported by the nanostripe waveguides. Furthermore, the linearly polarized emission from the terminating gratings is rotated by the bend to be orthogonal to the polarization of the incident beam, thus allowing cross-polarized far-field imaging with suppression of back-reflections from the incident beam. In order to introduce an external electrostatic field in the electro-optically active substrate supporting the plasmonic coupler, the individual waveguide ends are electrically connected to signal (V_m) and ground (GND), respectively. The change of the refractive index induced by the Pockels effect in z-cut LN depends on the direction of the applied electric field relative to the direction of the optic axis

ARTICLE
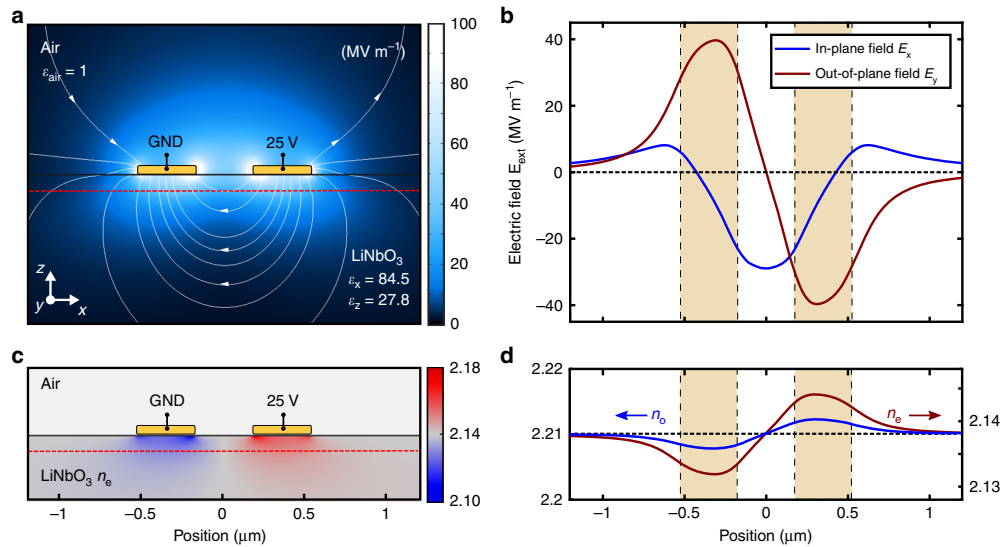
Fig. 2 Electrostatic field simulation of the two-wire configuration. a Color-coded electric field and its contours upon applying a bias of 25 V. The electrostatic field extends stronger along the depth-direction (z-axis), as compared to the isotropic case, due to the anisotropy in the relative permittivity of z-cut lithium niobate (LiNbO$_3$, LN). **b** In-plane (E_x) and out-of-plane electric-field component (E_z) in the LN substrate 100 nm below the surface (along the dashed red line shown in Fig. 2a). The yellow bars indicate the position of the Au wires. The in-plane field component E_x shows highest amplitude in between the two electrodes, while the out-of-plane component E_z exhibits highest amplitude underneath the wires with opposite sign. **c, d** Due to the linear electro-optic (Pockels) effect in the LN substrate, the extraordinary (n_e) and ordinary (n_o) refractive index underneath the left wire is decreased, while being increased by an equal amount in the right guide. Consequently, the waveguides lose their optical identity, which influences the power transfer in the directional coupler.

of the crystal. To investigate the optical response on the externally applied field, the electrostatic field distribution with the field contour lines are simulated for the two-wire configuration while one wire is grounded and the other is biased with 25 V (Fig. 2).

The field extends further along the depth-direction as compared to the isotropic case due to the anisotropic relative permittivity of LN. The amplitude of the electric field components along the x- and z- direction 100 nm below the LN/air interface (Fig. 2b) reveals an alternating electric field along the LN optical axis below the individual nanostripes.

Therefore, an opposite refractive index modification is introduced in the two waveguides, consequently eliminating the device symmetry of the directional coupler (Fig. 2c, d). Strong overlap between the plasmonic field and the modulating electrostatic field results in a significant phase change with opposite polarities in the two waveguides, thus providing efficient push-pull operation of the directional coupler modulator. An expression for the intensity modulation and switching characteristics of the device can be derived from the coupled-mode formalism[33]. Under assumption of negligible coupling in the output bends and by neglecting absorption losses, the normalized power in the weakly coupled waveguide system is given by (see Supplementary Note 1):

$$P_{1,2} = \frac{1}{2}\left[1 \pm \frac{2}{\Delta\beta_n + \Delta\beta_n^{-1}}\sin^2\left(\frac{\pi}{2}\frac{L}{L_C}\sqrt{1 + \Delta\beta_n^2}\right)\right], \quad (1)$$

where $\Delta\beta_n = [\beta_1(V_m) - \beta_2(V_m)]/[\beta_{odd}(V_m = 0) - \beta_{even}(V_m = 0)]$ is the normalized electrically induced difference in the propagation constants β_1 and β_2 of each individual waveguide mode, and L is the interaction length. From Eq. (1) it follows that the unbiased device is inherently set to the linear section of the modulation transfer curve (quadrature point), offering high degree of linearity and collapse of

even-order nonlinear distortions in the modulation spectrum. It is clear that complete switching of the optical power can be reached when the device length is $L = L_C/\sqrt{2}$ and when $\Delta\beta_n = 1$ (i.e., the required voltage should cause the difference in propagation constants of each wire to be as high as the difference between mode propagation constants of the even and odd modes in the passive device). Deviations from this interaction length result in reduced maximum modulation depth and sensitivity (see Supplementary Note 1 and 2 for details). It was found that for the considered cross-section geometry of the directional coupler, this condition is fulfilled at the interaction length of $L = 15.5\,\mu m$ and thus taken as the optimum design for efficient switching in our study. Interestingly, the above conditions for the complete switching demonstrate the well-known trade-off between required voltage and device length: with less coupled waveguides, the required full-switch voltage will be smaller, but the optimal interaction length will be larger. Due to the established material platform and the simple device geometry, the fabrication procedure of the monolithic modulator device is exceedingly simple, involving only a standard electron-beam lithography step followed by thermal gold evaporation and subsequent metal lift-off (see Methods for more details). Furthermore, the switch conceptionally exhibits relaxed tolerances to geometrical variations and wavelength instabilities compared to ring resonators or Mach-Zehnder interferometers (see Supplementary Note 3–5 for details).

Performance of the device. Switching and modulation of the scattering signal emitted from the output gratings of the two waveguide channels in the characterized device is illustrated with far-field images shown in Fig. 3 for two different bias voltages with opposite polarity.

At zero bias, the symmetry of the device configuration results in an equal phase condition in the coupler arms and consequently

3
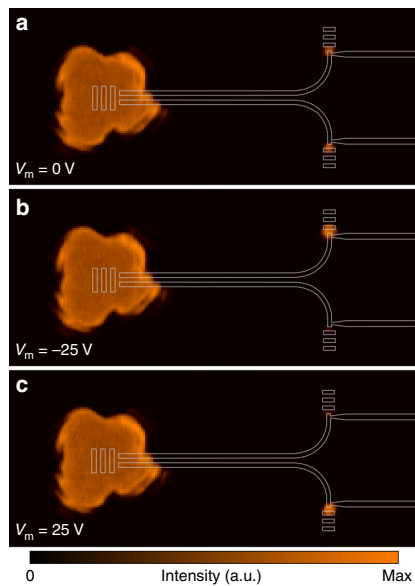
Fig. 3 Visualization of switching and modulation behavior. Experimental optical far-field images captured by an infrared camera at different modulation voltages. A diffraction-limited beam ($\lambda_0 = 1550$ nm) is positioned on the input grating to symmetrically feed the coupling system. The structure design is superimposed as a guide to the eye. The scattering images are superimposed with the structure design. **a** The unbiased device ($V_m = 0$ V) exhibits equal power distribution of the scattered signal emitted from the output ports, due to the symmetry of the directional coupler. **b** When a negative bias voltage ($V_m = -25$ V) is applied, an enhancement of the optical output signal of the biased waveguide arm is observed, while the optical signal at the opposite output port is decreased in intensity. **c** By changing the polarity of the applied voltage, the intensity in the two output terminals is switched.

equal power distribution in the waveguides, revealed by balanced output signals. When a bias signal is applied, an enhancement of the output signal at one port is observed, while the signal at the opposite output port is decreased. By changing the polarity of the applied voltage, the intensity in the two output terminals is switched, revealing a reversed refractive index change as expected from the linear modulation characteristics of the Pockels effect. The dynamic optical switching, induced by an alternating voltage of $V_{AC} = 25$ V at slow switching speeds, is captured by the infrared camera (Supplementary Movie 2).

For obtaining the transfer curve in Fig. 4a, the applied bias is varied and the output power modulation of the two channels is measured independently at the image plane by spatial filtering with subsequent detection by a photodiode (see the "Methods" section for more details). The experimentally measured modulation curve agrees well with the analytical predictions from the coupled mode theory (CMT), assisted by finite element method (FEM) simulations (see the "Methods" section for details). A modulation depth of 90% is achieved at sufficiently high voltages ($V \approx \pm 50$ V), without permanent breakdown of the device. This corresponds to a dual-channel intensity extinction ratio (ER) of 10 dB. Given that the full modulation depth is reached at the electrically induced phase mismatch of $\sqrt{2}\pi$, our device exhibits a drive voltage-length product of 0.3 V cm (half-wave voltage-length product of $V_\pi L = 0.21$ V · cm), which is approximately an order of magnitude smaller than that obtained with the

state-of-the-art photonic LN modulators. In fact, lower levels of the voltage-length product have only been observed with electro-optic polymers, whose very low phase-transition temperatures impede their practical deployment (see Supplementary Table 2 for a detailed comparison). The insertion loss due to the propagation loss of $\alpha = 0.35$ dB μm^{-1} in the phase shifter section is 5.5 dB, resulting in a half-wave voltage-length-loss product of $V_\pi L \alpha = 735$ VdB. Due to non-resonant modulation characteristics and the wide optical transparency window, spectrally broadband operation of our directional coupler switch is expected. The relative modulation efficiency at the driving voltage of 15 V is measured within the wavelength range of 1280–1590 nm (Fig. 4b), normalized by that measured at the design wavelength of 1550 nm. Although the performance of the device fluctuates with the operation wavelength, a high wavelength tolerance is observed, exhibiting <2 dB modulation depth variation within all wavelength telecommunication bands.

The electro-optic frequency response of the directional coupler switch is characterized from 10 kHz to 10 GHz (Fig. 4c). The device exhibits a flat frequency response up to 2 GHz in our measurement. The observed 3-dB bandwidth of (9 ± 2) GHz is caused by a limited response bandwidth of the electrical feedline on the chip and the RF probes (see Supplementary Note 8 for details). Owing to the extremely short response time ($\sim$ fs) of the Pockels effect and the small device capacitance of only 3.6 fF, the calculated modulation cutoff frequency exceeds 800 GHz at 50 Ω resistive load ($f = 1/[2\pi RC]$), indicating potential operation at much higher modulation speeds than shown in our measurements and suggesting the energy consumption reaching levels below 1 pJ/bit (see Supplementary Note 6 for details).

Discussion

In summary, we demonstrated a broadband directional coupler switch featuring a drive voltage-length product of 0.3 V cm at telecom wavelengths, to date the lowest value for a device based on lithium niobate electro-optic modulation. Owing to the excellent material properties such as electro-optic reliability and temperature stability, this material platform is still considered as the material-of-choice that can fulfill the demands of future optical data links, by exploring new device configurations which are significantly smaller, faster, and more efficient than current LN electro-optic modulators. The proposed directional coupler switch configuration addresses this challenge with exceptional structural simplicity by providing multiport, broadband, and effective modulation at a compact footprint and a high-speed operation. The presented proof-of-concept study of utilizing integrated plasmonic circuits in LN platforms demonstrates its enormous potential, which can pave the way towards feasible communication links, promising high-speed, broadband, and robust operation. The full-switching voltage in our configuration can be reduced by utilizing plasmonic waveguides with higher optical confinement or longer interaction length, which can eventually be interfaced with low-loss photonic waveguides or multicore fibers[26] for practical integration into long-haul on-chip optical communication systems.

Methods

Device fabrication. Devices are fabricated on commercially available *z*-cut lithium niobate substrates. The directional coupler modulators are written by electron beam lithography (using a scanning electron microscope JOEL JSM-6490LV with an acceleration voltage of 30 keV) in spin-coated 200-nm-thick PMMA positive resist and 20-nm-thick Al layer, which serves as a metallic charge dissipation layer during the writing (electron doses varying between 200 and 250 μC cm^{-2}). After resist development, the directional couplers are formed by depositing a 4 nm titanium adhesion layer and a 50 nm gold layer by thermal evaporation and subsequent 12 h lift-off in acetone. To reduce electron beam writing time, macroscopic bonding pads and connecting wires are patterned beforehand on the LN chip by

ARTICLE
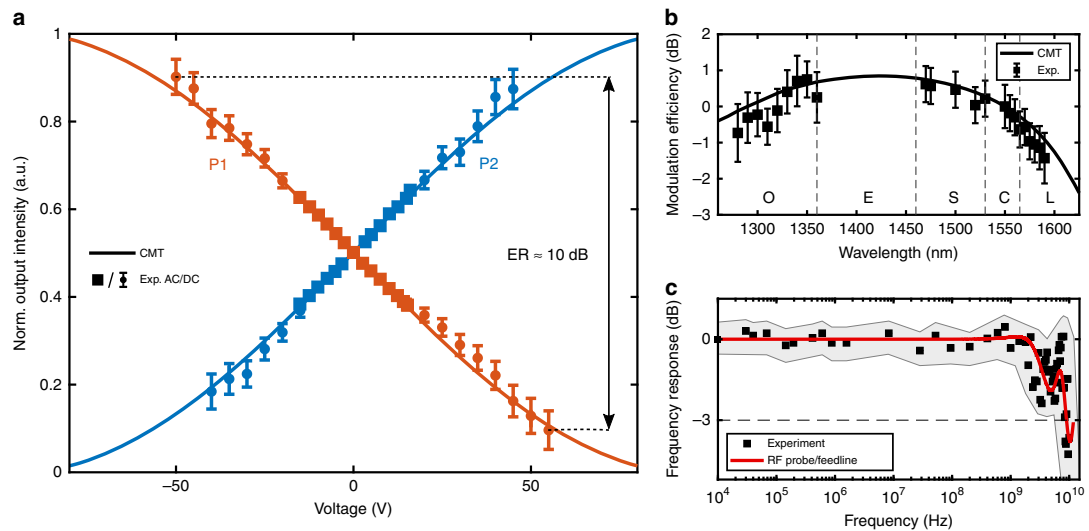
Fig. 4 Directional coupler switch characteristics. a Measured (symbols) and simulated (solid lines) electro-optical transfer function, showing the power exchange as a function of the applied bias voltage. Error bars represent standard deviations and are deduced from repeated measurements. For AC signals smaller than 15 V (with a frequency of 200 kHz), error bars are smaller than the symbols. **b** Wavelength dependence of the modulation efficiency (at the driving voltage of 15 V) normalized by that measured at the design wavelength of 1550 nm. Less than 2 dB modulation deterioration over all optical communication wavelength bands is observed. Error bars indicate the estimated standard deviation of the mean. **c** Measured frequency response as a function of the applied RF signal frequency, normalized with respect to the lowest applied frequency. The continuous shaded error region represents the standard deviation in the measured frequency response with a smoothed average between data points. The response in the measured frequency range is only restricted by the bandwidth limitations of the RF probe and the electrical feedline (red line).

optical lithography, metal deposition (5 nm Ti/150 nm Au), and lift-off. Lithographic overlay is ensured by the mix-and-match approach.

Experimental electro-optical characterization. A collimated and linearly polarized laser beam from a tunable IR laser is focused by a high numerical aperture objective (Olympus MPlan100xIR, NA = 0.95). The focused beam is positioned symmetrically on the grating coupler for symmetric feeding of the two arms of the directional coupler. The output optical signal is collected by the same objective. The cross-polarized configuration is used to suppress the back-reflection and scattering from the incident beam. This provides an improved signal-to-noise ratio for the optical signal scattered from the output gratings, which is subsequently detected by the IR camera or a high-speed photodiode. The integration time of the camera is adjusted to give a reasonable contrast for the output signal, leading to an over-saturation and increased size of the incident back-reflected beam spot. By applying electrical probes on the electrode pads, one directional coupler arm is grounded while the other is biased with an AC/DC signal. For measuring the modulation transfer curve, the wavelength dependence and the frequency response of the device, the scattering signal coming from one port of the directional coupler is spatially filtered and detected by a high-speed photodetector. The frequency response measurements are calibrated by the response reference of the signal generator and the photoreceiver. A detailed description of the experimental set-up can be found in Supplementary Note 7 and 8.

Numerical modeling. FEM simulations are performed using a commercially available software (Comsol Multiphysics 5.2a). For the electrostatic simulations, the device cross-section is modeled with the unclamped static relative permittivity tensor of LN taken from Jazbinsek et al.[34] ($\varepsilon_{xx} = \varepsilon_{yy} = 27.8$, $\varepsilon_{zz} = 84.5$), while the relative permittivity of air is set to be $\varepsilon_{air} = 1$ and the boundaries of the two gold nanostripes are set to ground and V_{bias} potential, respectively. The calculated electric-field distribution is utilized to determine the modification of the refractive index in the LN substrate by using the electro-optic Pockels coefficients from Jazbinsek et al.[34] (restricting to the largest diagonal terms, i.e., $\Delta n_{ii} = -0.5 r_{iiz} n_{ii}^3 E_z$, with $r_{xxz} = r_{yyz} = 10.12$ pm/V and $r_{zzz} = 31.45$ pm V^{-1}), which are considered to be non-dispersive over the investigated wavelength range[35]. For the optical simulation, the modified distribution of the refractive index of LN is fed into the mode solver, while the unmodified refractive indices from Au and LN were taken from Johnson and Christy[36] and Zelmon et al.[37] ($n_{xx} = n_{yy} = n_o = 2.211$, $n_{zz} = n_e = 2.138$ at $\lambda_0 = 1550$ nm). Scattering-boundary conditions in combination with a perfectly matched layer are applied to calculate the modification $\beta_1 - \beta_2$ in the propagation constants of each individual waveguide as a function of the applied

voltage, which is used for describing the intensity modulation using the coupled-mode formalism (see Supplementary Note 1 for details). The optical simulation of two parallel waveguides and unmodified LN refractive index was used to calculate the propagation constants of even and odd modes (β_{even} and β_{odd}) and, eventually, the coupling length L_C.

Data availability
All data that support the findings of this study are available from the corresponding authors upon reasonable request.

References
1. Weis, R. & Gaylord, T. Lithium niobate: summary of physical properties and crystal structure. *Appl. Phys. A* **37**, 191–203 (1985).
2. Alferness, R. Polarization-independent optical directional coupler switch using weighted coupling. *Appl. Phys. Lett.* **35**, 748–750 (1979).
3. Bozhevolnyi, S. I., Buritskii, K. S., Zolotov, E. M., Prokhorov, A. M. & Chernykh, V. A. A study of an electrooptic modulator utilizing coupled channel diffused waveguides in LiNbO₃. *Kvantovaya Elektro.* **9**, 1808–1816 (1982).
4. Schmidt, R. & Kaminow, I. Metal-diffused optical waveguides in LiNbO₃. *Appl. Phys. Lett.* **25**, 458–460 (1974).
5. Wooten, E. L. et al. A review of lithium niobate modulators for fiber-optic communications systems. *IEEE. J. Sel. Top. Quantum Electron.* **6**, 69–82 (2000).
6. Tavlykaev, R. F. & Ramaswamy, R. V. Highly linear Y-fed directional coupler modulator with low intermodulation distortion. *J. Lightwave Technol.* **17**, 282–291 (1999).
7. Anwar, N. et al. The effect of fabrication parameters on a Ridge Mach–Zehnder interferometric (MZI) modulator. *J. Lightwave Technol.* **20**, 854–861 (2002).
8. Ren, T. et al. An integrated low-voltage broadband lithium niobate phase modulator. *IEEE Photon. Technol. Lett.* **31**, 889–892 (2019).

ARTICLE

9.   Wang, C., Zhang, M., Stern, B., Lipson, M. & Lončar, M. Nanophotonic lithium niobate electro-optic modulators. *Opt. Express* **26**, 1547–1555 (2018).
10. He, M. et al. High-performance hybrid silicon and lithium niobate Mach–Zehnder modulators for 100 Gbit s−1 and beyond. *Nat. Photonics* **13**, 359–364 (2019).
11. Wang, C. et al. Integrated lithium niobate electro-optic modulators operating at CMOS-compatible voltages. *Nature* **562**, 101–104 (2018).
12. Boes, A., Corcoran, B., Chang, L., Bowers, J. & Mitchell, A. Status and potential of lithium niobate on insulator (LNOI) for photonic integrated circuits. *Laser Photonics Rev.* **12**, 1700256 (2018).
13. Rao, A. & Fathpour, S. Compact lithium niobate electrooptic modulators. *IEEE J. Sel. Top. Quantum Electron.* **24**, 1–14 (2018).
14. Mahmoud, M., Cai, L., Bottenfield, C. & Piazza, G. Lithium niobate electro-optic racetrack modulator etched in Y-Cut LNOI platform. *IEEE Photonics J.* **10**, 1–10 (2018).
15. Ebbesen, T. W., Genet, C. & Bozhevolnyi, S. I. Surface-plasmon circuitry. *Phys. Today* **61**, 44–50 (2008).
16. Thomaschewski, M., Yang, Y., Wolff, C., Roberts, A. & Bozhevolnyi, S. I. On-chip detection of optical spin-orbit interactions in plasmonic nanocircuits. *Nano Lett.* **19**, 1166–1171 (2019).
17. Nikolajsen, T., Leosson, K. & Bozhevolnyi, S. I. Surface plasmon polariton based modulators and switches operating at telecom wavelengths. *Appl. Phys. Lett.* **85**, 5833–5835 (2004).
18. Maier, M., Nemilentsau, A., Low, T. & Luskin, M. Ultracompact amplitude modulator by coupling hyperbolic polaritons over a graphene-covered gap. *ACS Photonics* **5**, 544–551 (2018).
19. Ding, Y. et al. Efficient electro-optic modulation in low-loss graphene-plasmonic slot waveguides. *Nanoscale* **9**, 15576–15581 (2017).
20. Ansell, D. et al. Hybrid graphene plasmonic waveguide modulators. *Nat. Commun.* **6**, 8846 (2015).
21. Thomas, P. et al. Nanomechanical electro-optical modulator based on atomic heterostructures. *Nat. Commun.* **7**, 13590 (2016).
22. Joushaghani, A. et al. Sub-volt broadband hybrid plasmonic-vanadium dioxide switches. *Appl. Phys. Lett.* **102**, 061101 (2013).
23. Markov, P. et al. Optically monitored electrical switching in VO2. *ACS Photonics* **2**, 1175–1182 (2015).
24. Rudé, M., Simpson, R. E., Quidant, R., Pruneri, V. & Renger, J. Active control of surface plasmon waveguides with a phase change material. *ACS Photonics* **2**, 669–674 (2015).
25. Haffner, C. et al. Low-loss plasmon-assisted electro-optic modulator. *Nature* **556**, 483–486 (2018).
26. Ayata, M. et al. High-speed plasmonic modulator in a single metal layer. *Science* **358**, 630–632 (2017).
27. Kieninger, C. et al. Ultra-high electro-optic activity demonstrated in a silicon-organic hybrid modulator. *Optica* **5**, 739–748 (2018).
28. Abel, S. et al. Large Pockels effect in micro- and nanostructured barium titanate integrated on silicon. *Nat. Materials* **18**, 42–47 (2019).
29. Haffner, C. et al. All-plasmonic Mach–Zehnder modulator enabling optical high-speed communication at the microscale. *Nat. Photonics* **9**, 525–528 (2015).
30. Heni, W. et al. Plasmonic IQ modulators with attojoule per bit electrical energy consumption. *Nat. Commun.* **10**, 1694 (2019).
31. Alloatti, L. et al. 100 GHz silicon–organic hybrid modulator. *Light Sci. Appl.* **3**, e173 (2014).
32. Berini, P., Charbonneau, R., Jeté-Charbonneau, S., Lahoud, N. & Mattiussi, G. Long-range surface plasmon-polariton waveguides and devices in lithium niobate. *J. Appl. Phys.* **101**, 113114 (2007).
33. Yariv, A. Coupled-mode theory for guided-wave optics. *IEEE J. Quantum Elect.* **9**, 919–933 (1973).
34. Jazbinšek, M. & Zgonik, M. Material tensor parameters of LiNbO3 relevant for electro- and elasto-optics. *Appl. Phys. B* **74**, 407–414 (2002).
35. Yonekura, K., Jin, L. & Takizawa, K. Measurement of dispersion of effective electro-optic coefficients r_{13}^E and r_{13}^E of non-doped congruent LiNbO3 crystal. *Jpn. J. Appl. Phys.* **47**, 7R (2008).
36. Johnson, P. & Christy, R. Optical constants of the noble metals. *Phys. Rev. B* **6**, 4370–4379 (1972).
37. Zelmon, D. E., Small, D. L. & Jundt, D. Infrared corrected Sellmeier coefficients for congruently grown lithium niobate and 5 mol% magnesium oxide–doped lithium niobate. *J. Opt. Soc. Am. B* **14**, 3319–3322 (1997).

Author contributions
S.I.B. and M.T. conceived the experiment and geometry of the modulators. M.T. set up the experiment, performed the device fabrication, experimental characterization and simulations of the device. V.Z. and C.W. contributed in the device characterization and simulations. M.T. wrote the manuscript with contributions from all other authors. S.I.B. supervised the project.

Competing interests
The authors declare no competing interests.

Additional information
Supplementary information is available for this paper at https://doi.org/10.1038/s41467-020-14539-y.

Correspondence and requests for materials should be addressed to M.T. or S.I.B.

Peer review information *Nature Communications* thanks Young-Ik Sohn, Luke Sweatlock and the other, anonymous, reviewer(s) for their contribution to the peer review of this work. Peer reviewer reports are available.

Reprints and permission information is available at http://www.nature.com/reprints

Publisher's note Springer Nature remains neutral with regard to jurisdictional claims in published maps and institutional affiliations.

Supplementary Information

Plasmonic monolithic lithium niobate directional coupler switches

Thomaschewski et al.

Supplementary Note 1: Coupled mode formalism

The evolution of a wave (mode), propagating along y-axis with the propagation constant of β, can be described as following (here for the electromagnetic wave):

$$\{\mathbf{E}(x,y,z), \mathbf{H}(x,y,z)\} = \{\mathbf{E}(x,z), \mathbf{H}(x,z)\} C\exp(j\beta y) \tag{1.1}$$

When there are two non-interacting waveguides, each carrying a single mode with a complex-valued amplitude of C_1 and C_2, respectively, the total field can be written in a similar form:

$$\{\mathbf{E}(x,y,z), \mathbf{H}(x,y,z)\} = \{\mathbf{E_1}(x,z), \mathbf{H_1}(x,z)\} C_1 \exp(j\beta_1 y) + \{\mathbf{E_2}(x,z), \mathbf{H_2}(x,z)\} C_2 \exp(j\beta_2 y) \tag{1.2}$$

This should be understood as following: the fields in the area of the first waveguides are described only with the first term (i.e., the field from the second mode does not reach this area), and the second term describes the fields in the area of the second waveguide. However, when waveguides are brought together, there is non-zero overlap between their modes, therefore they couple, i.e., the power transfers from one mode into the other. If the coupling is relatively weak, one can still use the above equation 1.2, but with the assumption that the mode amplitudes C_1 and C_2 are no longer constants, but instead have a slow evolution along the propagation axis y, which can be described with the following differential equations:[1,2]

$$\begin{cases} C_1{'} = j\kappa C_2 \exp(-j\Delta\beta y), \\ C_2{'} = j\kappa C_1 \exp(j\Delta\beta y), \end{cases} \tag{1.3}$$

where the primes denote differentiation with respect to the propagation direction (y-axis), $\Delta\beta = \beta_1 - \beta_2$ is the difference in the propagation constants of the modes, and κ is the coupling coefficient. Basically, the above equation tells that the modification of one mode amplitude is proportional to the relative amplitude of the other mode. Using a substitution of

$$\begin{cases} R(y) \equiv C_1(y)\exp\left(\frac{1}{2}j\Delta\beta y\right), \\ S(y) \equiv C_2(y)\exp\left(-\frac{1}{2}j\Delta\beta y\right), \end{cases} \tag{1.4}$$

the above equation is modified to the following:

$$\begin{cases} R' = \frac{1}{2}j\Delta\beta R + j\kappa S, \\ S' = j\kappa R - \frac{1}{2}j\Delta\beta S, \end{cases} \tag{1.5}$$

At the same time equation 1.2 will get the following form:

$$\{\mathbf{E}(x,y,z), \mathbf{H}(x,y,z)\} = [\{\mathbf{E_1}(x,z), \mathbf{H_1}(x,z)\} R(y) + \{\mathbf{E_2}(x,z), \mathbf{H_2}(x,z)\} S(y)]\exp(j\beta_{\mathrm{avg}} y), \tag{1.6}$$

with the average propagation constant $\beta_{\mathrm{avg}} = (\beta_1 + \beta_2)/2$ of the two modes. In order to solve Eq. 1.5, we search for a solution in the form $R/S = \alpha \equiv \mathrm{const}$. Then Eq. 1.5 transforms into

$$\begin{cases} \alpha S' = \frac{1}{2} j \Delta\beta \alpha S + j\kappa S, \\ S' = j\kappa\alpha S - \frac{1}{2} j \Delta\beta S; \end{cases}$$

$$\alpha \left(j\kappa\alpha - \frac{1}{2} j\Delta\beta \right) = \frac{1}{2} j\Delta\beta\alpha + j\kappa;$$

$$\alpha^2 - \frac{\Delta\beta}{\kappa}\alpha - 1 = 0;$$

$$\begin{cases} \alpha_{a,b} = \frac{\Delta\beta}{2\kappa} \pm \sqrt{1 + \left(\frac{\Delta\beta}{2\kappa}\right)^2} \equiv \Delta\beta_{\mathrm{n}} \pm \gamma, \\ \alpha_a\alpha_b = -1, \end{cases} \tag{1.7}$$

where $\Delta\beta_{\mathrm{n}} = \frac{\Delta\beta}{2\kappa}$, $\gamma = \sqrt{1 + \Delta\beta_{\mathrm{n}}^2}$. Using such α, one can get a general solution of Eq. 1.5 for R and S:

$$\begin{cases} S(y) = S_a \exp\left(j\left[\kappa\alpha_a - \frac{1}{2}\Delta\beta\right]y\right) + S_b \exp\left(j\left[\kappa\alpha_b - \frac{1}{2}\Delta\beta\right]y\right), \\ R(y) = \alpha_a S_a \exp\left(j\left[\kappa\alpha_a - \frac{1}{2}\Delta\beta\right]y\right) + \alpha_b S_b \exp\left(j\left[\kappa\alpha_b - \frac{1}{2}\Delta\beta\right]y\right), \end{cases} \tag{1.8}$$

where S_a and S_b are constants, determined from initial (boundary) conditions. One can see that each of the above two solutions represents a true mode of the system of two coupled waveguides, since then Eq. 1.6 will have the same form as for the single mode (Eq. 1.1):

$$\{\mathbf{E}(x,y,z), \mathbf{H}(x,y,z)\} = [\{\mathbf{E_1}(x,z), \mathbf{H_1}(x,z)\}\alpha + \{\mathbf{E_2}(x,z), \mathbf{H_2}(x,z)\}]S_\alpha e^{j\left(\kappa\alpha - \frac{1}{2}\Delta\beta + \beta_{\mathrm{avg}}\right)y}, \tag{1.9}$$

with the propagation constant of the mode $\beta = \beta_{\mathrm{avg}} + \kappa\alpha - \frac{1}{2}\Delta\beta$. When both waveguides are identical ($\Delta\beta = 0$), the ratio $R/S = \alpha$ is either 1 or -1 (see Eq. 1.7), therefore these supermodes are called even (symmetric) and odd (asymmetric). Their propagation constants are thus:

$$\begin{cases} \alpha_{\mathrm{even}} = \Delta\beta_{\mathrm{n}} + \gamma, \quad \alpha_{\mathrm{odd}} = \Delta\beta_{\mathrm{n}} - \gamma, \\ \beta_{\mathrm{even}} = \beta_{\mathrm{avg}} + \kappa\gamma, \quad \beta_{\mathrm{odd}} = \beta_{\mathrm{avg}} - \kappa\gamma. \end{cases} \tag{1.10}$$

Thus the CMT predicts the following conclusions: 1) the difference between propagation constants of even and odd mode (so-called splitting) is increasing with the increase of the mismatch between waveguides propagation constants ($\Delta\beta$) independently on its sign; 2) the mode with larger propagation constant tends to concentrate at the waveguide with larger propagation constant (for example, if $\kappa > 0$ and $\Delta\beta > 0$, then $\beta_{\mathrm{even}} > \beta_{\mathrm{odd}}$, but also $\alpha_{\mathrm{even}} > 1$, i.e., there is more power of the even mode in the first guide, which has larger propagation constant), and the other mode has the opposite tendency. The last is especially obvious for

the case of electro-optic modulation, where only the refractive index of waveguide environment is modulated: if even or odd mode tends to concentrate more in the place with increased refractive index, then its propagation constant should also be increased, compared to the unmodulated case. Finally, when both waveguides are identical ($\Delta\beta = 0$), the coupling coefficient can be expressed as

$$\kappa = (\beta_{\text{even}} - \beta_{\text{odd}})/2 \tag{1.11}$$

The amplitude distribution in each guide (Eq. 1.8) is convenient to express in terms of their initial values $R(y = 0) \equiv R_0$ and $S(y = 0) \equiv S_0$:

$$\begin{cases} S_a = \dfrac{R_0 - \alpha_b S_0}{\alpha_a - \alpha_b}, \\ S_b = \dfrac{\alpha_a S_0 - R_0}{\alpha_a - \alpha_b}; \end{cases}$$

$$\begin{cases} R(y) = \alpha_a S_a \exp(j\kappa\gamma y) + \alpha_b S_b \exp(-j\kappa\gamma y), \\ S(y) = S_a \exp(j\kappa\gamma y) + S_b \exp(-j\kappa\gamma y); \end{cases}$$

$$\begin{cases} R(y) = R_0 \cos(\kappa\gamma y) + j\left[\dfrac{\Delta\beta_n}{\gamma} R_0 + \dfrac{1}{\gamma} S_0\right] \sin(\kappa\gamma y), \\ S(y) = S_0 \cos(\kappa\gamma y) + j\left[\dfrac{1}{\gamma} R_0 - \dfrac{\Delta\beta_n}{\gamma} S_0\right] \sin(\kappa\gamma y). \end{cases}$$

The power distribution is then:

$$\begin{cases} |R(y)|^2 = |R_0 \cos(\kappa\gamma y)|^2 + \left|\dfrac{\Delta\beta_n R_0 + S_0}{\gamma} \sin(\kappa\gamma y)\right|^2 + 2\text{Im}\left\{R_0 \cos(\kappa\gamma y)\left[\dfrac{\Delta\beta_n R_0 + S_0}{\gamma} \sin(\kappa\gamma y)\right]^*\right\}, \\ |S(y)|^2 = |S_0 \cos(\kappa\gamma y)|^2 + \left|\dfrac{R_0 - \Delta\beta_n S_0}{\gamma} \sin(\kappa\gamma y)\right|^2 + 2\text{Im}\left\{S_0 \cos(\kappa\gamma y)\left[\dfrac{R_0 - \Delta\beta_n S_0}{\gamma} \sin(\kappa\gamma y)\right]^*\right\}. \end{cases}$$

where the asterisk indicates a complex conjugate, and Im{ } means an operator for taking the imaginary part. When all values are real, then the last term in each row of the above equation is zero, thus simplifying the equation for the power distribution:

$$\begin{cases} |R|^2 = R_0^2 \cos^2(\kappa\gamma y) + \left[\dfrac{\Delta\beta_n R_0 + S_0}{\gamma}\right]^2 \sin^2(\kappa\gamma y), \\ |S|^2 = S_0^2 \cos^2(\kappa\gamma y) + \left[\dfrac{R_0 - \Delta\beta_n S_0}{\gamma}\right]^2 \sin^2(\kappa\gamma y). \end{cases} \tag{1.12}$$

Conventional directional coupler. If light is launched only in one channel of identical waveguides ($R_0 = 1$, $S_0 = 0$), and if no modulation is applied ($\Delta\beta = 0$), then the first complete switch ($R = 0$, $S = 1$) will appear at the length L, where $\kappa\gamma L = \pi/2$, i.e, at $L = \pi/(2\kappa\gamma) = \pi/(2\kappa)$ (See Eq. 1.12). This interaction length is called a coupling length:

$$L_{\text{C}} \equiv \frac{\pi}{2\kappa} = \frac{\pi}{\beta_{\text{even}}(V=0) - \beta_{\text{odd}}(V=0)}, \tag{1.13}$$

where the propagation coefficients of even and odd modes are calculated without applied voltage.

From *even/odd mode formalism* the operation of a conventional directional coupler can be seen as following: both even and odd modes are excited with the same amplitude and phase, resulting in the constructive interference in the channel R ($R_0 = 1$) and destructive interference in the channel S ($S_0 = 0$). After propagating a length of L_{C} these modes get a phase mismatch of π due to different propagation constants, which will result in $R = 0$, $S = 1$ (i.e., destructive interference in channel R and constructive interference in channel S).

If such a device (with $L = L_{\text{C}}$) is used for modulation ($\Delta\beta \neq 0$), then the complete switch back ($R = 1$, $S = 0$) can be achieved at $\kappa\gamma L_{\text{C}} = \pi$ (according to Eq. 1.12), i.e., at $\gamma = 2$, which can be achieved at the modulation $\Delta\beta_{\text{n}} = \sqrt{3}$. The phase mismatch, achieved in such a device upon full switch, is thus $\Delta\beta L = 2\kappa\Delta\beta_{\text{n}}L_{\text{C}} = \sqrt{3}\pi$. A commonly reported number for waveguide-modulator design is the voltage V_π, required to produce the phase mismatch of π. Since $\Delta\beta$ is linearly proportional to the applied voltage (for small modifications of the refractive index), then the full-switch voltage of the conventional directional coupler is thus $V_{\text{full switch}} = \sqrt{3}V_\pi$.

From *even/odd mode formalism* the operation of a modulated directional coupler can be seen as following: the launching condition ($R_0 = 1$, $S_0 = 0$) result in the excitation of both these modes, with amplitudes resulting in a completely destructive interference in channel S (similarly to unmodulated case, but now amplitudes of even and odd modes are not the same due to the electrically induced asymmetry). If these modes acquire a phase mismatch of 2π after propagating the device length ($L = L_{\text{C}}$), then at the output they will result in the same interference condition as at the input, i.e., $|R/ = 1$, $|S/ = 0$, meaning the complete switch back. This will happen when the difference in the propagation constants of even and odd modes upon modulation is twice as large compared to the unmodulated case. From Eq. 1.10 it means $\gamma = 2$, agreeing exactly with the above derivations from CMT.

Our directional coupler. In our design both channels are equally launched ($R_0 = S_0 = 1/\sqrt{2}$). Then the optical power $|R|^2$ and $|S|^2$ in two waveguides are

$$\begin{cases} |R|^2 = \frac{1}{2}\left[1 + \frac{2\Delta\beta_{\text{n}}}{\gamma^2}\sin^2\left(\frac{\pi}{2}L_{\text{n}}\gamma\right)\right] \equiv P_1, \\ |S|^2 = \frac{1}{2}\left[1 - \frac{2\Delta\beta_{\text{n}}}{\gamma^2}\sin^2\left(\frac{\pi}{2}L_{\text{n}}\gamma\right)\right] \equiv P_2, \end{cases} \tag{1.14}$$

where $L_{\text{n}} \equiv \frac{L}{L_{\text{C}}} = \frac{2\kappa L}{\pi}$ is the normalized interaction length. Using a direct expression for γ, one can obtain equation (1) in the main text:

$$P_{1,2} = \frac{1}{2}\left[1 \pm \frac{2}{\Delta\beta_{\text{n}} + \frac{1}{\Delta\beta_{\text{n}}}}\sin^2\left(\frac{\pi}{2}L_{\text{n}}\sqrt{1 + \Delta\beta_{\text{n}}^2}\right)\right] \tag{1.15}$$

With no modulation voltage applied, the coupler is inherently operating at its 3 dB point due to the symmetry of the system. By applying a voltage, light can be coupled from one channel into the other by introducing an electro-optically induced mismatch $\Delta\beta$ between the propagation constants of the coupled waveguides. The full off-state in one channel (when P_1 or P_2 equal to zero) can be reached when $|\Delta\beta_n| = 1$ (i.e., the required voltage should change propagation constant of each channel to the same amount as the difference between those of the even and odd mode at no modulation), and when the sine function is at maximum amplitude (i.e., $\frac{\pi}{2}L_n\sqrt{1 + \Delta\beta_n^2} = \frac{\pi}{2} + \pi m$, $\sqrt{2}L_n = 1 + 2m$, where m is an integer number, $m \in \mathbb{Z}$). Thus, the smallest interaction length required for the complete switch is $L = L_C/\sqrt{2}$. It might seem that our device is superior to a conventional directional coupler in both shorter device length (by a factor of $\sqrt{2}$) and smaller voltage (by a factor of $\sqrt{3}$) required for the complete switch. However, the full-switch voltage should be calculated for the transition from the complete off-state to the complete on-state (e.g., from $P_1 = 0, P_2 = 1$ to $P_1 = 1, P_2 = 0$), and not from the balanced 3 dB point as in our device at no modulation. Thus, the condition for the complete switch is $|\Delta\beta_n| = 2$, corresponding to the phase mismatch of $\Delta\beta L = 2\kappa\Delta\beta_n L_C/\sqrt{2} = \sqrt{2}\pi$. The full-switch voltage is then $V_{\text{full switch}} = \sqrt{2}V_\pi$, which is still smaller than the one for a conventional directional coupler.

From *even/odd mode formalism* the operation of our directional coupler can be seen as following: when no modulation is applied, only the even mode is excited, therefore the power distribution in both guides is the same at any point along the propagation ($R = S$). However, when the voltage is applied, the initial condition does not satisfy the excitation of only the even mode (since the refractive index distribution becomes uneven, so even and odd modes are not completely even and odd in terms of field distribution – see Eq. 1.10). A complete off-state in one of the channels (R or S) can be achieved when contributions from even and odd modes to this channel interfere destructively, i.e., they equal in amplitude, but their phase mismatch is $\pi + \pi m, m \in \mathbb{Z}$. One can show that the condition for equal amplitudes is achieved when the asymmetry coefficient α of even/odd mode is $1\pm\sqrt{2}$. Comparing with Eq. 1.7 this means $|\Delta\beta_n| = 1$, agreeing to the above derivations from CMT. The condition for the opposite phase between even and odd modes results in the following: $[\beta_{\text{odd}}(V) - \beta_{\text{even}}(V)]L = \pi + 2\pi m, m \in \mathbb{Z}$. Using Eq. 1.10 and Eq. 1.13, it will transform into $\pi L_n \gamma = \pi + 2\pi m$, or $\sqrt{2}L_n = 1 + 2m$ (since $\gamma = \sqrt{2}$ for $|\Delta\beta_n| = 1$). This is exactly the same condition for the normalized interaction length as derived from CMT. Note that at this condition the difference in modified propagation constants of even and odd modes is increased by a factor of $\sqrt{2}$, compared to the unmodulated one: $\beta_{\text{even}}(V) - \beta_{\text{odd}}(V) = \sqrt{2}[\beta_{\text{even}}(V = 0) - \beta_{\text{odd}}(V = 0)]$.

Supplementary Figure 1 below shows the output power $P_{1,2}$ in each channel versus the normalized interaction length L_n for different $\Delta\beta_n$, calculated with Eq. 1.15. The absolute maximum modulation depth (full switch-off in P_2) is achieved when $\Delta\beta_n = 1$ and $L_n = (1 + 2m)/\sqrt{2}$, as predicted above. However, if such modulation

$\Delta\beta$ cannot be achieved (for example, due to the limitations in voltage supply or electric breakdown of the device), strongest modulation is achieved for a different device length, when $L_n = 1/\sqrt{1 + {\Delta\beta_n}^2}$, i.e., when the sine function in Eq. 1.15 reaches 1. Finally, one can note that for positive modulation $\Delta\beta_n > 0$ plotted in Supplementary Figure 1 (meaning $\beta_1 > \beta_2$) the power in the first channel is always larger than the one in the second channel ($P_1 \geq P_2$). This can be intuitively understood by the light's tendency to leak towards optically denser medium, which is waveguide 1 in our case.
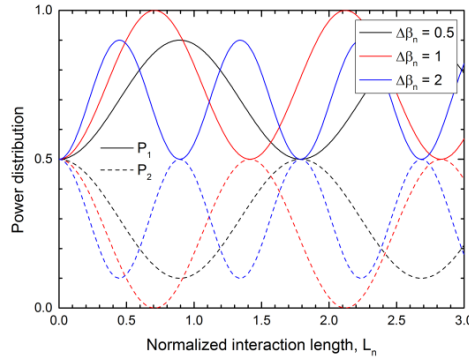
Supplementary Figure 1. Output power P_1 (solid) and P_2 (dashed) versus the normalized interaction length L_n for different $\Delta\beta_n = 0.5$ (black), 1 (red), 2 (blue). In our experimental study, the directional coupler satisfies the condition of $L_n = 1$, thus allowing full optical switching.

Mach-Zehnder interferometer. In a usual Mach-Zehnder interferometer a single waveguide splits into two identical waveguides (arms of the interferometer), which after propagating some lengths are combined into a single waveguide. Both splitting and merging acts as a filter for the even mode. That is, after the splitting the power in each arm is the same ($R_0 = S_0$), and at the merging junction the transmitted power into the single waveguide is proportional to $|R + S|$. Therefore, when no modulation is applied, and both interferometers arms are identical, then the transmission is at maximum (100% in the lossless case). In order to switch-off the transmission, one needs to apply the modulation, such that modes R and S at the merging junction will be out-of-phase, i.e., $\Delta\beta L = \pi$. Thus, the full-switch voltage in Mach-Zehnder interferometer device is $V_{\text{full switch}} = V_\pi$, which is the smallest among studied here devices. The drawbacks of Mach-Zehnder interferometer-based modulator is larger size and extra losses due to Y-junctions and routing required to separate interferometer arms.

Supplementary Note 2: Numerical electrostatic and mode analysis

Numerical simulations accompanying CMT are performed using a finite element method solver, implemented in commercially available software (Comsol Multiphysics 5.2a). In the first step, electrostatic simulations (Supplementary Figures 2a,c) are performed, in which the relative permittivity of air is set to $\varepsilon_{air} = 1$, and the boundaries of the two gold nanostripes are set to ground and V_{bias} potential, respectively. For simulations at small modulation frequencies (< 1 MHz) we used the unclamped static relative permittivity tensor of LN taken from Jazbinsek et al.[3] ($\varepsilon_{xx} = \varepsilon_{yy} = 84.48$, $\underline{\varepsilon_{zz}} = 27.78$). At higher frequencies (> 10 MHz) the crystal strain can no longer follow the changes of the external electric field. Thus, the clamped static relative permittivity tensor of LN taken from Jazbinsek et al.[3] ($\varepsilon_{xx} = \varepsilon_{yy} = 45.52$, $\varepsilon_{zz} = 26.22$) is used for the estimation of the device bandwidth (calculated from its capacitance). According to our simulations (see Supplementary Figure 2), there is a negligible difference in the electrostatic field distribution, calculated for unclamped and clamped values of LN permittivity. However, the clamped permittivity of LN reduces the modulation by ~20%, and results in almost 1.5 times smaller capacitance, as compared to the simulations with unclamped values of LN permittivity.
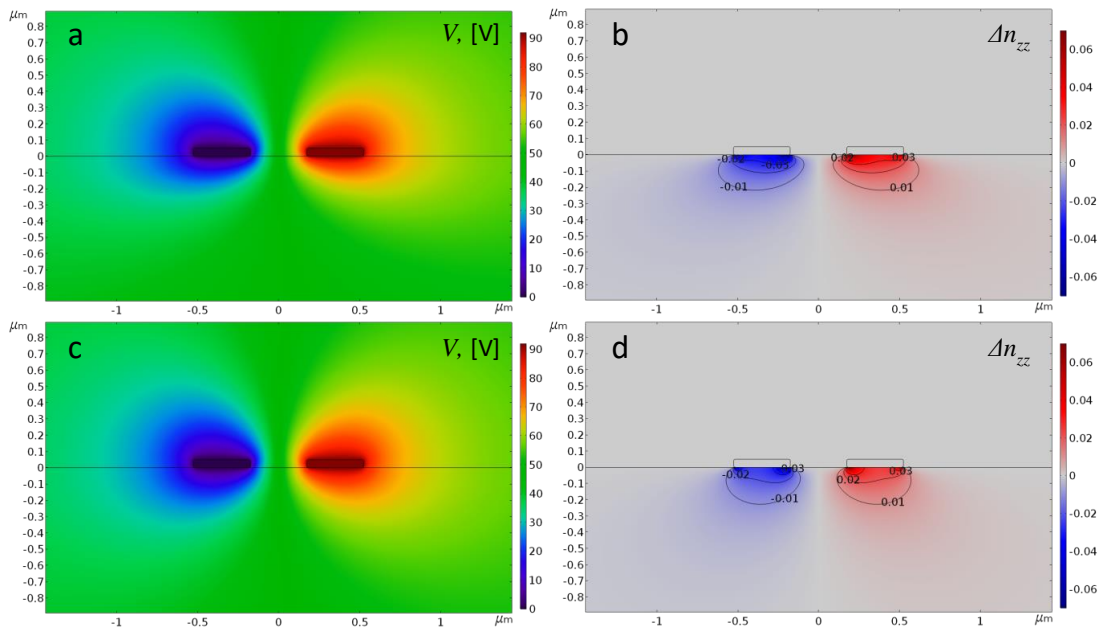
Supplementary Figure 2. Electrostatic simulations upon applying a full-switch voltage (92 V for our device), illustrating the distribution of the (a, c) potential and (b, d) electrically-induced change in the refractive index Δn_{zz} (corresponding to the extraordinary axis of LN substrate), calculated while using (a, b) unclamped and (c, d) clamped permittivity of LN.

The calculated electric-field distribution is utilized to determine the modification of the refractive index in the LN substrate (Supplementary Figures 2b,d) by using the electro-optic Pockels coefficients from Jazbinsek et

al.[3] (restricting to the largest diagonal terms, i.e., $\Delta n_{ii} = -0.5 r_{iiz} n_{ii}^3 E_z$, with $r_{xxz} = r_{yyz} = 10.12$ pm/V and $r_{zzz} = 31.45$ pm/V). For the optical simulation, the modified distribution of the refractive index of LN is fed into the mode solver, while the unmodified refractive index of LN was taken from Zelmon et al.[4] ($n_{xx} = n_{yy} = n_o = 2.211$, $n_{zz} = n_e = 2.138$ at $\lambda_0 = 1550$ nm). The refractive index of gold was taken from Lorentz-Drude (LD) fitting model[5]. A perfectly matched layer is applied on the boundary of the circular simulation domain (with a diameter of 10 μm) in order to absorb optical leakage. To distinguish real modes from cavity modes, the simulation domain size was varied (the effective mode index $N_{\text{eff}} \equiv \dfrac{\beta}{k_0} = \dfrac{\lambda \beta}{2\pi}$ and the field distribution of real modes does not depend on the simulation domain size, on the contrary to those of cavity modes). The calculated modes are leaky, because of their effective mode indices are being lower that the ordinary refractive index of LN substrate ($n_o = 2.211$). To estimate the amount of losses due to the leakage, we duplicated simulations with a lossless gold (by setting $\text{Im}[\varepsilon_{\text{Au}}] = 0$). It appeared that the leakage losses are responsible only for a few percent of total losses and is thus neglectable compared to the plasmonic loss.

In order to determine the coupling coefficient κ used in CMT, mode analysis was performed with both metal stripes present and unmodified refractive index of LN substrate (Supplementary Figures 3a,b). The calculated even and odd mode, and their effective mode indices ($n_{\text{even}} = 2.168$ and $n_{\text{odd}} = 2.133$) were used to determine the coupling coefficient κ (using Eq. 1.11) and the corresponding coupling length $L_C = 21.9$ μm (using Eq. 1.13).
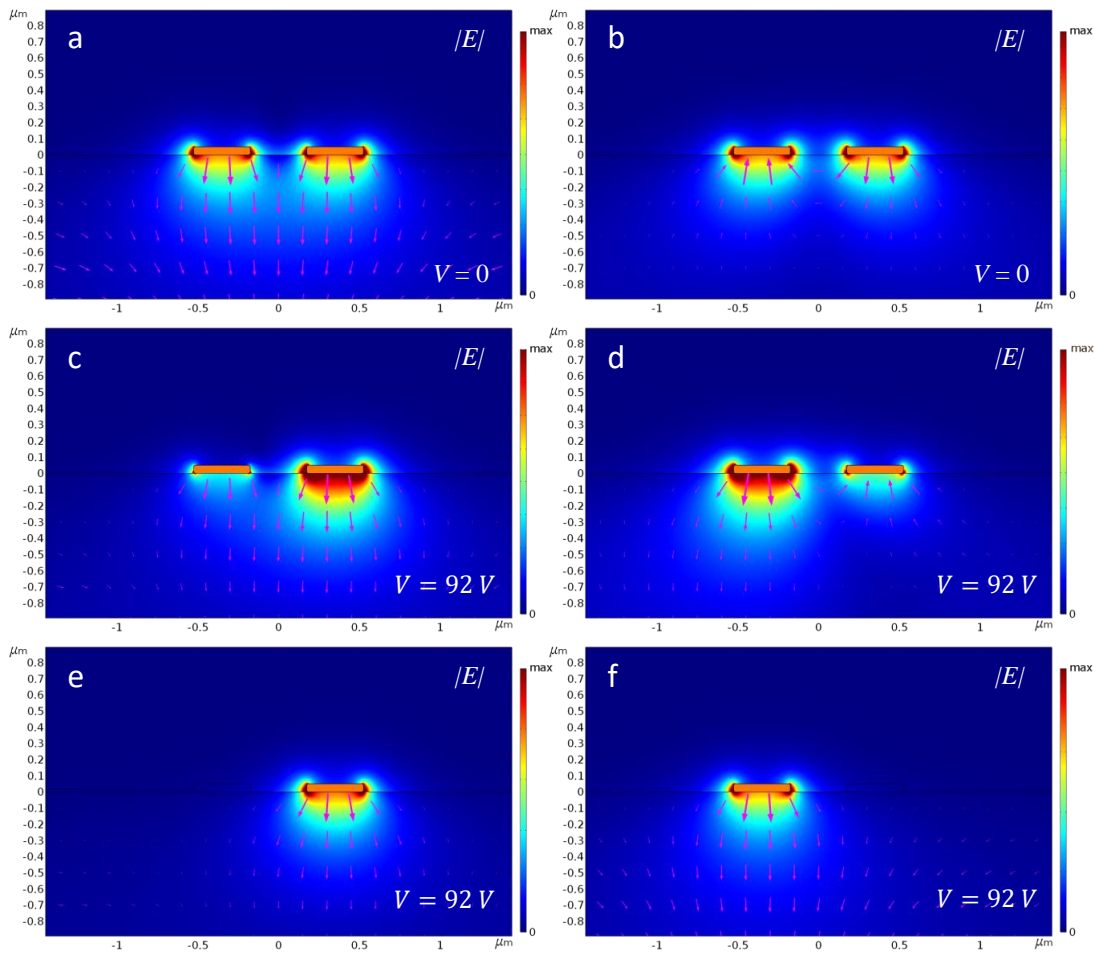
Supplementary Figure 3. (a, b) Optical $|E|$-field distributions for (a) even and (b) odd modes, when no voltage is applied. **(c-f)** Optical $|E|$-field distributions for (c) even, (d) odd, and (e,f) modes of individual waveguides upon applied full-switch voltage ($V = 92$ V). Gold waveguides are marked in orange. Magenta arrows represent transverse components of the optical E-field. The even mode localizes more in the region with increased refractive index, resulting in the increase of its effective mode index upon applied bias voltage. On the contrary, the odd mode has the opposite tendency.

In order to calculate the modification $\beta(V) - \beta(V = 0)$ of the propagation constants of each individual mode as a function of the applied voltage, we consider a single metal stripe in our model (Supplementary Figures 3e,f), and used the modified refractive index of LN substrate determined in the previous electrostatic step. Additionally, to prove the predictions of CMT, we run the mode analysis with both waveguides present and find modified even and odd modes (Supplementary Figures 3c,d). The strong asymmetry of even and odd mode distributions, predicted by CMT (with the asymmetry coefficient $\alpha = 1 \pm \sqrt{2}$ at full switch-off voltage), is clearly verified as shown in Supplementary Figures 3c,d.

The results of optical simulations are summarized in Supplementary Figure 4 below. As can be seen in Supplementary Figure 4b, using clamped values of LN permittivity reduces the modulation by ~20%, as compared to the modulation, calculated with unclamped values of LN permittivity. Overall, the CMT predicted effective mode indices are in good agreement with ones found in the numerical simulations.
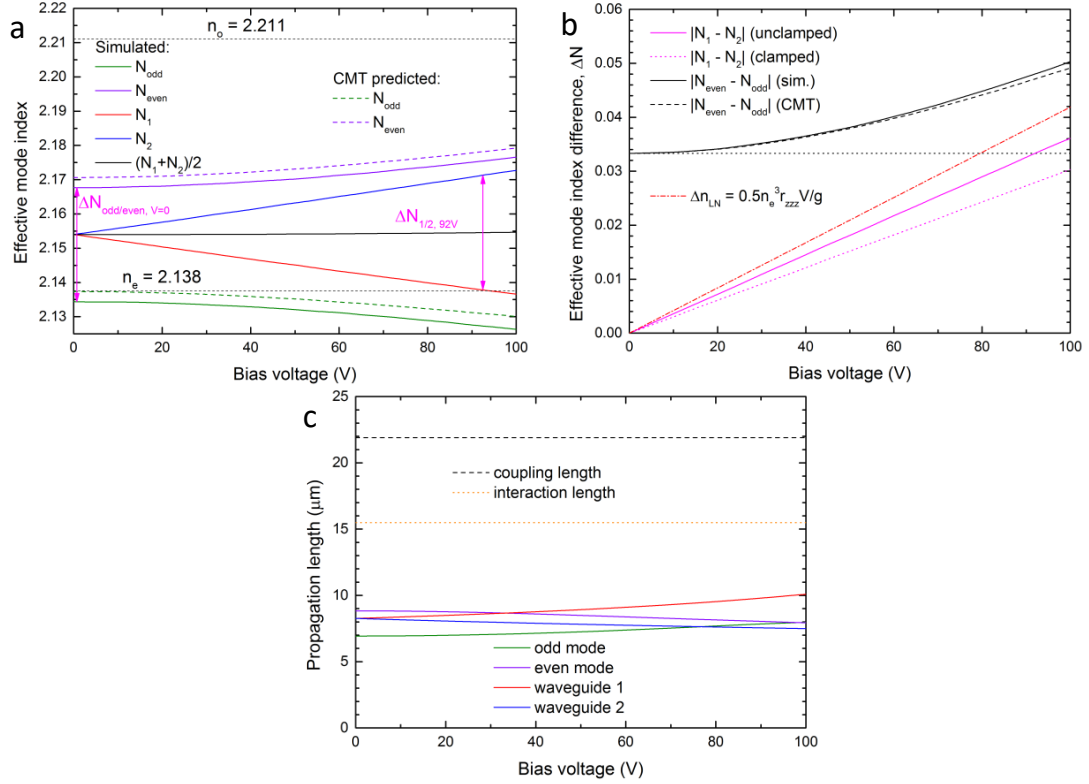
Supplementary Figure 4. a Effective mode index as a function of the applied bias voltage. Predictions from CMT are plotted with dashed lines. **b** Difference in the effective mode indices of individual waveguides ($|N_1$-$N_2|$, magenta lines), and of even and odd modes ($|N_{even}$ - $N_{odd}|$, black line) as a function of the applied bias voltage. Predictions from CMT are plotted with dashed lines. Full switch condition is achieved in our device when $|\Delta\beta_n| = 1$, i.e., when the electrically-induced difference in effective mode indices of individual waveguides, $|N_1$-$N_2|$ (magenta solid line), is equal to the difference in the effective mode indices of even and odd modes at no applied voltage, $|N_{even,V=0}$ - $N_{odd,V=0}|$ (black dotted line). This is satisfied at the bias voltage of ~92 V. Magenta dotted line shows calculations when using clamped values of LN permittivity; the rest is calculated with unclamped values of LN permittivity. Red dash-dotted line shows the expected average electrically-induced change in the refractive index of LN, assuming average electrostatic field as $E_z = V/g$, where $g = 350$ nm is the edge-to-edge separation of waveguides. **c** Propagation length as a function of the applied bias voltage for individual waveguide modes and even/odd supermodes. Black dashed line shows the

coupling length L_C; orange dotted line shows the optimal interaction length $L = L_C/\sqrt{2}$, required for a complete switch.

Finally, by comparing the effective mode index modulation $|N_1\text{-}N_2|$ and the expected average electrically-induced change in the refractive index of LN Δn_{LN} (assuming average electrostatic field as $E_z = V/g$, where $g = 350$ nm is the edge-to-edge separation of waveguides), one can calculate the interaction factor Γ, which quantifies the strength of the nonlinear electro-optic interaction of modulating field and optical mode:[6,7,8]

$$\Gamma \equiv \frac{|N_1 - N_1|}{\Delta n_{LN}} = \frac{\lambda g}{V_\pi L n_e^3 r_{zzz}}, \tag{2.1}$$

where L is the optimal interaction length, $L = L_C/\sqrt{2}$. We found that in our configuration it is $\Gamma \approx 0.86$, meaning quite a good overlap between electrostatic (RF) and optical fields.

Supplementary Note 3: Influence of free-space wavelength

In this section we study how the chosen free-space wavelength influences the modulator performance. For this the simulation domain was the same (350×50-nm^2 Au waveguides, separated by 350-nm gap), and the wavelength was varied. The Pockels coefficients of LN were kept constant. Since the modulation $\Delta\beta$ is linearly proportional to the applied voltage (as verified in Supplementary Figure 4b), here we did simulations only for the voltage of 0 and 50 V. At 0 V we calculated effective mode indices of even and odd mode in order to find the coupling length L_C and required modulation for the complete switch $\Delta\beta = 2[\beta_{\text{even}}(V=0) - \beta_{\text{odd}}(V=0)]$. For single-waveguide simulations (when the other waveguide is set to air) we did simulations at 0 and 50 V to find $\Delta\beta_{50\text{ V}}$, which we used to calculate the required full switch-off voltage

$$V_{\text{full switch}} = 2 \cdot [50 \text{ V}] \frac{\beta_{\text{even}}(V=0) - \beta_{\text{odd}}(V=0)}{\Delta\beta_{50\text{ V}}} \tag{3.1}$$

We plot two figures of merit: 1) drive voltage-length product $VL = V_{\text{full switch}}L_C/\sqrt{2}$, and 2) normalized drive voltage-length product VL/L_{prop}, where the normalization is done over the propagation length (calculated for single waveguide at zero applied voltage).
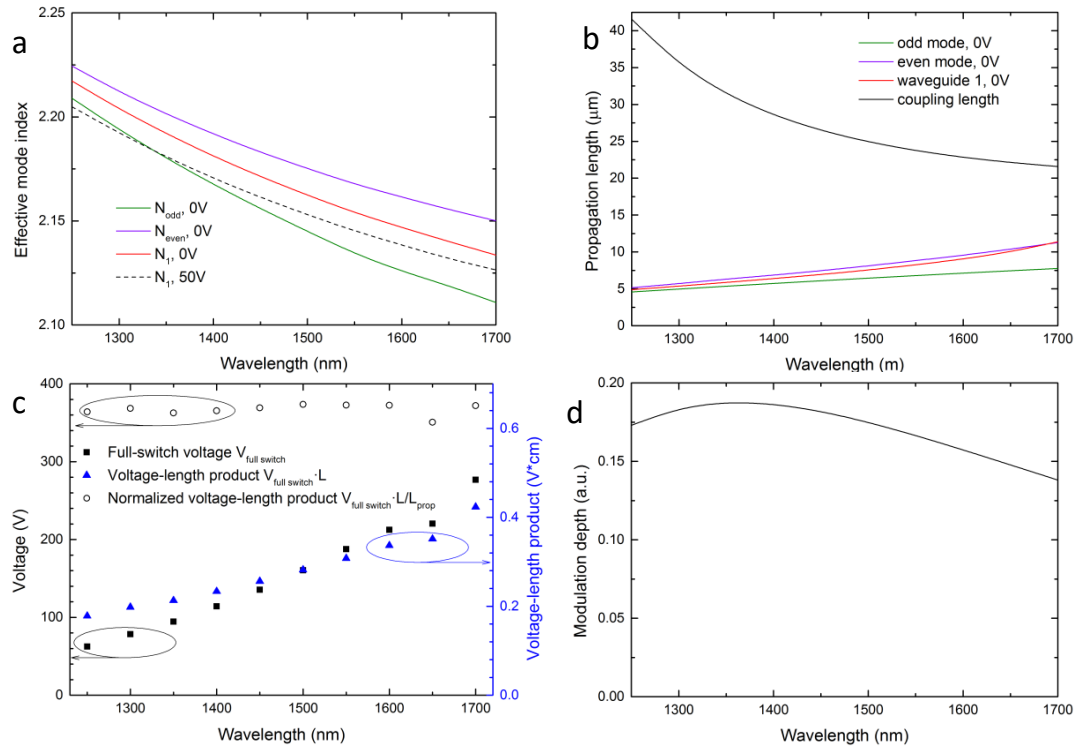
Supplementary Figure 5. a Wavelength dependence of the effective mode index of even (violet), odd (green), and mode of the individual waveguide (red) at zero applied voltage, compared with the effective mode index of individual waveguide mode at the applied voltage of 50 V (black dashed line). **b** Propagation length as a function of the wavelength for individual waveguide mode (red) and even/odd supermodes (violed and green,

respectively). Black line shows the coupling length L_C. **c** Estimated full-switch voltage $V_{\text{full switch}}$ (black filled squares), voltage-length product $V_{\text{full switch}}L$ (blue filled triangles), and voltage-length product, normalized to the propagation length, $V_{\text{full switch}}L/L_{\text{prop}}$ (black hollow circles). **d** Wavelength dependence of the modulation depth of the same device, optimized at $\lambda = 1550$ nm, at small driving voltages.

One can see in Supplementary Figure 5a that for a shorter wavelength, the modulation (change in N_1) is higher due to the higher refractive index of LN (since electro-optic modulation Δn is proportional to n^3), and due to the higher mode confinement (optical mode distribution like the one on Supplementary Figure 2e is more confined to the gold/LN interface, where the electro-optically induced change of the refractive index is highest). At the same time the difference between even and odd mode indices decreases with the decrease of the wavelength. Consequently, the coupling length increases at shorter wavelengths (and thus the full-switch device length) (Supplementary Figure 5b), but the required full-switch voltage becomes smaller (Supplementary Figure 5c). The voltage-length product is also smaller for shorter wavelengths, but when normalized to the propagation length, VL/L_{prop} becomes nearly constant for all investigated wavelengths (Supplementary Figure 5c), because the propagation length decreases substantially with a decrease of the wavelength (Supplementary Figure 5b). Considering the voltage-length-loss product, there is no significant benefit in changing the operation wavelength band.

Finally, we investigate the wavelength dependence of the modulation depth of our device, which was optimized for the free-space wavelength of $\lambda = 1550$ nm (reported also as Figure 4b in the main text). From Eq. 1.15 it follows that for small modulation ($|\Delta\beta_n| \ll 1$) the modulation depth is

$$\text{MD}(\lambda) = \frac{P_1(V) - P_1(V=0)}{P_1(V=0)} \approx \Delta\beta_n(\lambda)\sin^2\left(\frac{\pi}{2}\frac{L}{L_C(\lambda)}\right) \propto \Delta\beta(\lambda)L_C(\lambda)\sin^2\left(\frac{\pi}{2}\frac{L}{L_C(\lambda)}\right), \qquad (3.2)$$

where $L = L_C(\lambda = 1550 \text{ nm})/\sqrt{2}$ is interaction length in our device. We plot the last expression in Eq. 3.2 in Supplementary Figure 5d, while the exact solution for a modulation voltage of 15 V is plotted in Figure 4b of the main text (in dB scale and normalized to the value at our operation wavelength of 1550 nm). The product of the first two terms in Eq. 3.2 [i.e., $\Delta\beta(\lambda)L_C(\lambda)$] is inversely proportional to the voltage-length product, therefore it causes the increase of the modulation depth with the decrease of the voltage. However, the last sine term in the above equation decreases with the decrease of the wavelength (resulting in the increase of the coupling length), therefore there is an extremum (maximum) at the wavelength where the above factors cancel each other out.

Supplementary Note 4: Fabrication tolerance analysis of the investigated coupler switch

The influence of structural deviations induced by fabrication uncertainties on the switching performance in the proposed directional coupler is investigated. Therefore, a fabrication tolerance analysis at a fixed driving voltage of V_{bias} = 15 V is conducted by varying the two most critical design parameters, i.e., waveguide separation and waveguide width, affecting the switching performance. Though the variation of the modulation depth depends on the driving voltage, it is sufficient in telecommunication applications to operate the modulator at a modulation depth of ~ 25 %, which is achieved at the driving voltage of 15 V. Supplementary Figure 6a shows the influence on the modulation depth in terms of deviation of the waveguide separation distance. The gap dimensions between two coupling waveguides primarily affects the coupling length, and thus $L_n = L/L_c$ introduced in the description of the coupled mode formalism in Supplementary Note 1, which is found to have an optimum value of $L_n = \sqrt{2}$ for highest modulation depth at a fixed interaction length L. The fact that the maximum depth is observed at slightly smaller separation than g = 350 nm (the optimum design conditions at L = 15.6 nm) is due to a stronger electrostatic field at smaller separation distance, which results in a larger electro-optically induced phase mismatch in the two waveguide arms. Overall, the variation in the modulation depth is fairly small, varying less than 8% over a separation distances from 250 to 450 nm. By investigating deviations of the waveguide width w, while keeping the separation distance fixed at g = 350 nm, a steady increase of the modulation depth widths is observed for smaller waveguides (Supplementary Figure 6b). This behavior can be explained by the local enhancement of both, the optical and electrostatic field, for smaller waveguide widths, which results in an increased phase mismatch and thus higher modulation depth. However, smaller waveguide width results in higher losses of the whole device, therefore we chose w = 350 nm as a compromise between high losses and low modulation depth. Details on the design optimization can be found in Supplementary Note 5. The inset in Supplementary Figure 6b shows exemplarily the enhanced electrostatic field at smaller waveguide width (w = 250 nm), inducing a stronger modification of the refractive index, compared to a larger waveguide width (w = 450 nm). Within a waveguide width deviation of Δw = 100 nm, the modulation depth varies less than 10 %. Generally, the symmetrically fed directional coupler configuration exhibits more relaxed fabrication constraints than Mach-Zehnder or resonator-based modulators[9].
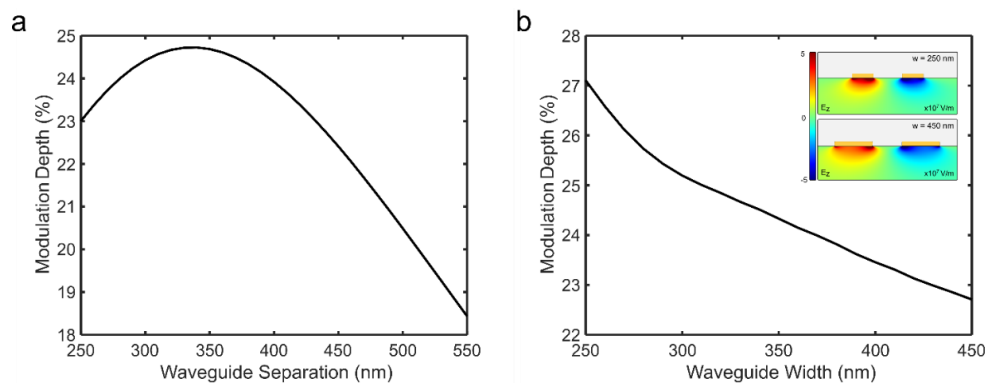
Supplementary Figure 6. Parametric geometric tolerance analysis of the directional coupler switch at $V_{bias} = 15$ V driving voltage. **a** Modulation depth versus waveguide separation with the fixed waveguide dimensions of 350×50 nm². **b** Modulation depth versus waveguide width with the fixed separation distance of 350 nm.

Supplementary Note 5: Design optimization for dual-channel phase modulators and directional coupler switches

In this section, a numerical optimization of the cross-section design is presented first in the general context of a dual-channel phase modulator. Since its practical implication is not restricted to the directional coupler switch (other device platforms like Mach-Zehnder interferometers or resonators are possible), we investigate the influence on the cross-section geometry on the half-wave voltage-length product for a phase shift of π between the two waveguides, the plasmonic losses and its interplay as voltage-length-loss product (FOM $= V_\pi L\alpha$). For simplicity, the separation distance between the two wires is fixed at 350 nm as in our experimentally realized device. By reducing the waveguide dimension, the voltage-length product $V_\pi L$ can be reduced to below 0.2 V·cm (Supplementary Figure 7a). This is due to the tight optical confinement in smaller waveguides which enhances the light-matter interaction of the propagating mode (i.e. the mode is more confined close to the stripe where the refractive index change is largest). Contrarily, as the mode confinement becomes tighter, propagation losses are increasing for smaller waveguide dimensions (Supplementary Figure **7**b). For waveguide-based device platforms in which the total optical losses should be kept reasonably small, an optimal trade-off between electro-optic efficiency (Supplementary Figure. **7**a) and loss (Supplementary Figure **7**b) must be found. Therefore, by multiplying the figures of merit, we defined the voltage-length-loss product $V_\pi L\alpha$ (Supplementary Figure **7**c). Since the losses decrease faster than $V_\pi L$ increases with larger waveguide dimensions, we observe a steady decrease of the voltage-length-loss product for larger waveguide dimensions. Nevertheless, for each waveguide width one can find an optimal waveguide thickness in which best device performance regarding $V_\pi L\alpha$ is found, indicated as red line in Fig. S7c. The used waveguide geometry in our experiment (marked as black diamond in Supplementary Figure 7) is close to this optimal condition.

In our directional coupler modulator, another relevant parameter that dictates the device performance is the coupling length L_c (Supplementary Figure 7d). As described in Supplementary Note 1, the optimal interaction length is $L = L_c\sqrt{2}$. By multiplying the optimum interaction length with the propagation loss α, one can determine the insertion loss of the directional coupler (Supplementary Figure 7e). In our study, we target a small voltage-length product with an acceptable optical insertion loss which is kept below 6 dB, thus exhibiting comparable insertion losses as in commercially available electro-optic modulators[10]. By keeping the waveguide thickness at 50 nm and further decreasing the waveguide width, the voltage-length product can be reduced while the insertion loss (due to plasmonic propagation) is kept below 6 dB, since the optimum interaction length scales with the reduced coupling length. However, this only provides minor performance improvements and introduces potential performance fluctuations due to fabrication imperfections (i.e. stronger thickness dependence of $V_\pi L$ and α at smaller waveguide width). Furthermore, the maximum extinction ratio is limited in lossy (plasmonic) directional couplers, when $L_c \gtrsim L_{\text{prop}}$, due to the difference in propagations

17

losses in even and odd mode. The maximum extinction ratio in the conventional passive directional coupler can be defined by[11]

$$\text{ER}_{max} = \max(P_1/P_2) = \{\tanh(\text{Im}[\Delta n]k_0 L_c)\}^{-2} \tag{5.1}$$

where the difference in the effective mode indices of the odd and even mode is $\Delta n = n_{odd} - n_{even}$, k_0 is the free-space wave vector and L_c is the coupling length. Our passive directional coupler device is expected to have a maximum extinction ratio of more than 20 dB (Supplementary Figure 7f), which is well below the electro-optically induced extinction ratio of 10 dB in the active device.
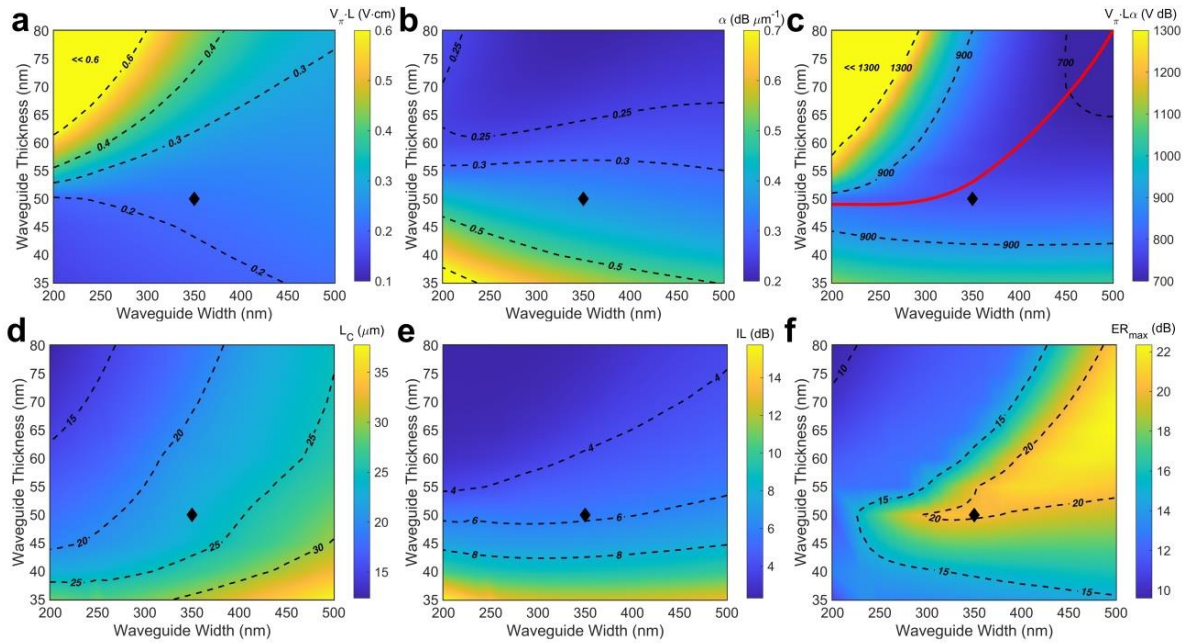
Supplementary Figure 7. (a-c) Design optimization for the plasmonic phase modulator. Figures of merit (**a** Half-wave voltage-length product $V_\pi L$, **b** propagation loss α, **c** voltage-length-loss product $V_\pi L\alpha$) are presented as a function of the waveguide dimensions with fixed waveguide spacing of 350 nm. The red line in **c** indicates the optimal width-thickness ratio where the smallest voltage-length-loss product can be found. **(d-f) Parametric study of the plasmonic directional coupler. d** Coupling length, **e** insertion loss (IL) and **f** maximum extinction ratio (ER) as a function waveguide width and thickness of a directional coupler with fixed separation distance of 350 nm. The black diamond shows the design parameters used in this work (350×50 nm^2).

Supplementary Note 6: Device capacitance and power consumption

By performing 3D-FEM simulations, the capacitance of the device with an interaction length of 15.5 um was found to be 3.6 fF, which dictates the capacitance-limited modulation bandwidth to be approximately 800 GHz with a 50 Ω source impedance. The calculated capacitance for different device lengths is shown in Supplementary Figure 8a. The energy consumption as a function of the modulation depth can be estimated according to[17]:

$$E = \frac{1}{4} C V_{\text{bias}}^2 \, , \tag{6.1}$$

where C is the device capacitance of the directional coupler and V_{bias} is the driving voltage. The calculated energy consumption as a function of the modulation depth translated from the modulation voltage is shown in Supplementary Figure 8b. Considering that most applications require relatively low modulation depth, operation with an energy consumption below 1 pJ bit^{-1} is feasible, which is smaller than many silicon-based photonic modulators.
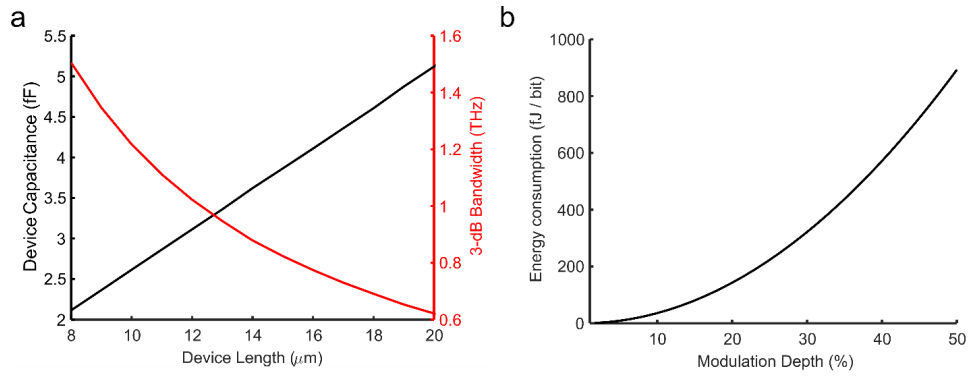
Supplementary Figure 8. Simulated electric-optical characteristics of the directional coupler modulator **a** Device capacitance and 3-dB bandwidth of the directional coupler modulator with a 50 Ω source impedance **b** Energy consumption as a function of the modulation depth.

Supplementary Note 7: Experimental set-up for measuring the modulation characteristics

A far-field optical setup (Supplementary Figure 9) is used for characterizing the electro-optic modulator. A tunable IR telecom laser is providing a collimated laser beam with a selectable wavelength. After the beam is periodically interrupted with the frequency f_c by an optical chopper (optional for the RF measurement), its polarization is defined by a polarizer (Pol) and a half-wave plate (HWP). The beam (p-polarization) passes through a polarizing beam splitter and IR-objective ($\times$ 100 magnification, NA=0.95). The focused diffraction-limited beam excites the plasmonic mode by precisely positioning the device under test (DUT). The incident beam is symmetrically illuminating the input grating coupling, in a way that the power at the output grating ports collected by the objective is equally distributed. The polarization of the emitted signal from the terminating coupling gratings is rotated by the waveguide bend to be orthogonal to the polarization of the incident beam and thus allowing suppression of back-reflections from the incident beam by the polarizing beam splitter. The signal is spatially filtered at the image plane to extract power only from one of the output ports. Using a fiber collimator, the signal is fiber-coupled and detected by an InGaAs high-speed photodetector. For electro-optically modulation, the driving voltage with frequency f_m is applied to the plasmonic structure, by mechanical clamping of electric probes on the connecting electrode pads of the chip. The wavelength- and voltage-dependent modulation depth is measured with an oscilloscope. For the high-speed measurement, the modulated signal is measured with a spectrum analyzer (SA), where the electro-optically modulated optical signal is observed at the intentionally shifted frequency caused by modulating the signal with the optical chopper. In this way the chopper modulation generates sidebands at $f_m \pm f_c$, which are contrary to the carrier signal free of electrical noise induced by electrical crosstalk between signal generator and spectrum analyzer (see Supplementary Note 8).
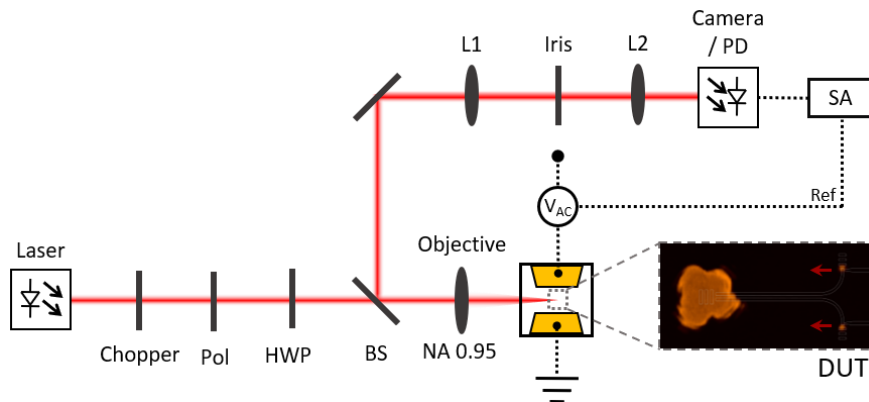
Supplementary Figure 9. Experimental set-up for characterizing the plasmonic modulator. The optical path is illustrated as red lines and the electrical wiring as dashed black lines.

Supplementary Note 8: RF characterization

The limited sensitivity of the photodetector (Thorlabs PDA8GS) and the fact that we did not include an optical amplifier in the detection path resulted in an RF transfer function of the overall system of as low as -140 dB. We did not have access to a vector network analyzer of the required bandwidth and dynamic range. Instead, we measured the RF response by exciting the modulator with a microwave synthesizer (HP8672S, excitation level approx. +10 dBm) and detecting the photocurrent with a separate RF spectrum analyzer (Rohde&Schwarz FSM, noise floor approx. -150 dBm at 6 Hz resolution bandwidth).

The plasmonic modulator was placed at the end of a coplanar waveguide composed of a 150 nm thick gold wire on the LiNbO$_3$ substrate with a characteristic impedance of 50 Ω +- 20%, a length of approx. 5 mm and an Ohmic resistance of 20-30 Ω. This waveguide was terminated by two thin gold wires (50 nm thick, designed to be 100 Ω each) fabricated together with the modulator. The termination wire resistance was subject to considerable variation from sample to sample leading to tolerable ripple in the RF-response.

On the opposite end, the coplanar waveguide was contacted by a low-profile RF-probe that was made in-house specifically to fit in the working distance of the microscope objective. It involved three contact tips, which formed a 2 mm short poorly matched coplanar waveguide (approx. 200 Ω characteristic impedance). Finally, the optical signal was detected with a commercial photoreceiver module connected directly to the spectrum analyzer. The detector is specified with a bandwidth of 9.5 GHz and according to the vendor has a first-order low-pass response.

The low RF signal at the receiver led to significant problems with direct crosstalk due to leakage from RF cables and through power cords. Because of the strong background signal at the microwave stimulus frequency and the sidebands at the harmonics of the power grid frequency, we modulated the optical incident power with a chopper at 75 Hz introducing RF-sidebands that were an unambiguous signature of the optical modulator.

We calibrated the frequency dependence of the stimulus power level caused by variations in the synthesizer and the cablework by replacing the RF contacts with a bolometric power detector (HP8481B). Furthermore, we subtracted the typical response of the photodetector (first-order low-pass pole at 9.5 GHz) from the total signal. Since we did not have access to a vector network analyzer or a reflectometer with the necessary bandwidth, we could not calibrate out the RF response of the contact pads and the on-chip waveguide. As an alternative, we simulated it using designed (characteristic impedance of the waveguide and the contact tips) and measured parameters (Ohmic resistance of the waveguide and the termination resistor). The resulting RF-response is shown in Supplementary Figure 10 alongside an equivalent schematic. We find that this RF model is in excellent agreement with the measured data (both shown in Fig. 4c of the main text). We stress that the model was not fitted to the measured data but was based on unrelated measurements. Therefore, we are confident that the apparent drop in modulated signal at higher frequencies is due to imperfections in the RF

contacts and feedline. We do not observe any bandwidth limitation from the plasmonic modulator itself as expected from our earlier estimates based on the device's capacitance.
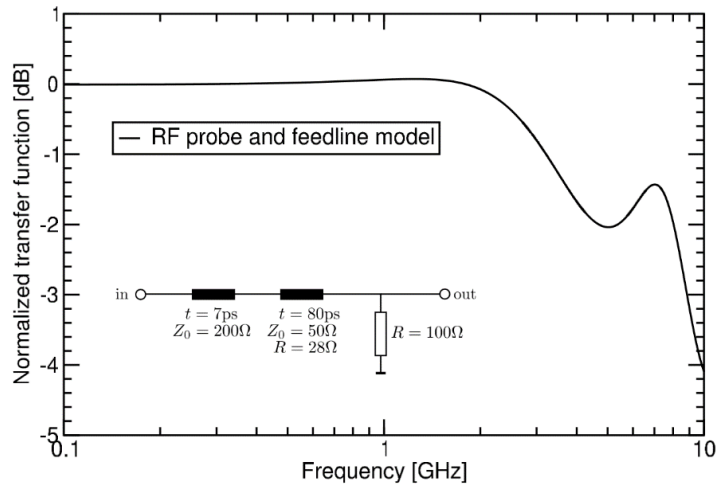
Supplementary Figure 10. The resulting RF response of the designed (characteristic impedance of the waveguide and the contact tips) and measured parameters (Ohmic resistance of the waveguide and the termination resistor) in our experiment, alongside an equivalent schematic (inset).

Supplementary Note 9: Near-field investigation of the directional coupler

We study the near-field evolution of directional coupling using an AFM-based phase-resolved scattering-type scanning near-field optical microscope (SNOM from NeaSpec) operated in a transmission configuration[12-15]. A commercial Si probe, coated by PtIr alloy (Arrow NcPt, NanoWorld), is used in a non-contact tapping mode (tapping frequency ~250 kHz, tapping amplitude ~50 nm). Scattering from this probe, measured by an amplified InGaAs detector, is demodulated at third harmonic of the tapping frequency in order to get rid of a strong background (bulk scattering from the tip, the cantilever, and the sample itself, which is not modulated by the tip-sample distance). The setup additionally employs a Mach-Zehnder interferometer with modulated phase of the reference arm (by means of mirror oscillations at a frequency ~300 Hz), which allows using a pseuhederodyne demodulation[16] to resolve both the amplitude and the phase. As a source, we used a telecom laser (New Focus Venturi TLB-6600) at CW output ($\lambda = 1550$ nm, ~8 mW), which was focused onto the sample (spot FWHM by intensity ~3.5 μm, corresponding to the NA ~0.16) normally from below by a custom-made right-angle parabolic mirror.

In order to investigate directional coupling and measure the coupling length accurately, we fabricated directional couplers with input into one of the channels (Supplementary Figure 11a), which equally excites even and odd modes. The fabricated directional coupler on *z*-cut LN incorporates a tapered grating which transforms free-space light from a loosely focused beam into a single nanowire waveguiding mode. After propagating 3 μm through a single waveguide, an identical adjacent waveguide is introduced, enabling evanescent coupling between those two waveguides. The length of the directional coupler is chosen large enough to avoid back reflections from its termination. Shortly after scanning the fabricated devices we encountered a problem of sample charging, which prohibits the tip to come close to the sample surface, making it impossible to record proper topography and near-field signal. We believe it is because of a piezoelectric effect of LN, caused by the oscillating tip, therefore we deposited 10 nm of SiO_2 to suppress this effect. By numerical simulations we have verified that this additional layer does not significantly influence modal properties of the system (though additional losses might appear due to the scattering on the roughness, caused by this layer). The dashed white box in Supplementary Figure 11a indicates the scanned area. An AFM topography image of this area is shown in Supplementary Figure 11b, along with the recorded near-field maps of the amplitude and the phase (Supplementary Figures 11c-d). Noticeably when approaching the 3-dB coupling point, a $\pi/2$ relative phase shift between the throughput light and the coupled light is observed as expected for evanescent coupling between two closely spaced identical waveguides. The near-field data of the coupling section is first analyzed in the Fourier domain, and then fitted as a sum of propagating modes by a least square method[12-16]. The mode effective indices and propagation lengths of the odd and even modes are measured for three different coupler configurations and compared with numerical simulations (Supplementary Table 1). A movie of the evolution of the real-valued field is provided in Supplementary Movie 1.
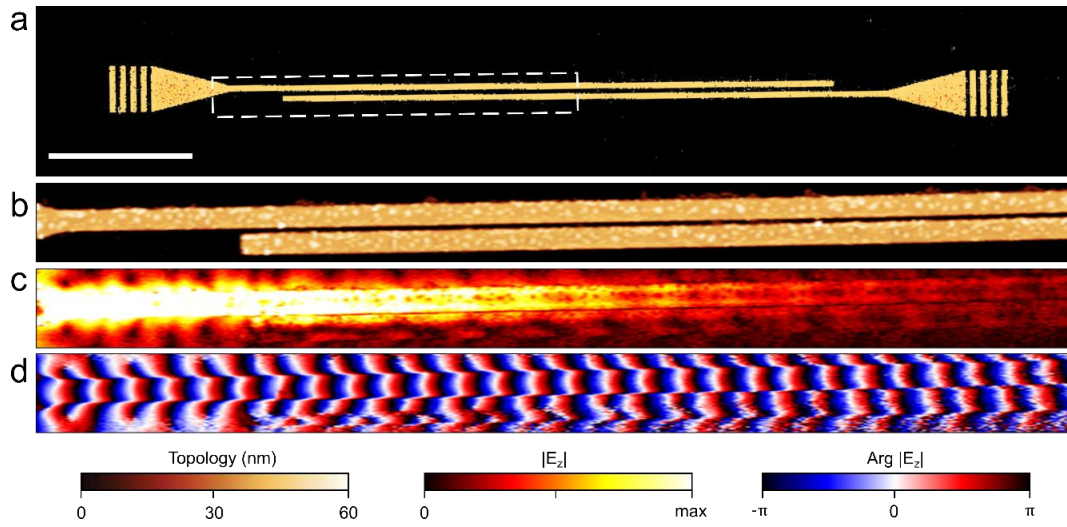
Supplementary Figure 11. Near-field investigation of the plasmonic directional coupler using phase-resolved scattering-type near-field optical microscopy (s-SNOM). **a** False-color scanning electron microscope (SEM) image of the investigated directional coupler with tapered grating coupler. A laser beam with the wavelength $\lambda_0 = 1550$ nm is positioned at the left input grating in order to couple optical power into one plasmonic waveguide arm. The dashed box indicates the area that was investigated using s-SNOM. The scale bar represents 10 µm. **b** Atomic Force Microscopy (AFM) topography of the investigated area, **c** near-field amplitude $|E_z|$, and **d** near-field phase Arg$[E_z]$, measured with s-SNOM.

Waveguide dimensions		$420{\times}50$ nm^2	$420{\times}50$ nm^2	$390{\times}50$ nm^2
Separation		100 nm	200 nm	190 nm
Experiment	n_{odd}	2.22±0.01	2.21±0.01	2.20±0.01
	n_{even}	2.12±0.01	2.15±0.01	2.15±0.01
	$L_{\mathrm{P,odd}}$	4±2 µm	7±4 µm	8±4 µm
	$L_{\mathrm{P,even}}$	1.2±0.5 µm	3±2 µm	3±2 µm
	L_{C}	8±2 µm	13±4 µm	14±6 µm
Simulations	n_{odd}	2.171	2.169	2.167
	n_{even}	2.119	2.122	2.119
	$L_{\mathrm{P,odd}}$	14.2 µm	13.7 µm	13.1 µm
	$L_{\mathrm{P,even}}$	8.6 µm	9.0 µm	9.7 µm
	L_{C}	14.9 µm	16.5 µm	16.1 µm

Supplementary Table 1. Experimentally obtained mode effective indices and propagation length of the odd and even mode, compared with numerical simulations.

Supplementary Note 10: Comparison with state-of-the-art electro-optic modulators

Material Platform	r_{33} / pm·V^{-1}	Thermal stability	$V_\pi \cdot L$ / V · cm	Insertion loss / dB	Reference
LN	30	+	9.4	1	[18]
LN	30	+	6.4	0.3	[19]
PZT	61	+/-	3.2	0.05	[20]
LN	30	+	2.2	0.4	[21]
LN	30	+	1.8	1.5	[22]
BTO	107	+/-	0.66	N/A	[23]
BTO	340	+/-	0.45	2.1	[24]
LN (Plasmonic)	**30**	**+**	**0.21**	**5.5**	**Our work**
EOP M3	91	-	0.11	2.5	[25]
EOP YLD-124 (Plasmonic)	100	-	0.012	6	[26]
EOP DLD-164 (Plasmonic)	180	-	0.006	2.5	[27]

Supplementary Table 2. Comparison of state-of-the-art electro-optic Pockels modulators sorted by the half-wavevoltage-length product. The material platform used in the individual modulator devices are lithium niobite (LN), lead zirconate titanate (PZT), barium titanate (BTO) and electro-optic polymers (EOP). The insertion loss is defined by the waveguide propagation loss in the phase-shifter section. The thermal stability is classified by the threshold temperature T_t of structural phase transition in the material to be low (-) at $T_t < 100$ °C, medium (+/-) at 100 °C $< T_t < 300$ °C or high (+) at $T_t > 300$ °C.

References

[1] Alferness, R. Guided-wave devices for optical communication. *IEEE J. Quantum Elect.* **17**, 946–959 (1981).

[2] Kogelnik, H. and Schmidt R. Switched directional couplers with alternating ΔB. *IEEE J. Quantum Elect.* **12**, 396–401 (1976).

[3] Jazbinšek, M. and Zgonik, M. Material tensor parameters of LiNbO3 relevant for electro- and elasto-optics. *Appl. Phys. B* **74**, 407–414 (2002).

[4] Zelmon, D. E., Small, D. L. and Jundt, D. Infrared corrected Sellmeier coefficients for congruently grown lithium niobate and 5 mol % magnesium oxide–doped lithium niobate. *J. Opt. Soc. Am. B* **14**, 3319-3322 (1997).

[5] Rakić, A. D., Djurišic, A. B., Elazar, J. M. and Majewski. M. L. Optical properties of metallic films for vertical-cavity optoelectronic devices, *Appl. Opt.* **37**, 5271-5283 (1998).

[6] Brosi J-M, Koos C, Andreani LC, Waldow M, Leuthold J, Freude W. High-speed low-voltage electro-optic modulator with a polymer-infiltrated silicon photonic crystal waveguide. *Opt. Express* **16**, 4177-4191 (2008).

[7] Witzens J, Baehr-Jones T, Hochberg M. Design of transmission line driven slot waveguide Mach-Zehnder interferometers and application to analog optical links. *Opt. Express* **18**, 16902-16928 (2010).

[8] Alexander, K. et al. Nanophotonic Pockels modulators on a silicon nitride platform. *Nat. Commun.* **9**, 3444 (2018)

[9] Tavlykaev, R. F. and Ramaswamy, R. V. Highly linear Y-fed directional coupler modulator with low intermodulation distortion. *J. Lightwave Technol.* **17**, 282–291 (1999).

[10] *Lithium Niobate Electro-Optic Modulators*. https://www.thorlabs.com (2019)

[11] Zenin, V. A., Volkov, V. S., Han, Z., Bozhevolnyi, S. I., Devaux, E. and Ebbesen, T. W. Directional coupling in channel plasmon-polariton waveguides. *Opt. Express* **20**, 6124-6134 (2012).

[12] Deshpande, R., Zenin, V. A., Ding F., Mortensen, N. A. and Bozhevolnyi, S. I. Direct Characterization of Near-Field Coupling in Gap Plasmon-Based Metasurfaces. *Nano Lett.* **18**, 6265-6270 (2018).

[13] DeVault, C. T., Zenin, V. A., Pors, A., Chaudhuri, K., Kim, J., Boltasseva, A., Shalaev, V. M. and Bozhevolnyi, S. I. Suppression of near-field coupling in plasmonic antennas on epsilon-near-zero substrates. *Optica* **5**, 1557-1563 (2018).

[14] Zenin, V. A., Choudhury, S., Saha, S., Shalaev, V. M., Boltasseva, A. and Bozhevolnyi, S. I. Hybrid plasmonic waveguides formed by metal coating of dielectric ridges. *Opt. Express* **25**, 12295-12302 (2017).

[15] Zenin, V. A., Malureanu, R., Radko, I. P., Lavrinenko, A. V. and Bozhevolnyi, S. I. Near-field characterization of bound plasmonic modes in metal strip waveguides. *Opt. Express* **24**, 4582-4590 (2016).

[16] Ocelic, N., Huber, A. and Hillenbrand, R. Pseudoheterodyne detection for background-free near-field spectroscopy. *Appl. Phys. Lett.* **89**, 101124 (2006).

[17] Miller, D. A. Energy consumption in optical modulators for interconnects. *Opt. Express* **20**, A293-A308, (2012).

[18] Mercante, A. J., Yao, P., Shi, S., Schneider, G., Murakowski, J., and Prather, D. W. 110 GHz CMOS compatible thin film LiNbO3 modulator on silicon. *Opt. Express* **24**, 15590–15595 (2016).

[19] Weigel, P. O. *et al.* Bonded thin film lithium niobate modulator on a silicon photonics platform exceeding 100 GHz 3-dB electrical modulation bandwidth. *Opt. Express* **26**, 23728-23729 (2018).

[20] Alexander, K. *et al.* Nanophotonic Pockels modulators on a silicon nitride platform. *Nat. Commun.* **9**, 3444 (2018).

[21] Wang, C. *et al.* Integrated lithium niobate electro-optic modulators operating at CMOS-compatible voltages. *Nature* **562**, 101–104 (2018).

[22] Wang, C., Zhang, M., Stern, B., Lipson, M., and Lončar, M. Nanophotonic lithium niobate electro-optic modulators. *Opt. Express* **26**, 1547-1555 (2018).

[23] Girouard, P., Chen, P., Jeong, Y., Liu, Z., Ho, S.-T., and Wessels, B. W. $\chi^{(2)}$ Modulator With 40-GHz Modulation Utilizing BaTiO3 Photonic Crystal Waveguides. *IEEE J. Quantum Elect.* **53**, 1–10 (2017).

[24] Abel, S. *et al.* Large Pockels effect in micro- and nanostructured barium titanate integrated on silicon. *Nat. Materials* **18**, 42–47 (2019).

[25] Alloatti, L. *et al.* 100 GHz silicon–organic hybrid modulator. *Light Sci. Appl.* **3**, e173 (2014).

[26] Ayata, M. *et al.* High-speed plasmonic modulator in a single metal layer. *Science* **358**, 630–632 (2017).

[27] Haffner, C. *et al.* All-plasmonic Mach–Zehnder modulator enabling optical high-speed communication at the microscale. *Nat. Photonics* **9**, 525–528 (2015).

Declaration of Authorship

Authorship Agreement

This authorship agreement concerns the published research work conducted by PhD Student Martin Thomaschewski, Yuanqing Yang and Sergey I. Bozhevolnyi.

The research work includes the following articles:

Nanoscale 10, 16178 - 16183 (2018)
Ultra-compact branchless plasmonic interferometers

In accordance with the criteria put forward at the Vancouver Convention for authorship (www.icmje.org), the undersigned Martin Thomaschewski confirms that he as first author is responsible for

- a substantial contribution of the intellectual content
- writing of drafts and final version of the paper (main author)
- all figures
- chip-scale fabrication of all examined structures
- the acquisition and interpretation of experimental evidence
- the finalization of the versions to be published

Similarly, the undersigned Yuanqing Yang and Sergey I. Bozhevolnyi confirm that they as co-author have contributed quantitatively and qualitatively to the conception and design, the critical revision for important intellectual content, the interpretation of experimental evidence, and the final approval of the versions to be published. As senior researcher Sergey I. Bozhevolnyi, stands as guarantor and takes public responsibility for the integrity of the research work as a whole, from inception to published articles.

Yuanqing Yang

Sergey I. Bozhevolnyi

Martin Thomaschewski

Authorship Agreement

This authorship agreement concerns the published research work conducted by PhD Student Martin Thomaschewski, Yuanqing Yang, Christian Wolff, Alexander S. Roberts and Sergey I. Bozhevolnyi.

The research work includes the following articles:

Nano Letters 19, 2, 1166-1171 (2019)

On-Chip Detection of Optical Spin–Orbit Interactions in Plasmonic Nanocircuits

In accordance with the criteria put forward at the Vancouver Convention for authorship (www.icmje.org), the undersigned Martin Thomaschewski confirms that he as first author is responsible for

- a substantial contribution of the intellectual content
- writing of drafts and final version of the paper (main author)
- all figures
- chip-scale fabrication of all examined structures
- the acquisition and interpretation of experimental evidence
- the finalization of the versions to be published

Similarly, the undersigned Yuanqing Yang, Christian Wolff, Alexander S. Roberts and Sergey I. Bozhevolnyi confirm that they as co-author have contributed quantitatively and qualitatively to the conception and design, the critical revision for important intellectual content, the interpretation of experimental evidence, and the final approval of the versions to be published. As senior researcher Sergey I. Bozhevolnyi, stands as guarantor and takes public responsibility for the integrity of the research work as a whole, from inception to published articles.

Yuanqing Yang

Christian Wolff

Alexander S. Roberts

Sergey I. Bozhevolnyi

Martin Thomaschewski

Authorship Agreement

This authorship agreement concerns the published research work conducted by PhD Student Martin Thomaschewski, Vladimir A. Zenin, Christian Wolff and Sergey I. Bozhevolnyi.

The research work includes the following articles:

Nature Communications 11, 748 (2020)
Plasmonic monolithic lithium niobate directional coupler switches

In accordance with the criteria put forward at the Vancouver Convention for authorship (www.icmje.org), the undersigned Martin Thomaschewski confirms that he as first author is responsible for

- a substantial contribution of the intellectual content
- writing of drafts and final version of the paper (main author)
- all figures
- chip-scale fabrication of all examined structures
- the acquisition and interpretation of experimental evidence
- numerical simulations and theoretical analysis
- the finalization of the versions to be published

Similarly, the Vladimir A. Zenin, Christian Wolff and Sergey I. Bozhevolnyi confirm that they as co-author have contributed quantitatively and qualitatively to the conception and design, the critical revision for important intellectual content, the interpretation of experimental evidence, and the final approval of the versions to be published. As senior researcher Sergey I. Bozhevolnyi, stands as guarantor and takes public responsibility for the integrity of the research work as a whole, from inception to published articles.
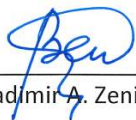
_____
Vladimir A. Zenin

_____
Christian Wolff

_____
Sergey I. Bozhevolnyi

_____
Martin Thomaschewski

Bibliography

1. Winzer, P. J., Neilson, D. T. & Chraplyvy, A. R. Fiber-optic transmission and networking: the previous 20 and the next 20 years. *Opt. Express* **26,** 24190–24239 (2018).

2. Kaminow, I. P., Li, T. & Willner, A. E. *Optical Fiber Telecommunications VIA* (Academic Press, Boston, 2013).

3. Andrae, A. S. & Edler, T. On global electricity usage of communication technology: trends to 2030. *Challenges* **6,** 117–157 (2015).

4. Dakin, J. Handbook of Optoelectronics (2006).

5. Ebbesen, T. W., Genet, C. & Bozhevolnyi, S. I. Surface-plasmon circuitry. *Phys. Today* **61,** 44–50 (2008).

6. Feynman, R. P. There's plenty of room at the bottom. *J. Microelectromech. Syst.* **1,** 60–66 (1992).

7. Drude, P. Zur Elektronentheorie der Metalle. *Annalen der Physik* **306,** 566–613 (1900).

8. Drude, P. Zur Elektronentheorie der Metalle; II. Teil. Galvanomagnetische und thermomagnetische Effecte. *Annalen der Physik* **308,** 369–402 (1900).

9. West, P. R. *et al.* Searching for better plasmonic materials. *Laser Photonics Rev.* **4,** 795–808 (2010).

10. Johnson, P. B. & Christy, R. W. Optical Constants of the Noble Metals. *Phys. Rev. B* **6,** 4370–4379 (12 1972).

11. Rakić, A. D. Algorithm for the determination of intrinsic optical constants of metal films: application to aluminum. *Appl. Opt.* **34,** 4755–4767 (1995).

12. Bliokh, K. Y., Bekshaev, A. Y. & Nori, F. Extraordinary momentum and spin in evanescent waves. *Nat. Commun.* **5,** 1–8 (2014).

13. Thomaschewski, M., Yang, Y. & Bozhevolnyi, S. I. Ultra-compact branchless plasmonic interferometers. *Nanoscale* **10,** 16178–16183 (2018).

14. Thomaschewski, M., Yang, Y., Wolff, C., Roberts, A. S. & Bozhevolnyi, S. I. On-Chip Detection of Optical Spin–Orbit Interactions in Plasmonic Nanocircuits. *Nano Lett.* **19,** 1166–1171 (2019).

15. Thomaschewski, M., Zenin, V., Wolff, C. & Bozhevolnyi, S. Plasmonic monolithic lithium niobate directional coupler switches. English. *Nat. Commun.* **11** (2020).

16. Malitson, I. H. Interspecimen Comparison of the Refractive Index of Fused Silica. *J. Opt. Soc. Am.* **55,** 1205–1209 (1965).

17. Nunley, T. N. *et al.* Optical constants of germanium and thermally grown germanium dioxide from 0.5 to 6.6 eV via a multisample ellipsometry investigation. *J. Vac. Sci. Technol. B* **34,** 61205 (2016).

18. Zelmon, D. E., Small, D. L. & Jundt, D. Infrared corrected Sellmeier coefficients for congruently grown lithium niobate and 5 mol. % magnesium oxide–doped lithium niobate. *J. Opt. Soc. Am. B* **14,** 3319–3322 (1997).

19. Melikyan, A. *et al.* High-speed plasmonic phase modulators. *Nat. Photonics* **8,** 229–233 (2014).

20. Aspnes, D. & Studna, A. Dielectric functions and optical parameters of Si, Ge, GaP, GaAs, GaSb, InP, InAs, and InSb from 1.5 to 6.0 eV. *Phys. Rev. B* **27,** 985–1009 (2 1983).

21. Berini, P., Charbonneau, R., Jetté-Charbonneau, S., Lahoud, N. & Mattiussi, G. Long-range surface plasmon-polariton waveguides and devices in lithium niobate. *J. Appl. Phys.* **101,** 113114 (2007).

22. Boltasseva, A. *et al.* Integrated optical components utilizing long-range surface plasmon polaritons. *J. Light. Technol* **23,** 413 (2005).

23. Berini, P. Long-range surface plasmon polaritons. *Adv. Opt. Photonics* **1,** 484–588 (2009).

24. Berini, P, Charbonneau, R, Lahoud, N & Mattiussi, G. Characterization of long-range surface-plasmon-polariton waveguides. *J. Appl. Phys.* **98,** 043109 (2005).

25. Charbonneau, R., Berini, P., Berolo, E. & Lisicka-Shrzek, E. Experimental observation of plasmon–polariton waves supported by a thin metal film of finite width. *Opt. Lett.* **25,** 844–846 (2000).

26. Vernoux, C. *et al.* Flexible long-range surface plasmon polariton single-mode waveguide for optical interconnects. *Optical Materials Express* **8,** 469–484 (2018).

27. Kim, J. T. *et al.* Chip-to-chip optical interconnect using gold long-range surface plasmon polariton waveguides. *Opt. Express* **16,** 13133–13138 (2008).

28. Kim, J. T. *et al.* Low-loss polymer-based long-range surface plasmon-polariton waveguide. *IEEE Photon. Technol.* **19,** 1374–1376 (2007).

29. Ju, J. J. *et al.* Polymer-based long-range surface plasmon polariton waveguides for 10-Gbps optical signal transmission applications. *J. Light. Technol* **26,** 1510–1518 (2008).

30. Kretschmann, E & Raether, H. Notizen: Radiative Decay of Non Radiative Surface Plasmons Excited by Light. *Z. Naturforsch. A* **23** (1968).

31. Otto, A. Excitation of nonradiative surface plasma waves in silver by the method of frustrated total reflection. *Z. Phys.* **216,** 398–410 (1968).

32. Andryieuski, A. & Lavrinenko, A. V. Nanocouplers for infrared and visible light. *Adv. Optoelectron.* **2012** (2012).

33. Ayata, M. *et al.* High-speed plasmonic modulator in a single metal layer. *Science* **358,** 630–632 (2017).

34. Ayata, M., Fedoryshyn, Y., Koch, U. & Leuthold, J. Compact, ultra-broadband plasmonic grating couplers. *Opt. Express* **27,** 29719–29729 (2019).

35. Andkjær, J., Nishiwaki, S., Nomura, T. & Sigmund, O. Topology optimization of grating couplers for the efficient excitation of surface plasmons. *J. Opt. Soc. Am. B* **27,** 1828–1832 (2010).

36. Maqsood, M. W., Mehfuz, R & Chau, K. J. High-throughput diffraction-assisted surface-plasmon-polariton coupling by a super-wavelength slit. *Opt. Express* **18,** 21669–21677 (2010).

37. Novotny, L. & van Hulst, N. Antennas for light. *Nat. Photonics* **5,** 83–90 (2011).

38. Balanis, C. A. *Antenna theory: analysis and design* (Wiley-Interscience, 2005).

39. Andryieuski, A., Malureanu, R., Biagi, G., Holmgaard, T. & Lavrinenko, A. Compact dipole nanoantenna coupler to plasmonic slot waveguide. *Opt. Lett.* **37,** 1124–1126 (2012).

40. Novotny, L. Effective Wavelength Scaling for Optical Antennas. *Phys. Rev. Lett.* **98,** 266802 (26 2007).

41. Bliokh, K. Y., Rodríguez-Fortuño, F. J., Nori, F & Zayats, A. V. Spin–orbit interactions of light. *Nat. Photonics* **9,** 796–808 (2015).

42. Bliokh, K. Y., Smirnova, D. & Nori, F. Quantum spin Hall effect of light. *Science* **348,** 1448–1451 (2015).

43. Yin, X., Ye, Z., Rho, J., Wang, Y. & Zhang, X. Photonic Spin Hall Effect at Metasurfaces. *Science* **339,** 1405–1407 (2013).

44. Bliokh, K. Y., Gorodetski, Y., Kleiner, V. & Hasman, E. Coriolis Effect in Optics: Unified Geometric Phase and Spin-Hall Effect. *Phys. Rev. Lett.* **101,** 030404 (3 2008).

45. Dai, Y., Dąbrowski, M., Apkarian, V. A. & Petek, H. Ultrafast Microscopy of Spin-Momentum-Locked Surface Plasmon Polaritons. *ACS Nano* **12,** 6588–6596 (2018).

46. Lefier, Y. & Grosjean, T. Unidirectional sub-diffraction waveguiding based on optical spin-orbit coupling in subwavelength plasmonic waveguides. *Opt. Lett.* **40,** 2890–2893 (2015).

47. Lefier, Y., Salut, R., Suarez, M. A. & Grosjean, T. Directing Nanoscale Optical Flows by Coupling Photon Spin to Plasmon Extrinsic Angular Momentum. *Nano Lett.* **18,** 38–42 (2018).

48. Prämassing, M, Liebtrau, M, Schill, H., Irsen, S & Linden, S. Interferometric near-field characterization of plasmonic slot waveguides in single-and poly-crystalline gold films. *Opt. Express* **28,** 12998–13007 (2020).

49. Deshpande, R., Zenin, V. A., Ding, F., Mortensen, N. A. & Bozhevolnyi, S. I. Direct characterization of near-field coupling in gap plasmon-based metasurfaces. *Nano Lett.* **18,** 6265–6270 (2018).

50. DeVault, C. T. *et al.* Suppression of near-field coupling in plasmonic antennas on epsilon-near-zero substrates. *Optica* **5,** 1557–1563 (2018).

51. Zenin, V. A., Malureanu, R., Radko, I. P., Lavrinenko, A. V. & Bozhevolnyi, S. I. Near-field characterization of bound plasmonic modes in metal strip waveguides. *Opt. Express* **24,** 4582–4590 (2016).

52. Schinke, C. *et al.* Uncertainty analysis for the coefficient of band-to-band absorption of crystalline silicon. *AIP Adv.* **5,** 067168 (2015).

53. Nunley, T. N. *et al.* Optical constants of germanium and thermally grown germanium dioxide from 0.5 to 6.6 eV via a multisample ellipsometry investigation. *Journal of Vacuum Science & Technology B, Nanotechnology and Microelectronics: Materials, Processing, Measurement, and Phenomena* **34,** 061205 (2016).

54. Adachi, S. Optical dispersion relations for GaP, GaAs, GaSb, InP, InAs, InSb, $Al_xGa_{1-x}As$, and $In_{1-x}Ga_xAs_yP_{1-y}$. *J. Appl. Phys.* **66,** 6030–6040 (1989).

55. Salamin, Y. *et al.* 100 GHz Plasmonic Photodetector. *ACS Photonics* **5,** 3291–3297 (2018).

56. Chalabi, H., Schoen, D. & Brongersma, M. L. Hot-Electron Photodetection with a Plasmonic Nanostripe Antenna. *Nano Lett.* **14,** 1374–1380 (2014).

57. Wang, F. & Melosh, N. A. Plasmonic Energy Collection through Hot Carrier Extraction. *Nano Lett.* **11,** 5426–5430 (2011).

58. Knight, M. W., Sobhani, H., Nordlander, P. & Halas, N. J. Photodetection with Active Optical Antennas. *Science* **332,** 702–704 (2011).

59. Knight, M. W. *et al.* Embedding Plasmonic Nanostructure Diodes Enhances Hot Electron Emission. *Nano Lett.* **13,** 1687–1692 (2013).

60. Chen, L. & Lipson, M. Ultra-low capacitance and high speed germanium photodetectors on silicon. *Opt. Express* **17,** 7901–7906 (2009).

61. Assefa, S. *et al.* CMOS-integrated high-speed MSM germanium waveguide photodetector. *Opt. Express* **18,** 4986–4999 (2010).

62. Dorodnyy, A. *et al.* Plasmonic photodetectors. *IEEE J. Sel. Top. Quantum Electron.* **24,** 1–13 (2018).

63. Echtermeyer, T. *et al.* Strong plasmonic enhancement of photovoltage in graphene. *Nat. Commun.* **2,** 1–5 (2011).

64. Afshinmanesh, F., White, J. S., Cai, W. & Brongersma, M. L. Measurement of the polarization state of light using an integrated plasmonic polarimeter. *Nanophotonics* **1,** 125–129 (2012).

65. Ma, P. *et al.* Plasmonically enhanced graphene photodetector featuring 100 Gbit/s data reception, high responsivity, and compact size. *ACS Photonics* **6,** 154–161 (2018).

66. Sobhani, A. *et al.* Enhancing the photocurrent and photoluminescence of single crystal monolayer MoS2 with resonant plasmonic nanoshells. *Appl. Phys. Lett.* **104,** 031112 (2014).

67. Wang, H. *et al.* Plasmonically enabled two-dimensional material-based optoelectronic devices. *Nanoscale* (2020).

68. Ly-Gagnon, D.-S. *et al.* Routing and photodetection in subwavelength plasmonic slot waveguides. *Nanophotonics* **1,** 9–16 (2012).

69. Sobhani, A. *et al.* Narrowband photodetection in the near-infrared with a plasmon-induced hot electron device. *Nat. Commun.* **4,** 1–6 (2013).

70. Tan, C. L., Lysak, V. V., Alameh, K. & Lee, Y. T. Absorption enhancement of 980 nm MSM photodetector with a plasmonic grating structure. *Opt. Commun.* **283,** 1763–1767 (2010).

71. Emboras, A. *et al.* Electrically controlled plasmonic switches and modulators. *IEEE J. Sel. Top. Quantum Electron.* **21,** 276–283 (2014).

72. Abadia, N. *et al. A CMOS-compatible Franz-Keldysh effect plasmonic modulator* in *11th International Conference on Group IV Photonics (GFP)* (2014), 63–64.

73. Dumas, D. *et al.* Ge/SiGe quantum confined Stark effect electro-absorption modulation with low voltage swing at λ= 1550 nm. *Opt. Express* **22,** 19284–19292 (2014).

74. Ansell, D *et al.* Hybrid graphene plasmonic waveguide modulators. *Nature communications* **6,** 1–6 (2015).

75. Emboras, A. *et al.* Atomic scale plasmonic switch. *Nano Lett.* **16,** 709–714 (2016).

76. Zhang, W. *et al.* Atomic switches of metallic point contacts by plasmonic heating. *Light Sci. Appl.* **8,** 1–8 (2019).

77. Nikolajsen, T., Leosson, K. & Bozhevolnyi, S. I. Surface plasmon polariton based modulators and switches operating at telecom wavelengths. *Appl. Phys. Lett.* **85,** 5833–5835 (2004).

78. Razali, N, Mohamed, R, Ehsan, A. A., Kuang, C. & Shaari, S. Thermo-optic coefficient of different photosensitive acrylate polymers for optical application. *J. Nonlinear Opt. Phys. Mater* **14,** 195–201 (2005).

79. Qiu, F., Ge, C., Gu, X. & Yang, D. Synthesis, Photochromism, and Optical Property of a Polymer Containing a Push-Pull Electronic Structure Chromophore and Chirality Skeleton. *Int. J. Polym. Anal. Ch.* **16,** 36–48 (2011).

80. Gagnon, G., Lahoud, N., Mattiussi, G. A. & Berini, P. Thermally activated variable attenuation of long-range surface plasmon-polariton waves. *J. Light. Technol* **24,** 4391–4402 (2006).

81. Gosciniak, J. *et al.* Thermo-optic control of dielectric-loaded plasmonic waveguide components. *Opt. Express* **18,** 1207–1216 (2010).

82. Gosciniak, J., Markey, L., Dereux, A. & Bozhevolnyi, S. I. Efficient thermo-optically controlled Mach-Zhender interferometers using dielectric-loaded plasmonic waveguides. *Opt. Express* **20,** 16300–16309 (2012).

83. Gosciniak, J. & Bozhevolnyi, S. I. Performance of thermo-optic components based on dielectric-loaded surface plasmon polariton waveguides. *Sci. Rep.* **3,** 1803 (2013).

84. Weeber, J.-C. *et al.* Nanosecond thermo-optical dynamics of polymer loaded plasmonic waveguides. *Opt. Express* **21,** 27291–27305 (2013).

85. Nielsen, M. G., Bernardin, T., Hassan, K., Kriezis, E. E. & Weeber, J.-C. Silicon-loaded surface plasmon polariton waveguides for nanosecond thermo-optical switching. *Opt. Lett.* **39,** 2282–2285 (2014).

86. Fan, H., Charbonneau, R. & Berini, P. Long-range surface plasmon triple-output Mach-Zehnder interferometers. *Opt. Express* **22,** 4006–4020 (2014).

87. Joushaghani, A. *et al.* Sub-volt broadband hybrid plasmonic-vanadium dioxide switches. *Appl. Phys. Lett.* **102,** 061101 (2013).

88. Farmakidis, N. *et al.* Plasmonic nanogap enhanced phase-change devices with dual electrical-optical functionality. *Sci. Adv.* **5,** eaaw2687 (2019).

89. Soref, R. & Bennett, B. Electrooptical effects in silicon. *IEEE J. Quantum Electron.* **23,** 123–129 (1987).

90. Dionne, J. A., Diest, K., Sweatlock, L. A. & Atwater, H. A. PlasMOStor: a metal-oxide- Si field effect plasmonic modulator. *Nano Lett.* **9,** 897–902 (2009).

91. Li, M., Wang, L., Li, X., Xiao, X. & Yu, S. Silicon intensity Mach–Zehnder modulator for single lane 100 Gb/s applications. *Photonics Res.* **6,** 109–116 (2018).

92. Testa, F. & Pavesi, L. *Optical Switching in Next Generation Data Centers* (Springer, 2017).

93. Amin, R. *et al.* Sub-wavelength GHz-fast broadband ITO Mach–Zehnder modulator on silicon photonics. *Optica* **7,** 333–335 (2020).

94. Amin, R. *et al.* A Lateral MOS-Capacitor-Enabled ITO Mach–Zehnder Modulator for Beam Steering. *J. Light. Technol* **38,** 282–290 (2020).

95. Haffner, C. *et al.* All-plasmonic Mach–Zehnder modulator enabling optical high-speed communication at the microscale. *Nat. Photonics* **9,** 525–528 (2015).

96. Haffner, C. *et al.* Low-loss plasmon-assisted electro-optic modulator. *Nature* **556,** 483–486 (2018).

97. Polo, J., Mackay, T. & Lakhtakia, A. *Electromagnetic surface waves: a modern perspective* (Newnes, 2013).

98. Zachariasen, W. Skr. Norske Vid. *Ada., Oslo, Mat. Naturv* **4** (1928).

99. Ballman, A. A. Growth of piezoelectric and ferroelectric materials by the CzochraIski technique. *J. A. Ceram. Soc.* **48,** 112–113 (1965).

100. Czochralski, J. Ein neues verfahren zur messung der kristallisationsgeschwindigkeit der metalle. *Z. Phys. Chem* **92,** 219–221 (1918).

101. Weis, R. & Gaylord, T. Lithium niobate: summary of physical properties and crystal structure. *Appl. Phys. A* **37,** 191–203 (1985).

102. Postnikov, A., Caciuc, V & Borstel, G. Structure optimization and frozen phonons in LiNbO3. *J. Phys. Chem. Solids* **61,** 295–299 (2000).

103. Ching, W., Gu, Z.-Q. & Xu, Y.-N. First-principles calculation of the electronic and optical properties of LiNbO 3. *Phys. Rev. B* **50,** 1992 (1994).

104. Schmidt, W. G. *et al.* LiNbO$_3$ ground- and excited-state properties from first-principles calculations. *Phys. Rev. B* **77,** 035106 (2008).

105. Abel, S. *et al.* Large Pockels effect in micro-and nanostructured barium titanate integrated on silicon. *Nat. Mater.* **18,** 42–47 (2019).

106. Eltes, F. *et al.* Low-loss BaTiO3–Si waveguides for nonlinear integrated photonics. *ACS Photonics* **3,** 1698–1703 (2016).

107. Xiong, C. *et al.* Active silicon integrated nanophotonics: ferroelectric BaTiO$_3$ devices. *Nano Lett.* **14,** 1419–1425 (2014).

108. Abel, S. *et al.* A hybrid barium titanate–silicon photonics platform for ultraefficient electro-optic tuning. *J. Light. Technol* **34,** 1688–1693 (2016).

109. Wang, C. *et al.* Integrated lithium niobate electro-optic modulators operating at CMOS-compatible voltages. *Nature* **562,** 101–104 (2018).

110. Wang, C., Zhang, M., Stern, B., Lipson, M. & Lončar, M. Nanophotonic lithium niobate electro-optic modulators. *Opt. Express* **26,** 1547–1555 (2018).

111. Dicken, M. J. *et al.* Electrooptic modulation in thin film barium titanate plasmonic interferometers. *Nano Lett.* **8,** 4048–4052 (2008).

112. Zgonik, M. *et al.* Dielectric, elastic, piezoelectric, electro-optic, and elasto-optic tensors of BaTiO$_3$ crystals. *Phys. Rev. B* **50,** 5941 (1994).

113. Basu, T, Sen, S, Seal, A & Sen, A. Temperature dependent electrical properties of PZT wafer. *J. Electron. Mater.* **45,** 2252–2257 (2016).

114. Alexander, K. *et al.* Nanophotonic Pockels modulators on a silicon nitride platform. *Nat. Commun.* **9,** 3444 (2018).

115. Kajzar, F. *Organic thin films for waveguiding nonlinear optics* (CRC Press, 1996).

116. Palessonga, D *et al.* Bandwidth improvement of microwave photonic components based on electro-optic polymers loaded with TiO 2 nanoparticles. *Appl. Phys. A* **123,** 542 (2017).

117. Randhawa, S. *et al.* Performance of electro-optical plasmonic ring resonators at telecom wavelengths. *Opt. Express* **20,** 2354–2362 (2012).

118. Zhang, X. *et al.* High performance optical modulator based on electro-optic polymer filled silicon slot photonic crystal waveguide. *J. Light. Technol* **34,** 2941–2951 (2015).

119. Alloatti, L. *et al.* 100 GHz silicon–organic hybrid modulator. *Light Sci. Appl.* **3,** e173–e173 (2014).

120. Ayata, M. *et al.* High-speed plasmonic modulator in a single metal layer. *Science* **358,** 630–632 (2017).

121. Salamin, Y. *et al.* Compact and ultra-efficient broadband plasmonic terahertz field detector. *Nat. Commun.* **10,** 1–8 (2019).

122. Heni, W. *et al.* Plasmonic IQ modulators with attojoule per bit electrical energy consumption. *Nat. Commun.* **10,** 1–8 (2019).

123. Elder, D. L., Benight, S. J., Song, J., Robinson, B. H. & Dalton, L. R. Matrix-assisted poling of monolithic bridge-disubstituted organic NLO chromophores. *Chem. Mater.* **26,** 872–874 (2014).

124. Dalton, L. R., Harper, A. W. & Robinson, B. H. The role of London forces in defining noncentrosymmetric order of high dipole moment–high hyperpolarizability chromophores in electrically poled polymeric thin films. *P. Natl. Acad. Sci. USA* **94,** 4842–4847 (1997).

125. Miller, D. A. Energy consumption in optical modulators for interconnects. *Opt. Express* **20,** A293–A308 (2012).

126. McGuire, A, Scott, M, Thomas, A. & Booth, R. Practical low voltage 2×2 polarisation independent LiNbO$_3$ digital optical switch. *Electron. Lett.* **27,** 1025–1026 (1991).

127. Ramaswamy, R. & Kim, H. A novel, tapered, both in dimension and in index, velocity coupler switch. *IEEE Photon. Technol.* **5,** 557–560 (1993).

128. Hu, H, Ricken, R, Sohler, W & Wehrspohn, R. Lithium niobate ridge waveguides fabricated by wet etching. *IEEE Photon. Technol.* **19,** 417–419 (2007).

129. Noguchi, K. & Miyazawa, H. *LiNbO3 waveguided modulators for 40 Gbit/s and beyond* in *Integrated Photonics Research* (Optical Society of America, 2000), IThH2.

130. Rabiei, P. & Steier, W. H. Lithium niobate ridge waveguides and modulators fabricated using smart guide. *Appl. Phys. Lett.* **86,** 161115 (2005).

131. Guarino, A., Poberaj, G., Rezzonico, D., Degl'Innocenti, R. & Günter, P. Electro–optically tunable microring resonators in lithium niobate. *Nat. Photonics* **1,** 407–410 (2007).

132. García-Granda, M., Hu, H., Rodríguez-García, J & Sohler, W. Design and fabrication of novel ridge guide modulators in lithium niobate. *J. Light. Technol* **27,** 5690–5697 (2009).

133. Chen, L., Xu, Q., Wood, M. G. & Reano, R. M. Hybrid silicon and lithium niobate electro-optical ring modulator. *Optica* **1,** 112–118 (2014).

134. Rao, A. *et al.* High-performance and linear thin-film lithium niobate Mach–Zehnder modulators on silicon up to 50 GHz. *Opt. Lett.* **41,** 5700–5703 (2016).

135. Weigel, P. O. *et al.* Bonded thin film lithium niobate modulator on a silicon photonics platform exceeding 100 GHz 3-dB electrical modulation bandwidth. *Opt. Express* **26,** 23728–23739 (2018).

136. Petraru, A, Schubert, J, Schmid, M & Buchal, C. Ferroelectric BaTiO$_3$ thin-film optical waveguide modulators. *Appl. Phys. Lett.* **81,** 1375–1377 (2002).

137. Girouard, P. *et al.* $\chi^{(2)}$ Modulator With 40-GHz Modulation Utilizing BaTiO$_3$ Photonic Crystal Waveguides. *IEEE J. Quantum Electron.* **53,** 1–10 (2017).